HAL
open science

Characterization of mass variations in Antarctica in response to climatic fluctuations from space-based gravimetry and radar altimetry data

Athul Kaitheri

▶ **To cite this version:**

Athul Kaitheri. Characterization of mass variations in Antarctica in response to climatic fluctuations from space-based gravimetry and radar altimetry data. Earth Sciences. Université Côte d'Azur, 2021. English. NNT : 2021COAZ4100 . tel-03644306

HAL Id: tel-03644306

https://theses.hal.science/tel-03644306v1

Submitted on 19 Apr 2022

HAL is a multi-disciplinary open access archive for the deposit and dissemination of scientific research documents, whether they are published or not. The documents may come from teaching and research institutions in France or abroad, or from public or private research centers.

L'archive ouverte pluridisciplinaire **HAL**, est destinée au dépôt et à la diffusion de documents scientifiques de niveau recherche, publiés ou non, émanant des établissements d'enseignement et de recherche français ou étrangers, des laboratoires publics ou privés.

UNIVERSITÉ CÔTE D'AZUR

ÉCOLE DOCTORALE
SCIENCES FONDAMENTALES ET APPLIQUÉES

THÈSE DE DOCTORAT

Caractérisation des variations de masse en Antarctique en réponse aux fluctuations climatiques à partir des données de gravimétrie spatiale et d'altimétrie radar

Athul KAITHERI

UMR Géoazur

Présentée en vue de l'obtention du grade de docteur en Sciences de la Planète et de l'Univers **d'**Université Côte d'Azur
Dirigée par : Anthony Mémin
Co-dirigée par : Frédérique Rémy
Soutenue le : 2 Décembre 2021

Devant le jury, composé de :
Jean-Paul Boy, Physicien, EOST Strasbourg
Martin Horwath, Professeur, IFPG Dresden
Agnès Fienga, Astronome, OCA Nice
Muriel Llubes, Maitresse de conférences, Université de Toulouse III Paul Sabatier
Guillaume Ramillien, Directeur de Recherche, GET, CNRS, Toulouse

Caractérisation des variations de masse en Antarctique en réponse aux fluctuations climatiques à partir des données de gravimétrie spatiale et d'altimétrie radar

Jury:

Président du jury
Jean-Paul Boy, Physicien, Ecole et Observatoire des Sciences de la Terre, Strasbourg

Rapporteurs
Jean-Paul Boy, Physicien, Ecole et Observatoire des Sciences de la Terre, Strasbourg
Martin Horwath, Professor, Institut fur Planetare Geodäsie, Dresden

Examinateurs
Agnès Fienga, Astronome, Observatoire de la Côte d'Azur, Nice
Muriel Llubes, Maitresse de conférences, Université de Toulouse III Paul Sabatier
Guillaume Ramillien, Directeur de Recherche, Géosciences Environnement Toulouse, CNRS, Toulouse

Characterizing mass changes in Antarctica in response to climate changes from space-based gravimetry and radar altimetry

Résumé

Quantifier le bilan de masse de l'Antarctique et son impact en termes de niveau de la mer, demande une bonne compréhension de la variabilité interannuelle ainsi que de ces causes. Ceci est devenu plus crucial dans le cadre du réchauffement climatique. Très peu d'études ont été faites sur l'influence des anomalies climatiques sur le comportement de l'Antarctique et sur l'évaluation de leurs impacts. Les variations de volume ou de masse de l'Antarctique sont en majorité basées sur l'altimétrie ou la gravimétrie spatiales. Dans cette thèse, nous utilisons les données des missions d'Envisat (2002 to 2010) et de GRACE (2002 to 2016) afin de restituer respectivement les variations de volume et de masse de la calotte. Nous utilisons aussi les données issues du modèle de climat RACMO2.3p2 afin de forcer notre modèle de compaction. Ce modèle nous permet à la fois d'évaluer la transformation de neige en glace et de corriger les variations d'élévation mesurées par altimétrie.

Les variations de hauteur estimées par ces différentes techniques sont en bon accord les unes avec les autres, particulièrement en Antarctique de l'Ouest, sur la Péninsule et le long de la côte de l'Antarctique de l'Est. Les variations interannuelles sont extraites en utilisant un modèle de décomposition modale empirique (emd). Une étude par moindre carré met en évidence un signal de périodicité proche de 4 ans sur les données issues de l'altimétrie, de la gravimétrie et du modèle RACMO. Ceci semble indiquer une influence de phénomène El Niño, lequel influe sur différents paramètres comme le transport de l'humidité, la température de surface de l'océan, les précipitations autour de l'Antarctique en alternant des périodes froides et des périodes chaudes. Mais d'autres oscillations semi-périodiques peuvent aussi avoir un impact sur la variabilité Antarctique. Citons l'Amundsen Sea Low (ASL) ou le Southern Annular mode (SAM).

Une analyse en composante principale combinant nos trois estimations de hauteur met en évidence des structures similaires. Les anomalies de hauteur semblent circuler dans le sens des aiguilles d'une montre de Coasts Land (CL) vers Pine Island (PIG) en passant par Dronning Maud Land (DML) et Wilkes Land (WL) à une période comprise entre 6 et 8 ans. Ceci suggère une anomalie climatique due à l'onde circumpolaire (ACW) qui se propage à travers l'océan austral en 8 à 10 ans. En résumé, la variabilité interannuelle du bilan de masse Antarctique est modulée

par différentes anomalies climatiques.

Mots clés : Calotte polaire de l'Antarctique, GRACE, Envisat, RACMO2.3p2, modèle de compaction, oscillation australe et onde circumpolaire

Abstract

Quantifying the mass balance of the Antarctic Ice Sheet (AIS), and the resulting sea level rise, requires an understanding of inter-annual variability and associated causal mechanisms. This has become more complex and challenging in the backdrop of global climate change. Very few studies have been exploring the influence of climate anomalies on the AIS and only a vague estimate of its impact is available. Usually changes to the ice sheet are quantified using observations from space-borne altimetry and gravimetry missions. In this study, we use data from Envisat (2002 to 2010) and Gravity Recovery and Climate Experiment (GRACE) (2002 to 2016) missions to estimate monthly elevation changes and mass changes, respectively. Similar estimates of the changes are made using weather variables (surface mass balance (SMB) and temperature) from a regional climate model (RACMO2.3p2) as inputs to a firn compaction (FC) model. Using the firn compaction model we were able to model the transformation of snow into glacial ice and hence estimate changes in the elevation of the ice sheet using climate parameters.

Elevation changes estimated from different techniques are in good agreement with each other across the AIS especially in West Antarctica, Antarctic Peninsula, and along the coasts of East Antarctica. Inter-annual height change patterns are then extracted using for the first time an empirical mode decomposition followed by a reconstruction of modes. These signal on applying least square method revealed a sub-4-year periodic signal in the all the three distinct height change patterns. This was indicative of the influence of the El Niño Southern Oscillation (ENSO), a climate anomaly that alters, among other parameters, moisture transport, sea surface temperature, precipitation, in and around the AIS at similar frequency by alternating between warm and cold conditions. But there existed altering periodic behavior among inter annual height change patterns in the Antarctic Pacific (AP) sector which was found possibly by the influence of multiple climate drivers, like the Amundsen Sea Low (ASL) and the Southern Annular Mode (SAM).

A combined analysis of the three distinct estimates using a PCA (principal component analysis) along the coast revealed similar findings. Height change anomaly also appears to traverse eastwards from Coats Land to Pine Island Glacier (PIG) regions passing through Dronning Maud Land (DML) and Wilkes Land (WL) in 6 to 8 years. This is indicative of climate anomaly traversal due to the Antarctic Circumpolar Wave (ACW) which propagates anomalies through the Southern Ocean in 8 to 10 years. Altogether, inter-annual variability in the SMB of the AIS is found

to be modulated by multiple competing climate anomalies.

Keywords: Antarctic Ice Sheet; GRACE; Envisat; RACMO2.3p2; firn compaction model; ENSO; ACW

Acknowledgements

Gurur Brahma Gurur Vishnu
Gurur Devo Maheshwaraha
Guru Saakshaat Para Brahma
Tasmai Sri Gurave Namaha

Guru is the Creator (Brahma), Guru is the Preserver (Vishnu), GuruDeva is the Destroyer (Maheshwara). Guru is the absolute (singular) Lord himself. Salutations to that Sri Guru.

Past few years has been a period of intense learning and personal growth for me. Preparing this thesis has been a new learning experience. I would like to reflect on the people who have supported and helped me so much throughout this period.

My heartfelt gratitude to both of my thesis directors Frédérique Rémy and Anthony Mémin. First of all, I thank them for the opportunity they offered me to pursue research after my Masters. They have guided me through these years as a young researcher and helped me follow my scientific instincts. They listened me through these years and have shown me light whenever I was lost in the dark. They always gave me the right opportunities and stage to showcase my findings and skills. They found time to point out my weak areas and gave the right advice to help me grow as a better researcher.

I thank all the members of the jury for taking their time to review and validate my work. I express my heartfelt gratitude to Jean-Paul Boy for presiding the jury and making a qualitative review of my work despite his busy engagements. I extend similar feelings towards Martin Horwath who also spared time from his busy schedule to review my thesis. I thank them for their kind gesture towards a budding researcher. I thank Agnès Fienga for being a part of the jury and always keeping me as a part of the research team at Geoazur. She found time to ask the questions at various stages of this project and supported me as an active member of the team. I would also like to thank both Muriel Llubes and Guillaume Ramillien for accepting

our invitation to be a part of the jury. Muriel's words gave much needed strength in the final days of the thesis. Guillaume apart from being a part of the jury, has helped through the years by being a member of my thesis committee. He helped me shape this research by asking the right questions and helped me with things that I left unnoticed. I also thank Carole Petit for being a part of my thesis committee and helping me with things similar to Guillaume.

At this moment, I convey my gratitude towards other members of the AstroGéo GPM team, especially Olivier Laurain, Lucie Rolland and Gilles Metris. The team has provided me a primary platform to discuss my findings and research. I whole heartedly thank other research scholars in the team including Arthur Briaud, Christelle Saliby and Florian Zedek. I also appreciate the help offered by Vishnu Viswananth, an earlier research scholar with the team. They have always found time to listen, discuss and help in this pursuit.

I would like to thank Marc Sosson, Director of the lab for providing me and other fellow researchers the perfect infrastructure to conduct our research and being our leading light. I also thank Jeanick Brisswalter, President of the university and Elisabeth Taffin de Givenchy, director of the doctoral school for providing us with directions and leading us from the front. The university and the doctoral school shaped the researcher inside me through various trainings and activities during the period. I also extend my gratitude towards people at the university and welcome center who facilitated my stay in this beautiful Mediterranean coast.

Working in a suitable and comfortable environment is a key element in research. I thank everyone in the different departments at Géoazur. I thank Jenny Trevisan for her immense work on managing the office logistics during the sanitary crisis. I thank Valérie Mercier and Sandrine Bertétic for welcoming me at my arrival to the lab and for all the help during my stay. I thank David Chapeau, Caroline Ramel and Lionel Maurino from the IT department for handling my many recurrent doubts and annoying issues. I would also like to thank Jelena Giannetti for her kindness and invaluable support at the library.

I extend my heartfelt gratitude to my office mate Paul Jarrin who has always been a constant presence alongside me at my work. I wish him the best on from the deepest of my heart. Along with him, I express my love towards other present and past doctoral and post-doctoral researchers in the lab who always considered me as one among them and helped me in my pursuit. I wish them to achieve their goals. I name a few of them: Thea Ragon, Nicolas Wynants-Morel, Zoe Candaux, Laurie

Boschetti, Carlo Mologni, Jean Furstoss, Serge Sambolian, Hector Alemany, Daniel Mata Flores, Emmanuelle Homonnay, Lionel Mattéo, Ophélie Rohmer, Sébastien Bonnieux, Lise Devreux, Pierre Morena, Dorian Joncour, Marion Baques, etc. They provided me company during the toughest of the tough times by planning various group activities, outings, video calls, etc.

I wish to extend my love towards my Indian friends in Sophia Antipolis, Antibes and Nice who never let me miss my home. I remember my friends who live their life in various parts of Europe and other countries who always made my time here comfortable and memorable.

My friends back in India has always been a shoulder to rest my head upon. They had the patience to listen me, engage with me irrespective of my situation. I express my love for them.

My parents have always let me follow my dreams without any doubt over the years. I owe them whatever I have gained as a human being. I thank them for the sacrifices they did to help me grow as a person without any difficulties. I express my love towards my brother who has always been the person with all the solutions to my difficulties. I thank all my relatives and all my teachers for the thoughts and values they have inculcated in me.

I wish to record my gratitude, with at most reverence and faithfulness to the Almighty God, for leading and guiding in my life.

Contents

1 Introduction **21**

1.1 Climate change scenario 21

1.2 Antarctica 23

1.2.1 Geography 24

1.2.2 Climate 26

1.2.3 Antarctic ice sheet 28

1.2.4 Ice sheet processes & mass balance 29

1.2.5 Inter-annual variability 37

1.3 Thesis overview 37

2 Height changes from satellite observations **41**

2.1 Observations 41

2.2 Satellite Gravimetry 42

2.2.1 Principle 42

2.2.2 Gravity data processing 43

2.2.3 Height changes from GRACE observations 47

2.3 Satellite altimetry 51

2.3.1 Principle 51

2.3.2 Altimetry data processing 54

2.3.3 Height changes from Envisat observations 56

3 Height changes from modelling **61**

3.1 Climate Model 61

3.2 Height changes from RACMO2.3p2 outputs 64

3.3 Firn densification model 67

3.3.1 Numerical experiments 72

3.3.2 Height changes from the firn densification model 75

4 Inter-annual variability **81**

4.1 Comparison between height changes 81

4.1.1 Correlation analysis 81

4.1.2 Regression analysis 82
4.2 Extraction of inter annual signals 86
4.3 Characterizing inter-annual signals 88
4.3.1 Least squares method 89
4.3.2 Periodicity 90
4.3.3 Amplitude 92
4.4 Principal component analysis 93

5 Influence of climate anomalies 101
5.1 El Niño Southern Oscillation 101
5.1.1 Southern Oscillation Index 102
5.1.2 Oceanic Niño Index 105
5.2 Southern Annular Mode 107
5.3 Amundsen Sea Low 109
5.4 Antarctic Circumpolar Wave 111

6 General conclusions 115
6.1 Conclusions 115
6.2 Future perspectives 117

List of Figures

1.1 CO_2 concentration reconstructed from ice cores. Thousands of years before today (0 = 1950) in x axis. Credit: NOAA. 22

1.2 Fracture and loss of ice tongue in Thwaites Glacier, West Antarctica. Images taken on (a) December 2, 2001 and (b) December 28, 2019. Credit: NASA's Earth Observatory. 23

1.3 Greenland and Antarctic ice sheets, constituting 99% of the freshwater ice on Earth. Credit: NSIDC 24

1.4 Map of Antarctica [adapted from Lightenberg 2014 thesis]. The color gradient represents the surface elevation of the grounded ice sheet, in meters above sea level (m a.s.l.). Grey regions indicate floating ice shelves and the thin black line shows the grounding line (GL) that marks the boundary between grounded and floating ice. Names indicate major regions of the ice sheet (bold black), oceanic subareas (blue) and other notable features (oblique black), such as Larsen C Ice Shelf (LCIS), Filchner-Ronne Ice Shelf (FRIS), Amery Ice Shelf (AmIS) and Ross Ice Shelf (RIS). The solid red line represents the upper boundary of the region where annual surface melt occurs (greater than 2 mm water equivalent (w.e.) per year melt during 1979–2011 period [Lenaerts et al., 2012]). 25

1.5 Illustration of all relevant climate processes on the AIS. Adpated from Leanaerts et al., [2019]. 27

1.6 Ice sheet mechanisms and and their corresponding time-scale. Adapted from [Remy & Frezzotti, 2006, Remy & Parouty, 2009]. 30

1.7 Cumulative estimates of Antarctic ice sheet mass change. The solid lines representing cumulative ice-sheet mass changes are determined from the integral of monthly measurement class averages for each ice sheet. The estimated 1σ uncertainty of the cumulative change is shaded. The dashed lines represent the results of a previous assessment made by Shepherd et al. [2012]. 36

2.1 The GRACE mission satellites as they orbit Earth. The drawing is not to scale; the trailing spacecraft would actually be about 220 kilometers behind the lead spacecraft [Earth Observatory NASA]. . . 43

2.2 Working principle of GRACE satellites illustrated [Earth Observatory NASA]. 44

2.3 Mean (a) and standard deviation (b) of gravity changes (in μgal) observed using GRACE. Mean varies between -10 μgal (in blue) and 10 μgal (in red). Standard deviation varies between 0 μgal (in yellow) and 15 μgal (in violet). 48

2.4 Time series of gravity changes in μgal for (a) PIG region and (b) DML region observed using GRACE mission during September 2002 to September 2016. Black (CSR), blue (GFZ) and red (JPL) represent different solutions. The abscissa is the time. The ordinate shows the gravity variations (in μgal), which varies in each subplot. 49

2.5 Time series of mean WEH changes in cm for (a) PIG and (b) DML region estimated from GRACE observations. The abscissa is the time. The ordinate shows the variations in WEH (in cm), which varies in each subplot. 50

2.6 Residuals in SEH (in green), IEH (in yellow) and WEH (in red) at (a) PIG and (b) DML. The abscissa is the time. The ordinate shows the variations in WEH (in cm), which varies in each subplot. 50

2.7 Monthly means of residual changes in WEH estimated from the GRACE solutions at (a) PIG and (b) DML. Error bars represent standard deviation (1 σ) from the mean. The abscissa is the time representing month of the year. The ordinate shows the changes in WEH (in cm), which varies in each subplot. 51

2.8 Standard deviation of residual changes in WEH (in cm) estimated from GRACE solutions during (a) Envisat period (2002 – 2010) and GRACE life time (2002 – 2016). Varies between 0 cm (in yellow) and 6 cm (in violet). 52

2.9 Altimetric waveform shape from Remy & Parouty [2009]. Altimetric observations also provide the return waveform which is the histogram of the backscattered energy with respect to time. The signal is the combination of a surface echo (in light grey) and of a volume echo (in dark grey). 53

2.10 Past, operating, approved, and proposed polar topography altimeter missions [Kern et al, 2020]. 54

2.11 The altimetric waveform is represented in blue alongside the retracking fitting function (in yellow). The variables extracted from the altimetric waveform like range, leading edge width and amplitude, and trailing edge slope are shown. Adapted from Legresy et al. [2005]. 55

2.12 Mean (a) and standard deviation (b) of elevation changes (in cm) estimated using Envisat. Mean varies between -20 cm (in red) and 20 cm (in blue). Standard deviation varies between 0 cm (in yellow) and 20 cm (in violet). 57

2.13 Time series of elevation changes in centimeters for (a) PIG and (b) DML estimated from Envisat observations during September 2002 to October 2010 in blue. The best-fitting quadratic trend is shown in black. Residual changes at each region is represented in red. The abscissa is the time. The ordinate shows the elevation changes (in cm), which varies in each subplot. 58

2.14 Monthly means of residual elevation changes estimated from the Envisat observations. Error bars represent standard deviation (1 σ) from the mean. The abscissa is the time representing month of the year. The ordinate shows the elevation changes (in cm), which varies in each subplot. 58

2.15 Standard deviation of residual changes (in cm) estimated using Envisat observations. Varies between 0 cm (in yellow) and 12 cm (in violet). 59

3.1 Modelled surface mass balance trend (1958–2007) in kg m^{-2} from Ettema et al., [2009]. Thin dashed lines represent 250 m elevation contours from Bamber et al., [2001]. 63

3.2 Symbolic representation of height changes of an ice sheet. Green components like accumulation and bed rock upliftment cause positive changes whereas red components (firn compaction, melt and ice motion) cause negative changes. 65

3.3 Time series of elevation changes in cm for (a) PIG and (b) DML estimated using outputs from RACMO2.3p2 during 1992–2016. The abscissa is the time. The ordinate shows the variations in WEH (in cm), which varies in each subplot. 66

3.4 Residual changes in elevation (in red) and SMB (in yellow) at (a) PIG and (b) DML. The abscissa is the time. The ordinate shows the variations in elevation (in cm) and SMB (in kg m^{-2}), which varies in each subplot. 67

3.5 Monthly means of residual changes estimated from RACMO outputs at (a) PIG and (b) DML. Error bars represent standard deviation (1 σ) from the mean. The abscissa is the time representing month of the year. The ordinate shows the changes in elevation (in cm), which varies in each subplot. 67

3.6 Height changes at (a) PIG and (b) DML from Envisat observations (in red), GRACE observations in WEH (in green) and RACMO (in blue). The abscissa is the time. The ordinate shows the variations in elevation (in cm), which varies in each subplot. 68

3.7 Schematic representation of the firn densification model (FDM) by Ligtenberg [2011]. At the surface the mass adding (arrow up) and mass removing (arrow down) SMB components are shown: precipitation (P), surface sublimation (SU_s), drifting snow sublimation (SU_{ds}) and erosion/deposition (ER_{ds}) and surface melt (Me). The four circles schematically illustrate the processes that are calculated within the model firn layer: firn densification and percolation, retention and refreezing of meltwater. 69

3.8 Density-depth profile at (a) Byrd and (b) Vostok regions. The abscissa is the depth from the surface (in m), which varies in each subplot. The ordinate shows density (in kgm^{-3}). 72

3.9 Parameter settings and results for the first experiment at (a) Byrd and (b) Vostok. The abscissa is time from 1985 to 2015. The top panel depicts temperature (in K) kept constant. The middle panel depicts accumulation rate (in m w.e. a^{-1}) which has an impulse of + 0.5 times the mean rate during 1990 to 1995. The bottom panel depicts the changes in elevation: compacted signal (in blue) and not compacted (in red) and influence of compaction (in black dash). . . . 73

3.10 Parameter settings and results for the second experiment at (a) Byrd and (b) Vostok. The abscissa is time from 1985 to 2015. The top panel depicts temperature (in K) kept constant. The middle panel depicts accumulation rate (in m w.e. a^{-1}) which has an impulse of 0.5 times the mean rate in both directions (positive during 1990-1995 and negative during 1995-2000). The bottom panel depicts the changes in elevation: compacted signal (in blue) and not compacted (in red) and influence of compaction (in black dash). 74

3.11 Parameter settings and results for the third experiment at (a) Byrd and (b) Vostok. The abscissa is time from 1985 to 2015. The top panel depicts accumulation rate (in m w.e. a^{-1}) kept constant. The middle panel depicts temperature (in K) which has an impulse of 2° C during 1990-1995. The bottom panel depicts the changes in elevation: compacted signal (in blue) and not compacted (in red) and influence of compaction (in black dash). 75

3.12 Time series of elevation changes in cm at (a) PIG and (b) DML estimated using outputs from RACMO2.3p2 and the firn densification model during 1992–2016. The abscissa is the time. The ordinate shows the variations in elevation (in cm), which varies in each subplot. 76

3.13 Residual changes in elevation both compacted (in blue) and not compacted (in red) and SMB (in yellow) at (a) PIG and (b) DML. The abscissa is the time. The ordinate shows the variations in elevation (in cm) and SMB (in kg m^{-2}), which varies in each subplot. 77

3.14 Monthly means of residual changes estimated from RACMO outputs and the firn densification model at (a) PIG and (b) DML. Error bars represent standard deviation (1 σ) from the mean. The abscissa is the time representing month of the year. The ordinate shows the changes in elevation (in cm), which varies in each subplot. 77

3.15 Height changes at (a) PIG and (b) DML from Envisat observations (in red), GRACE observations in WEH (in green) and RACMO and firn densification model (in blue). The abscissa is the time. The ordinate shows the variations in elevation (in cm), which varies in each subplot. 78

3.16 Standard deviation of temporal changes (in cm) computed from RACMO outputs during (a) 2002–2010 (Envisat period), (b) 2002–2016 (GRACE period) and (c) 1992–2017. Varies between 0 cm (in yellow) to 16 cm (in violet). 79

3.17 Standard deviation of temporal changes (in cm) observed using (a) Envisat, (b) GRACE in SEH and (c) RACMO for the period 2002-2010. Varies between 0 cm (in yellow) to 12 cm (in violet). 79

4.1 Coefficient of correlation between height changes estimated from (a) Envisat and GRACE, (b) Envisat and RACMO and (c) GRACE and RACMO, during the period 2002 - 2010. Positive and negative correlation coefficients are in red and blue respectively. 82

4.2 Coefficient of regression (left) and uncertainty (right) maps between height changes estimated from (a, d) Envisat and GRACE in SEH, (b, e) Envisat and RACMO, and (c, f) GRACE in SEH and RACMO, during the period 2002–2010. In the coefficient of regression maps, color indicates the magnitude, and the dark circle refer to regions where the coefficient is negative. Larger uncertainty values are indicated using dark red. 84
4.3 Height changes are shown for CL (a), DML (b), PIG (c), and WL (d) with that computed from RACMO in red, GRACE solutions in green, separating WEH (solid) from SEH (dash), and Envisat observations in blue. The abscissa is the time. The ordinate shows the amplitude (in cm), which varies in each subplot. 85
4.4 An example of EMD applied to height changes at DML. SEH from GRACE normalized to standard deviation at DML in red and constituent modes in green. The abscissa is the time. The ordinate shows the amplitude of the signal (in left) and the corresponding mode (in right). 87
4.5 Inter-annual height changes after mode reconstruction following the EMD analysis at CL (a), DML (b), PIG (c), WL (d). Height change estimates are from RACMO (red), GRACE in WEH (green), SEH (dashed green) and Envisat (blue). The abscissa is the time. The ordinate shows the amplitude of the signal (in cm), which varies in each subplot. 89
4.6 Energy ratio of the inter-annual signal extracted from (a) Envisat, (b) GRACE and (c) RACMO. Higher values (in dark red) indicate higher energy contention in the inter-annual signal and lower values (in white) indicate negligible less energy retention. 90
4.7 RMS reduction (in %) of the best single period fitting model for height changes estimated from Envisat (a), GRACE (b), and RACMO (c). Value ranges between the least value 0% (yellow) and the highest value 100% (blue). 90
4.8 Maps of the period of the best fitting model for height changes estimated from Envisat (a), GRACE in SEH (b), and RACMO (c) after EMD. Value ranges between the lowest value 2 years (in yellow) and the highest value 8 years (in blue). The period range is broken down into three classes: A, B, and C. 91
4.9 Histogram of period values extracted from inter-annual signals from Envisat (a), GRACE (b) and RACMO (c). The abscissa is the period (years). The ordinate shows the count of each period. 92

4.10 Maps of the amplitude of the best fitting model for height changes estimated from Envisat (a), GRACE in SEH (b), and RACMO (c) after EMD. Value ranges between 0 (in white) and 12 cm (in red). . . 93

4.11 Explained variance map of the PC1 with locations (black circles) of sites selected to perform the PCA. Darker color indicates larger explained variance. 94

4.12 PC1 height changes ordered by longitude. The grey colored region represents ice shelves. Positive and negative anomalies are in red and blue, respectively. The abscissa is the time. The ordinate shows the amplitude of the signal and observations from each region sampled alongside the AIS coast at equal intervals. 97

4.13 PC1 height changes ordered by time. The grey colored region represents ice shelves. Positive and negative anomalies are in red and blue, respectively. The abscissa is the longitude of region sampled alongside the AIS coast at equal intervals. The ordinate shows the amplitude of the signal and observations at each time period. 98

4.14 Time occurrence of anomalies in PC1 that are longitudinally successive around the AIS. Circles and triangles represent positive and negative anomalies, respectively. The abscissa is the longitude of region sampled alongside the AIS coast at equal intervals. The ordinate shows the time of occurrence of peak at each region. The color depicts the absolute amplitude of the anomaly at each location from PC1. Linear trends are estimated considering negative anomalies (blue), positive anomalies between 135° and 360° E (orange), and positive anomalies between 15° and 285° E (green), ignoring locations with variance $< 70\%$. 99

5.1 Thematic maps of anomalies in sea surface temperature in the Pacific Ocean during a strong La Niña event (top, during December 1988) and El Niño event (bottom, during December 1997). Maps by NOAA Climate. 103

5.2 SOI vs time from 1990 to present to indicate El Niño or La Niña periods and their magnitude. Positive SOI values are in blue and negative values are in red. 104

5.3 ONI vs time from 1990 to present to indicate El Niño or La Niña periods and their magnitude. El Niño or La Niña events fall into four categories: weak, moderate, strong and very strong. 106

5.4 Correlation maps between ONI and inter-annual height changes estimated from (a) ENVISAT, (b) GRACE, and (c) RACMO. Positive and negative correlation coefficients are in red and blue, respectively. 107
5.5 Locations of the 12 stations used to calculate the observation-based SAM index. 6 locations are close to 65° S and leftover 6 are close to 40° S. Adapted from Marshall [Marshall & National Center for Atmospheric Research Staff, 2018]. 108
5.6 Seasonal values of the observation-based SAM index since 1990 to present. Positive values in red and negative values in blue. 109
5.7 An instance of seasonal mean sea level pressure differences around Antarctica with the geographical location of the ASL marked with a '+' symbol where up to 10 hPa difference is experienced on an average. Lower mean sea level pressure values are in blue and the higher mean sea level pressure values in red. The black line box represents the region used to derive the ASL indices. Adapted from Hosking [Hosking & National Center for Atmospheric Research Staff, 2020]. 110
5.8 Time series of monthly shifts in ASL's longitudinal location derived from ERA-Interim data (grey line) along with the 11-month smoothed time series (black line). Adapted from Hosking [Hosking & National Center for Atmospheric Research Staff, 2020]. 111
5.9 Simplified schematic summary of inter annual variations in the SO. Sea surface temperature (warm in red and cold in blue), atmospheric sea-level pressure (high, H and low, L), meridional wind stress, and sea ice extent (grey lines), together with the mean course of the Antarctic Circumpolar Current (green). Sea-ice extent is based on the overall 13-year average. Heavy black arrows depict the general eastward motion of anomalies, and other arrows indicate communications between the circumpolar current and the more northerly subtropical gyres. Adapted from White & Peterson [1996]. 112

6.1 Flowchart of the study. Parallelogram represents data used and rectangle represents a process. The arrow points towards direction of data flow. 116

List of Tables

1.1 The trends of mass change over the Antarctic ice sheet (AIS) published in the last two decades [Gao et al., 2019]. 33
1.2 Mass balance estimates of the AIS aggregated from satellite altimetry, gravimetry and the input–output method. The data were averaged over the period 2003–2010 [Shepherd et al., 2018]. The arithmetic mean of each individual result is also shown for the given regions, along with the combined imbalance of the AIS, calculated as the sum of estimates from the constituent regions. 36

4.1 Regression coefficients between height changes computed using our three data sets at four different locations with respective coordinates in square brackets. Values in the bracket denotes uncertainty. 84
4.2 Correlation coefficients between inter-annual height changes derived using EMD analysis. 87
4.3 Percentage of area covered by each class from each data set. 92
4.4 Explained variance in percentage after Principal Component Analysis (PCA) at the 20 regions. 94
4.5 Coefficient of each data set in PC1 at the 20 regions. 95

5.1 Periods since 1950 to present classified into groups of El Niño or La Niña events based on their magnitude into weak, moderate, strong and very strong. 106

Abbrevations

The following abbreviations are used in this manuscript:

ACW	Antarctic Circumpolar Wave
AIS	Antarctic Ice Sheet
ASL	Amundsen Sea Low
CL	Coats Land
CNES	Centre National d'études Spatiales
CSR	Center for Space Research
DML	Dronning Maud Land
EMD	Empirical Mode Decomposition
ENSO	El Niño Southern Oscillation
ERS	European Remote Sensing
ETM	Enhanced Thematic Mapper
FCM	Firn Compaction Model
FDM	Firn Densification Model
GFZ	GeoForschungsZentrum
GIA	Glacial Isostatic Adjustment
GRACE	Gravity Recovery and Climate Experiment
ICESat	Ice, Cloud,and land Elevation Satellite
IEH	Ice Equivalent Height
IGY	International Geophysical Year
IPCC	Intergovernmental Panel on Climate Change
ISRO	Indian Space Research Organization
JPL	Jet Propulsion Laboratory
NASA	National Aeronautics and Space Administration
NOAA	National Oceanic and Atmospheric Administration
OLI	Operational Land Imager
ONI	Oceanic Niño Index
PCA	Principal Component Analysis
PIG	Pine Island Glacier
RMS	Root Mean Square
SAM	Southern Annular Mode

SEH	Snow Equivalent Height
SIE	Sea Ice Extent
SLP	Sea Level Pressure
SOI	Southern Oscillation Index
SST	Sea Surface Temperature
UNFCCC	United Nations Framework Convention on Climate Change
WEH	Water Equivalent Height
WL	Wilkes Land

Chapter 1

Introduction

"Climate change" is the most sought-after global issue at present since the middle of the 20th century. According to the Intergovernmental Panel on Climate Change (IPCC), changes in the climate over long time periods are identified and described using statistical tests like mean and variations in the properties of the climate system. Changes in the composition of atmosphere or lithosphere due to modulations in solar cycle, volcanic eruptions, etc. too can cause climate change. Acoording to the United Nations Framework Convention on Climate Change (UNFCCC), in its Article 1, climate change is a change of climate which is then attributed directly or indirectly to human activity which alters the composition of the global atmosphere alongside the natural climate variability observed over comparable time-periods. Hence, the UNFCCC makes a distinction between climate change attributable to human made activities modifying the atmospheric composition and climate variability attributable to natural causes [Pachauri et al., 2014].

1.1 Climate change scenario

At present all parts of the world experience more frequent occurrences of extreme climatic events. This includes experiencing heat waves, flash floods, storms, cyclones, wildfires, etc. of higher intensity which were less frequent in the past decades [Masson-Delmotte et al., 2021].

Human activities like deforestation and burning fossil fuels releases are major contributors in releasing carbon dioxide (CO_2), a major greenhouse gas alongside natural contributions from volcanic eruptions and respiration. Apart from CO_2, methane (CH_4) from livestock is 28 times more potent in warming the atmosphere and is the primary agricultural source of greenhouse gases worldwide. Human activities have raised atmospheric concentrations of CO_2 by 48% above pre-industrial levels found in 1850. This rise is more than what had happened naturally over a 20,000-year period (from 185 ppm during the Last Glacial Maximum to 280 ppm in 1850).

Atmospheric CO_2 levels measured at Mauna Loa Observatory, Hawaii presently clocks 417 ppm in June 2021. Nineteen of the warmest years have occurred since 2000, except for 1998. The year 2020 tied with 2016 for the warmest year on record since record-keeping began in 1880. Indirect measurements of CO_2 concentration reconstructed from ice cores is given in figure 1.1 [https://climate.nasa.gov/vital-signs/carbon-dioxide/].

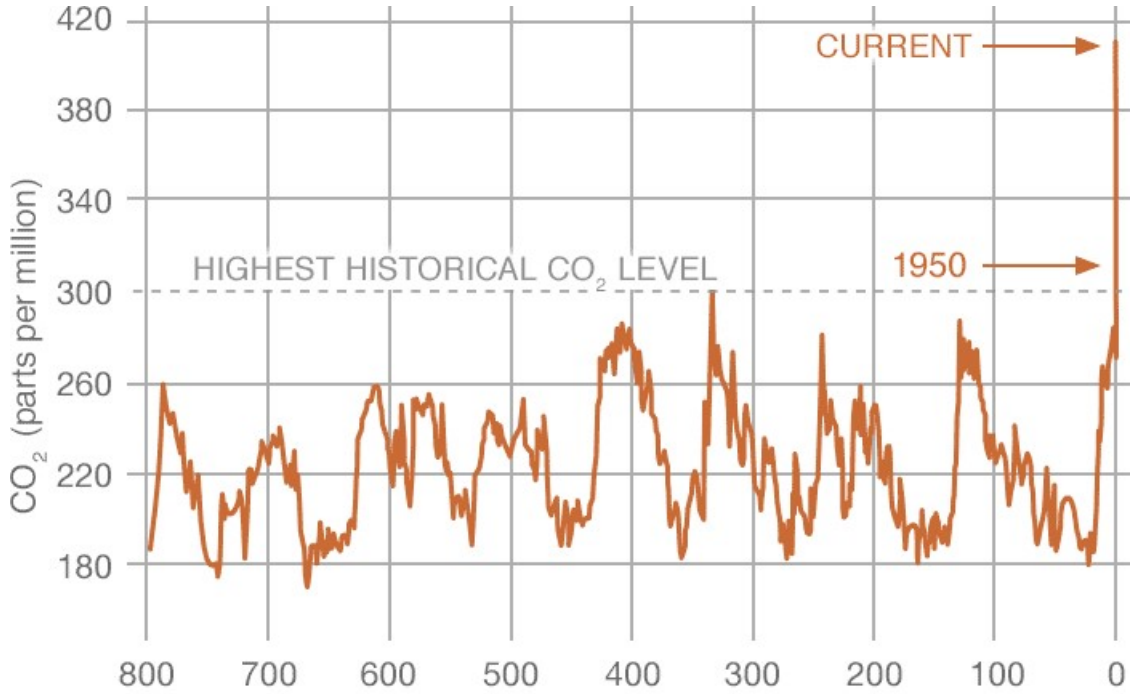

Figure 1.1: CO_2 concentration reconstructed from ice cores. Thousands of years before today (0 = 1950) in x axis. Credit: NOAA.

The biggest impact of these changes will happen to the cold regions of Earth which are often referred to as the Cryosphere. Figure 1.2 gives a glimpse of changes happening at one of the cold regions.

These images depict the cracking and decrease of floating ice between 2001 and 2019. Ice flowing into the sea from Thwaites have increased in the last decades causing sea level rise. The 2001 image was taken with the Enhanced Thematic Mapper (ETM) Plus instrument on Landsat 7. The 2019 image was taken with the Operational Land Imager (OLI) on the Landsat 8 satellite [https://earthobservatory.nasa.gov/images/146247/thwaites-glacier-transformed].

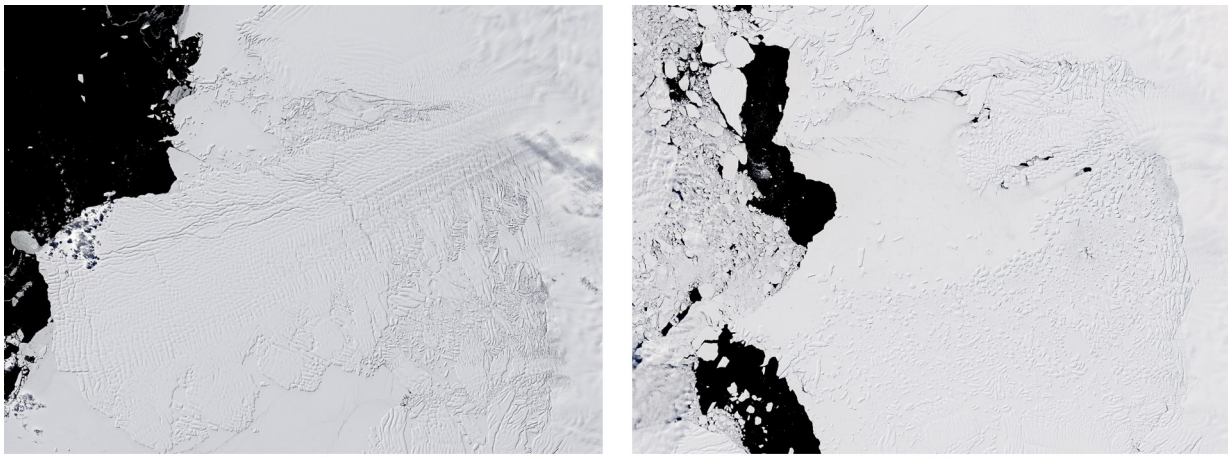

(a) (b)

Figure 1.2: Fracture and loss of ice tongue in Thwaites Glacier, West Antarctica. Images taken on (a) December 2, 2001 and (b) December 28, 2019. Credit: NASA's Earth Observatory.

Role of the cryosphere

The cryosphere refers to the frozen water part of the Earth system. These are places on Earth that are so cold that, water gets frozen into solid state (ice or snow) for at least part of the year and temperature drops below 0° C. The term "cryosphere" has its origin from the Greek word "krios", which means cold.

Continental ice sheets covering Antarctica and Greenland constitute major portion of the cryosphere (figure 1.3). Other forms of cryosphere on land include ice caps, glaciers, and areas with snow and permafrost. Ice flows from continental ice sheets to the sea due to their geometry to form ice shelves. Ocean surrounding Antarctica and the Arctic too freeze to become a part of the cryosphere and is referred as sea ice. Rivers and lakes which freezes during winters also gets included as cryosphere.

These cryosphere components has an important role to play in our planet's climate. Due to their high albedo values, snow and ice reflects radiation from the sun to regulate the temperature. Polar regions, the major constituent of cryosphere being most sensitive to climate shifts, experience changes first hand and serve as an important indicator of these global changes.

1.2 Antarctica

Antarctica apart being the southernmost continent is the driest, windiest, coldest and iciest continent on our planet. Nearly 98% of the total land surface area (14.2 million square km) is covered by ice with varying thickness. The name of the

Figure 1.3: Greenland and Antarctic ice sheets, constituting 99% of the freshwater ice on Earth. Credit: NSIDC

continent literally means "opposite to Arctic" and also geographically lays almost concentrically around the South Pole. Surrounded by the ocean on all sides, the continent and its ice sheet experience a unique climate. Figure 1.4 gives an overview of the continent which holds a lot of superlatives.

1.2.1 Geography

The continent is divided into East Antarctica, West Antarctica and Antarctic Peninsula. East Antarctica is largely composed of a high ice-covered plateau whereas West Antarctica is largely an ice sheet covering an archipelago of mountainous islands. The extended Antarctic Peninsula region along with the Ross Sea and the Weddell Sea stops Antarctica from being circular. The Ross Sea and the Weddell Sea in the south of Pacific and Atlantic oceans respectively, plays a role in dividing the continent into two unequal parts, namely East and West Antarctica. East Antarctica being the bigger among the two. These regions are separated by the Transantarctic Mountains running west of the Ross Ice Shelf, reaching up to the Antarctic Peninsula.

The Antarctic ice sheet contains close to 30 million cubic km of ice, which transform to about 90% and 80% of the world's ice and freshwater respectively. Statistically, the average thickness of ice sheet would be greater than 2000 meters and it goes lower only at regions along the coasts or in ice shelves. Ice thickness reaches upto a maximum of 4000 m in the interiors of the AIS [Fretwell et al., 2013] that

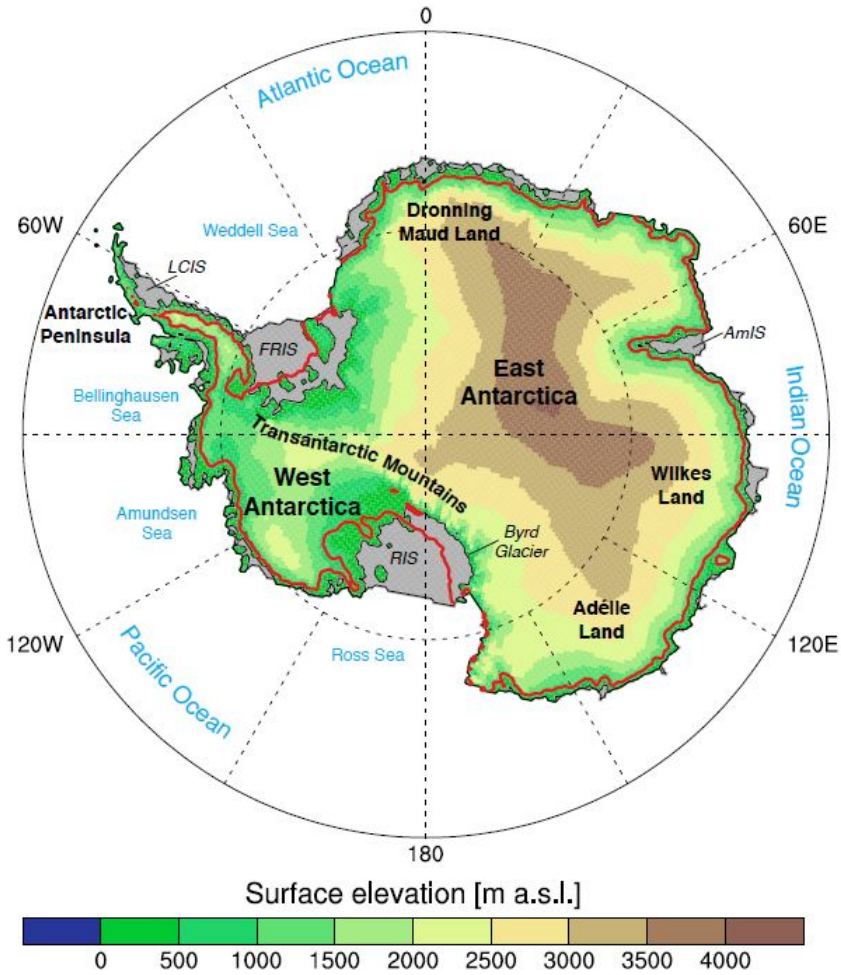

Figure 1.4: Map of Antarctica [adapted from Lightenberg 2014 thesis]. The color gradient represents the surface elevation of the grounded ice sheet, in meters above sea level (m a.s.l.). Grey regions indicate floating ice shelves and the thin black line shows the grounding line (GL) that marks the boundary between grounded and floating ice. Names indicate major regions of the ice sheet (bold black), oceanic subareas (blue) and other notable features (oblique black), such as Larsen C Ice Shelf (LCIS), Filchner-Ronne Ice Shelf (FRIS), Amery Ice Shelf (AmIS) and Ross Ice Shelf (RIS). The solid red line represents the upper boundary of the region where annual surface melt occurs (greater than 2 mm water equivalent (w.e.) per year melt during 1979–2011 period [Lenaerts et al., 2012]).

flows towards the coast, driven by internal deformation and sliding [Bamber et al., 2000]. Along 75% of the coast, the ice flows into the ocean to form large floating ice shelves, that buttress their feeding ice streams [Scambos et al., 2004; Rignot et al., 2004]. These ice shelves cover majority of the Ross and Weddell seas are called the Ross Ice Shelf and the Filchner-Ronne Ice Shelf, respectively. These along with glaciers, ice sheets feed ice into the ocean through discharge or by calving all along the coast.

Marine resources and richness attracted early people to Antarctica until the

middle of 20th century. Later Antarctica emerged as a major destination for science enthusiasts across the seasons since the International Geophysical Year (IGY) in 1957–58. The Antarctic Treaty was signed on December 1, 1959 by the active countries to preserve the continent for non military scientific pursuits. Antarctic Treaty Area sets aside region south of 60° S latitude as Antarctic region. All kind of science including geology, geophysics, glaciology, biology, geochemistry, etc. thrived in the Antarctica. Initial studies used ground based instruments to explore its features whereas satellites and remote sensing techniques emerged as key contributor later.

1.2.2 Climate

Antarctic experience a very unique weather and climate which undergo both spatial and temporal variations. There is automatic weather station (AWS) since the first polar year and in situ measurements along the coasts. But the continent is very large so that these measurements are not enough to represent accuratelty the processes at play. Since the 1970s spaceborne techniques allow a global and synoptic vision of the continent and which later lead to the first models. However, some climate parameters like instantaneous accumulation, wind intensity, snow density, etc cannot be measured from space. The average annual 2-m temperature on Antarctica is $-37°C$ makes it the coldest continent[Lenaerts, 2013] and the majority of the AIS temperatures remain below freezing at any time of the year. Temperatures during winter go down up to $-89.2°C$ in the high inland ice sheet and records up to $-60°C$ near sea level. Temperatures vary spatially as regions closer to the sea experience higher temperatures. Antarctic Peninsula experience higher temperatures comparatively in summer and winter. Average winter temperatures near the coast stay between -20 and $-30°C$ whereas it goes down between -40 and $-70°C$ in the interiors. Similarly in summer, it is $0°C$ near the coast and between -20 and $-35°C$ in the interiors. Surface melt occurs regularly on the bordering ice shelves and in the Antarctic Peninsula, during austral summer (red line in figure 1.4). Global warming has its influence on AIS too as winter temperatures have risen in Antarctic Peninsula and close by regions. It has also driven changes including disintegration of the Larsen Ice Shelf [Lemke et al., 2007]. The steep coastal areas have abundant precipitation and is wetter in comparison, even though it is smaller in area.

Due to its low temperatures, concentration of water vapor in the Antarctic atmosphere is too low and consequentially very little precipitation. Precipitation rate too varies spatially as it varies between few ten millimeters per year in the inlands to few hundred millimeters per year near the coasts. Especially the ice sheet interior is very dry, receiving only ∼10 mm of snow annually [Scambos et al., 2012; Lenaerts

et al., 2012a]. The steep coastal areas, where orographic precipitation is more abundant, are wetter, although these are relatively small in area compared to the ice sheet interior. Low concentration of water vapor in the atmosphere, also helps in losing heat. An illustration of relevant climate processes on the AIS is shown in figure 1.5.

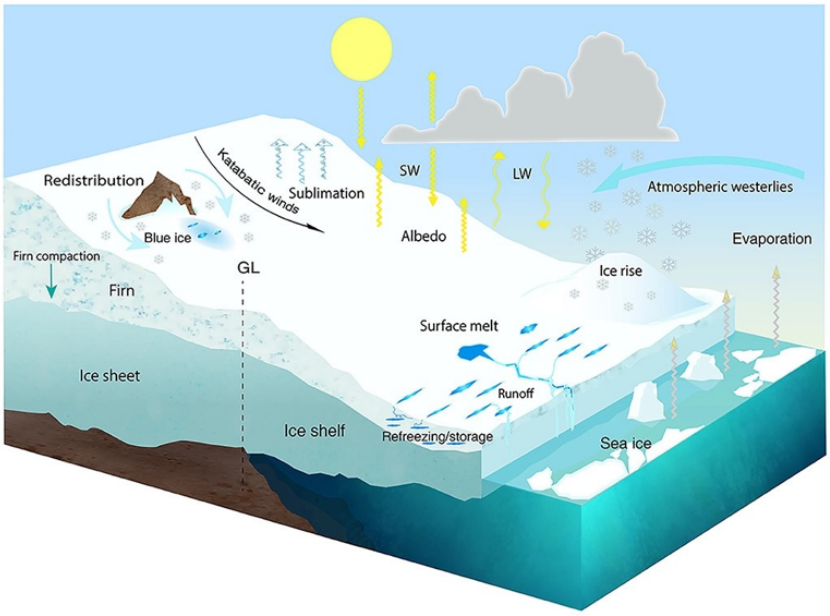

Figure 1.5: Illustration of all relevant climate processes on the AIS. Adpated from Leanaerts et al., [2019].

Antarctica is also subject to fierce winds especially along coastal regions. These winds in East Antarctica flows down the steep slopes from the interior highlands to be called katabatic winds. They even carry loose snow if turbulent and a velocity greater than the critical density. On steeper slopes and in confluence areas, wind speeds are higher, with the highest annual average near-surface wind speeds on Earth (greater than 20 m/s) occurring in the coastal areas of Adélie Land, East Antarctica [Mawson, 1915; Wendler et al., 1997; Lenaerts et al., 2012b]. In other regions, winds are pleasant and mean velocities ranging between 4 meters per second and 8 meters per second during summer and winter, respectively.

Major factor determining Antarctic climate is the 23.5° axial tilt of Earth to its annual plane of orbit around the Sun. This allows polar regions to have long winter nights as well as long summer days as seasons vary. During winter, the ocean surrounding the continent freezes and isolates itself from oceanic heat. Outgoing terrestrial radiation greatly exceeds radiation absorbed allowing strong surface cooling too. There is also exchange of atmospheric heat from the southern Atlantic, Pacific, and Indian oceans to Antarctica aided by winds circumnavigating the continent.

This is also brings precipitation to the continent.

1.2.3 Antarctic ice sheet

An ice sheet is defined as large mass of land ice extending more than 50000 square kilometers. The two major ice sheets on Earth today cover most of Greenland and Antarctica (figure 1.3). During the last glacial maximum (LGM), around 20000 years ago, ice sheets also covered much of North America and Scandinavia. An ice sheet forms through the accumulation of snowfall, when annual snowfall exceeds annual snowmelt. Over a large period of time, multi year snow builds up to form a thick sheet of ice and covering large area. Ice or snow on the top deforms the material in the bottom and forces it to flow.

The shape of the ice sheet is controlled by the equilibrium between snowfall and ice flow [Paterson, 1994]. Every year, few centimeters of fresh snow accumulate in the interior and a few tens of centimeters fall near the coast in the AIS [Vaughn et al., 1999]. This new snow weighs approximately 2200 Gigatons each year and is equivalent to 6 mm of global sea level rise. Small imbalances in this process may therefore contribute to significant changes to global mean sea level. The snow at the surface gets buried by each new snowfall event. The buried snow turns into ice over a long period of time and later flows down very slowly toward the coasts. Ice sheets undergo calving along the coasts. But, some portion of snow melts in between two accumulation periods. This forces the fluffy powder snow to become hard round ice pellets which is later buried when the new snow falls. This continues year after year forcing the material at the bottom to densify due to stress and cold conditions. Over time and depth, it becomes solid ice. Later this ice mass moves influenced by its weight and position.

Ice velocity component is very low in the center of the ice sheets (less than 1 m/yr). This can go up to 100 m/yr near the coastal regions. Therefore, ice sheets tend to be keepers of valuable climate records as it takes several hundreds of thousands years for the snow falling in the center to reach the sea. For instance, the climatic history of 800,000 years was recovered from the EPICA depth ice core at Dome C [Jouzel et al., 2007].

90% of all land ice present on Earth is in the AIS and contains approximately 26.5 million cubic kilometers of ice [Fretwell et al., 2013], which is equivalent to 58.3 m of eustatic sea level rise (SLR). Whereas the remaining 10% of frozen freshwater is found in Greenland (7.4 m of eustatic SLR) [Bamber et al., 2013] and in smaller ice fields and glaciers (0.31–0.53 m of eustatic SLR), such as Alaska, Svalbard, Patagonia, the Himalaya and the Canadian Archipelago [Huss and Farinotti, 2012; Grinsted, 2013; Radi´c et al., 2014; Stocker, 2013].

In Antarctica, the ice shelves that fringe the AIS (grey areas in figure 1.4) are typically a kilometer to a few hundred meters thick [Pritchard et al., 2012], although only almost 10% of their mass is above sea level due to the $\sim 9/10$ relation between the density of glacier ice ($\sim$ 917 kg m^{-3}) and sea water ($\sim$ 1032 kg m^{-3}). Many ice shelves along the Antarctic coast are relatively similar in size ($\sim$ 10000 square kilometers), although two large ice shelves stand out in figure 1.4; the Ross Ice Shelf (RIS) and Filchner-Ronne Ice Shelf (FRIS), each approximately 500000 square kilometers [Rignot et al., 2013]. Along the EAIS coast between 40 – 170 °E, less ice shelves are present.

In order to better understand, model or predict the ice sheet evolution, we need to better understand climatic and dynamic processes which control them.

1.2.4 Ice sheet processes & mass balance

The main mechanisms acting on the geometry of Antarctica and the various associated reaction times is represented in figure 1.6. Ice sheet processes time scales ranges between periods less than 1 year to periods greater than few hundred thousand years. Therefore, variations in the ice sheet volume at present may be due to climate changes at present or during the last 100,000 years. Processes like surface melting, snow precipitation, snow drift, sublimation or melt-refreeze phenomena under ice shelves react almost instantly to climate variation. On the other hand, rivers of ice (ice stream), outfall glaciers or platform dynamics, sea level rise occur a little more slowly, around 10 to 10000 years after the disturbance. Apart from these two types of processes, flow of the ice, the temperature at the base of the cap or the isostasy have very long reaction times, of the order greater than 10000 years.

Of these different types of processes, snow accumulation is the only process which leads to a gain of mass for the ice sheet. Accumulation is the largest component among various processes at the surface. Processes like snow melting, drift, sublimation, ice flow, ice stream, lead to a mass loss for the ice sheet at different time scales. Isostasy which takes few hundred thousand years to reflect refers to the response of the solid Earth to any changes in the ice sheets. It is the term for deformation of the Earth when subjected to forces or to changes in surface loads as our planet is not a rigid body. The nature of this deformation depends largely on the time scale, magnitude, and wavelength of the deforming force or load.

Observations of changes (positive or negative) we make on the ice sheet can be due to any of these processes or a combination of multiple processes. Therefore, a proper understanding of these processes and their properties is important to decode the observations and changes we find on the AIS. Let's see how changes happen to

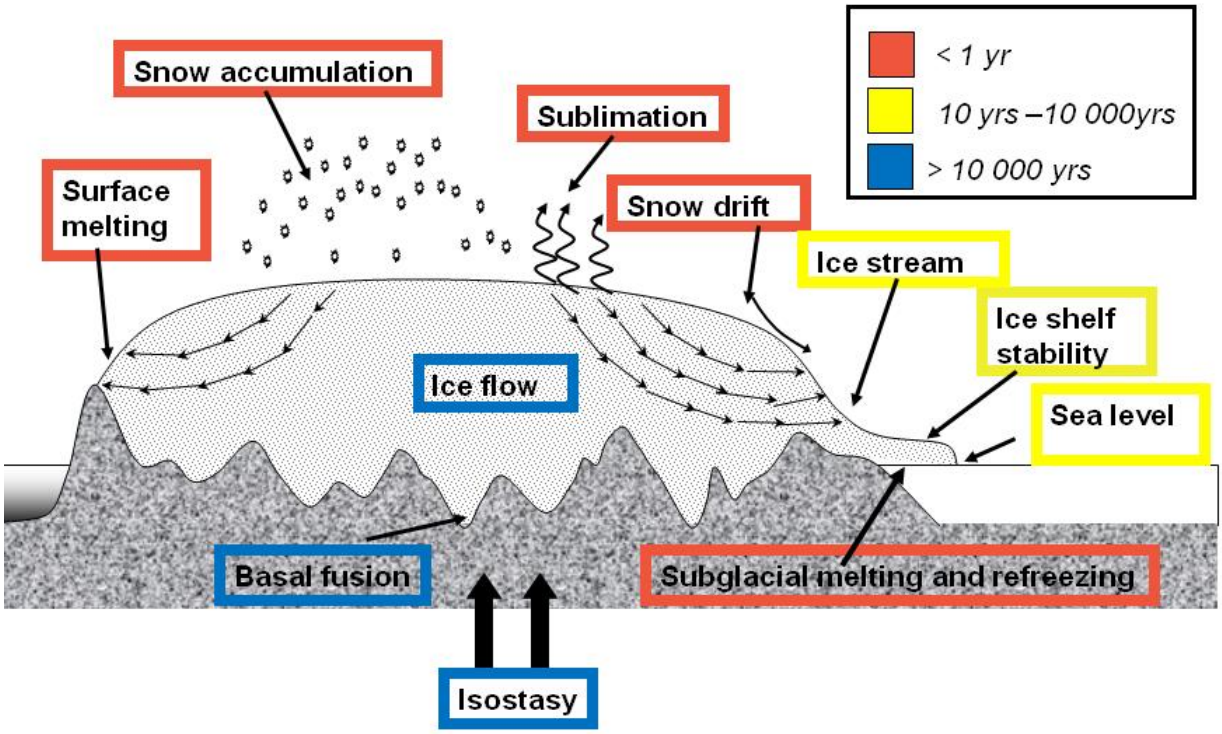

Figure 1.6: Ice sheet mechanisms and and their corresponding time-scale. Adapted from [Remy & Frezzotti, 2006, Remy & Parouty, 2009].

an ice sheet and how it is being quantified and monitored.

Mass balance

A mass balance or material balance, in other words, applies the law of conservation of mass to the analysis of a physical system. It accounts for material or mass entering the system and mass leaving the system. It needs to identify every mass flows happening in the system to have an accurate estimate. Applications of the law of mass conservation varies depending on the nature of the system, but the motto remains to be "matter cannot be created or destroyed".

For an ice sheet, mass balance refers to the net balance between the mass gained and mass lost over a period of time. Mass gain can be due to processes like snow accumulation whereas mass is lost majorly through melting and calving. A positive mass balance indicate the ice sheet is gaining mass as it gained more through accumulation compared to what it lost through calving and melting and vice versa. A negative mass balance directly contributes to a rise in global mean sea level (GMSL). Therefore, it is important, under a warming climate, to have accurate estimates of the mass balance of ice sheets.

In simpler terms, mass balance of an ice sheet (MB) can be expressed as,

$$MB = SMB + ID \tag{1.1}$$

where SMB refers to surface mass balance which is usually positive for the AIS and is reflective of the mass input at the surface whereas ID refers to ice discharge generally a negative value representing mass loss majorly at the edges. This method is often referred as the input-output method (IOM) or the mass budget method [Rignot et al., 2008]. But both surface mass balance and ice discharge in the AIS are large quantities with large uncertainties, which implies that it is difficult to accurately capture the much smaller difference between the two to make a robust estimate of the mass balance. SMB which is the net mass input of an ice sheet can be expressed as,

$$SMB = P – SU_s – SU_{ds} – ER_{ds} – RU \tag{1.2}$$

where P represents precipitation both solid and liquid, SU_s and SU_{ds} are respectively sublimation of surface snow and drifting snow. ER_{ds} is erosion of drifting snow and RU stands for runoff of meltwater [Lenaerts et al., 2012a]. Precipitation is the largest component of the Antarctic SMB and mainly falls as snow on the ice sheet. Sublimation of surface and drifting snow, as well as drifting snow erosion, removes part of the newly accumulated snow. Whereas meltwater happens when snow melts at the surface. But meltwater will percolate into the snow where it refreezes as ice. If enough snow melts, the pore space gets saturated and meltwater can eventually run off into the ocean. In Antarctica, surface runoff is small as almost all meltwater refreezes locally [Ettema et al., 2009; Van Angelen et al., 2013].

Mass output from the AIS is in the form of discharge of solid ice into the ocean. The boundary between grounded and floating ice is called the grounding line and is often used as 'gate' where the discharge of grounded ice is calculated [Rignot et al., 2011a]. When the ice passes the grounding line, it forms floating ice shelves. These ice shelves lose their mass to the ocean by two processes that are more or less equal in magnitude. It may be as iceberg calving at the front of the ice shelf and basal melting at the bottom of the ice shelf that is in contact with the relatively warm ocean water [Depoorter et al., 2013; Rignot et al., 2013].

Until early 1990s, the mass balance of large ice sheets like Greenland and Antarctica was poorly known due to its remoteness and size. It was often quantified as a residual in the budget of oceanic mass and sea level change. But recent developments in remote sensing techniques and regional climate modelling have made resolving of the ice sheet mass balance components possible at a near-annual timescale [Van den Broeke et al., 2011]. Spaceborne geodetic techniques were available since 2000s to measure the changes in mass and volume of ice sheet, such as the dual-satellite

mission named Gravity Recovery and Climate Experiment (GRACE) and satellite altimetry mission including two kinds of sensor, radar and laser. Thus there are three widely used methods are the mass budget method [e.g. Rignot et al., 2008], the volumetric method [e.g. Davis et al.,2005] and the gravimetric method [e.g. Velicogna and Wahr, 2006].

In the mass budget method, both the mass input to and mass output from the ice sheet are calculated separately and the difference gives the mass balance of the ice sheet (Equation 1.1). Evolution of climate models and input derived from various satellite products helped in deriving the mass input. The SMB is taken as the input mass to the ice sheet, which is either estimated from in-situ observations interpolated with a satellite derived background field [Vaughan et al., 1999; Arthern et al., 2006] or simulated with a climate model [Van de Berg et al., 2006; Lenaerts et al., 2012a]. In Antarctica, the SMB is mainly driven by precipitation in the form of snowfall. Other SMB components include rainfall, sublimation, drifting snow erosion and runoff, but are smaller in magnitude to precipitation. Ice discharge is the mass lost and is calculated as the amount of ice that flows over the grounding line, given by the vertically averaged ice velocity multiplied by the ice thickness. Ice velocities are obtained from differencing radar satellite images (SAR Interferometry) [Rignot et al., 2011b], while ice thickness is deduced from either the floatation criterium at the grounding line [Rignot et al., 2011c] or direct observations using ice penetrating radar from airplanes [Li et al., 2013; Rignot et al., 2013].

The volumetric method relies on satellite altimetry (radar and laser) observations to measure surface elevation changes with time [Davis et al., 2005; Wingham et al., 2006; Pritchard et al., 2009]. These changes in surface elevation provide a change in volume, which can be converted into an ice mass change if the density at which the elevation change occurs is known. Surface elevation changes can also be caused by other processes, such as bedrock movement due to changes in ice loading (glacial isostatic adjustment) [Peltier, 2004; Spada et al., 2011; Whitehouse et al., 2012], SMB changes [Horwath et al., 2012], firn densification changes (Helsen et al. [2008] and Ligtenberg 2014). On ice shelves, changes in sea level can cause surface elevation changes [Pritchard et al. [2012]. Therefore, to extract ice sheet mass balance from surface elevation measurements, multiple corrections have to be applied depending on the processes likely to be influencing the measurements.

In the gravimetric method, direct measurements of the mass changes are made by observing the changes in the Earth's gravity field with the GRACE tandem satellites. To extract ice sheet mass balance from GRACE measurements, all other mass changes in the surrounding environment has to be taken into consideration. This include majorly glacial isostatic adjustment (GIA), ocean tides, atmospheric variations, etc. It is important to explicitly distinguish the different processes, as

densities vary largely between bedrock (∼3500 kg m^{-3}), ocean water (∼1032 kg m^{-3}), ice (∼917 kg m^{-3}) and snow (∼350 kg m^{-3}) [Riva et al., 2009]. Even though this method gives most direct measure of the mass changes compared to other two in principle, it has a relatively coarse spatial resolution (∼250 km) of the GRACE satellite and is largely subject to leakage effect.

Each of the three techniques rely on differing satellite observations and differing corrections for surface processes to get the right interpretation from the estimated ice sheet mass changes. Interestingly another approach named joint inversion estimate (JIE) has evolved with aim of reducing the uncertainty of GIA. This method combines multiple geodetic data as we lack climatological and geophysical data to constrain the glacial history and visco-elastic Earth structure. Table 1.1 summarizes trends of mass change over the Antarctic ice sheet (AIS) published in the last two decades [Gao et al., 2019]. This also include reconciled estimates (RE) of ice-sheet mass change computed as the mean of the technique dependent values available at each epoch [Shepherd et al., 2018]. Large differences exist among published estimates within a range of the total mass change from -252 to 112 Gt/yr. But it clearly indicates the reduced disparity in mass change trends while using JIE or RE compared to using a single method.

Table 1.1: The trends of mass change over the Antarctic ice sheet (AIS) published in the last two decades [Gao et al., 2019].

Method	Time period	Trend (Gt/yr)	Reference
IOM	1995-2000	-26 ± 27	Rignot & Thomas [2002]
IOM	1996 2000 2006	-112 ± 91 -138 ± 92 -196 ± 92	Rignot et al. [2008]
IOM	1992-2009	-83 ± 91	Rignot et al. [2011]
IOM	2003-2009	-105 ± 59	Gardner et al. [2013]
IOM	1979-1990 1989-2000 1999-2009 2009-2017	-40 ± 9 -50 ± 14 -166 ± 18 -252 ± 26	Rignot et al. [2019]
Radar	1992–1996	-60 ± 76	Wingham et al. [1998]
Radar	1992–2001	-31 ± 12	Zwally et al. [2005]
Radar	1992–2003	27 ± 29	Wingham et al. [2006]
Radar	1995–2003	25 ± 14	Helsen et al. [2008]
Radar	1992–2001	-31 ± 12	Zwally & Giovinetto [2011]
Radar	2010–2013	-159 ± 48	McMillan et al. [2014]

Radar	2011–2014	-129 ± 83	Helm et al. [2014]
Radar	1992–2001	112 ± 61	Zwally et al. [2015]
Laser	2003–2007	98	Gunter et al. [2009]
Laser	2003–2008	-78 ± 5	Shi et al. [2011]
Laser	2003–2009	-6 ± 10	Gardner et al. [2013]
Laser	2003–2009	-60 ± 44	Helm et al. [2014]
Laser	2003–2009	-126 ± 20	Groh et al. [2014]
Laser	2003–2008	82 ± 25	Zwally et al. [2015]
Laser	2003–2008	-44 ± 21	Li et al. [2016]
Radar & Laser	1992–2017 2010–2017	-85 ± 16 -137 ± 25	Schröder et al. [2019]
GRACE	2002–2005	-139 ± 73	Velicogna and Wahr [2006]
GRACE	2002–2005	-40 ± 36	Ramillien et al. [2006]
GRACE	2002–2006	-150 ± 73	Moore and King [2008]
GRACE	2003–2007	-74	Gunter et al. [2009]
GRACE	2002–2009 2002–2006 2006–2009	-143 ± 73 -104 -246	Velicogna [2009]
GRACE	2002–2009	-190 ± 77	Chen et al. [2009]
GRACE	2002–2008	-109 ± 48	Horwath and Dietrich [2009]
GRACE	2002–2007	-78 ± 37	Yang et al. [2009]
GRACE	2003–2008	-198 ± 22	Cazenave et al. [2009]
GRACE	2002–2008	-91	Zhu et al. [2009]
GRACE	2002–2010	-82 ± 29	Jia et al. [2011]
GRACE	2002–2010	-69 ± 18	King et al. [2012]
GRACE	2003–2010	-165 ± 72	Jacob et al. [2012]
GRACE	2002–2010	-80	Luo et al. [2012]
GRACE	2006–2011	-211 ± 75	Tang et al. [2012]
GRACE	2003–2011	-83 ± 36	Barletta et al. [2013]
GRACE	2003–2012	-57 ± 34	Ivins et al. [2013]
GRACE	2003–2010	-81 ± 26	Luthcke et al. [2013]
GRACE	2003–2012 2003–2012	-83 ± 49 -147 ± 80	Velicogna and Wahr [2013]
GRACE	2004–2012	-196 ± 21	Ju et al. [2013]
GRACE	2003–2012	-107 ± 30	Groh et al. [2014]
GRACE	2003–2012	-58 ± 16	Williams et al. [2014]
GRACE	2003–2013	-171 ± 22	

	2003–2010	-156 ± 24	Schrama et al. [2014]
GRACE	2003–2014	-92 ± 10	Harig and Simons [2015]
GRACE	2003–2013 0	-81 ± 27	Gao et al. [2015]
GRACE	2003–2012	-107 ± 34	Mu et al. [2017]
JIE	2002–2008	-87 ± 43	Wu et al. [2010]
JIE	2002–2013	-114 ± 23	Sasgen et al. [2013]
JIE	2003–2010	-47 ± 35	Mémin et al. [2014]
JIE	2003–2009	-100 ± 44	Gunter et al. [2014]
JIE	2003–2009	-67 ± 55	Gao et al. [2016]
JIE	2003–2013	-84 ± 22	Martín-Español et al. [2016]
JIE	2002–2015	-95 ± 50	Forsberg et al. [2017]
JIE	1993–2000 2000–2005 2005–2013	-156 ± 22 -20 ± 41 -103 ± 20	Talpe et al. [2017]
JIE	2003–2009	-46 ± 43	Zhang et al. [2017]
JIE	2003–2016	-141 ± 27	Sasgen et al. [2017]
RE	1992–2011 1992–2000 1993–2003 2000–2011 2005–2010	-71 ± 53 -48 ± 65 -71 ± 61 -87 ± 43 -81 ± 37	Shepherd et al. [2012]
RE	1992–1997 1997–2002 2007–2012 2012–2017 1992–2011 1992–2017	-49 ± 67 -38 ± 64 -160 ± 50 -219 ± 43 -76 ± 59 -109 ± 56	Shepherd et al. [2018]

Other than RE estimates of ice sheet mass changes for the whole AIS, Shepherd et al. [2018] also discussed differences in ice sheet mass change trends in different regions of the AIS. Figure 1.7 gives a glimpse of ice mass change trends for the West Antarctica, the East Antarctica, the Antarctic Peninsula and the whole AIS. Clearly West Antarctica is driving the overall decrease of mass in Antarctica with a rate accelerating since 2005.

Table 1.2 summarizes the table 1.1 and figure 1.7. It gives a clear picture on ice mass change trends and associated uncertainty in the estimate for each region and for each method employed.

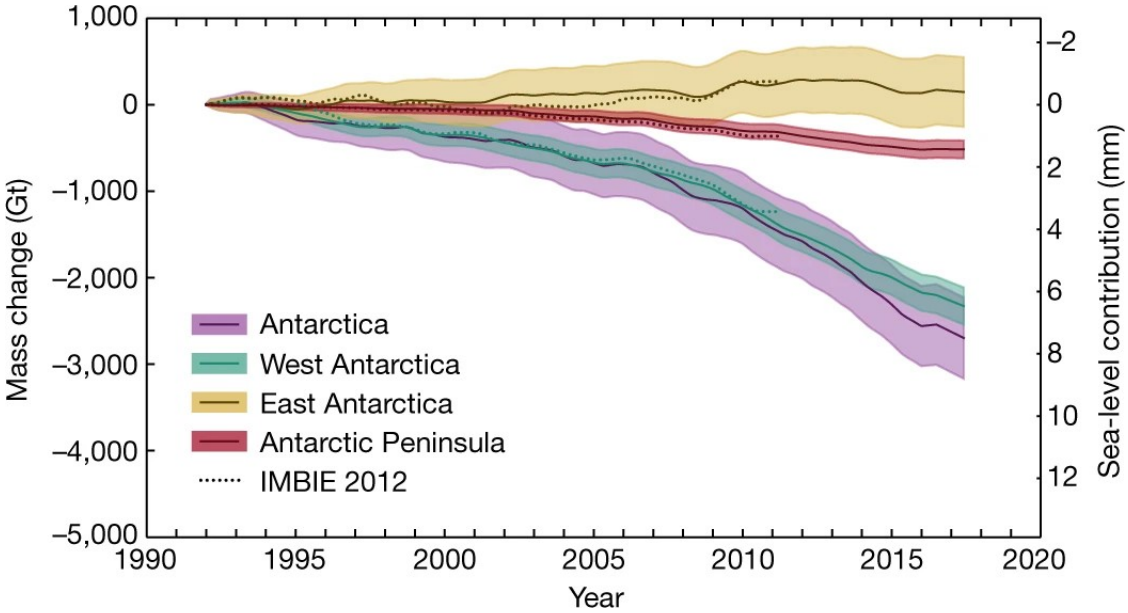

Figure 1.7: Cumulative estimates of Antarctic ice sheet mass change. The solid lines representing cumulative ice-sheet mass changes are determined from the integral of monthly measurement class averages for each ice sheet. The estimated 1σ uncertainty of the cumulative change is shaded. The dashed lines represent the results of a previous assessment made by Shepherd et al. [2012].

Table 1.2: Mass balance estimates of the AIS aggregated from satellite altimetry, gravimetry and the input–output method. The data were averaged over the period 2003–2010 [Shepherd et al., 2018]. The arithmetic mean of each individual result is also shown for the given regions, along with the combined imbalance of the AIS, calculated as the sum of estimates from the constituent regions.

Region	Altimetry mass balance (Gt/yr)	Gravimetry mass balance (Gt/yr)	Mass budget mass balance (Gt/yr)	Average mass balance (Gt/yr)
EAIS	37 ± 18	47 ± 18	-35 ± 65	15 ± 41
WAIS	-70 ± 8	-101 ± 9	-115 ± 43	-93 ± 26
APIS	-10 ± 9	-23 ± 5	-51 ± 24	-27 ± 15
AIS	-43 ± 21	-76 ± 20	-201 ± 82	-105 ± 51

Even when the techniques vary largely, the results reveal significant mass losses in ice sheets, caused by the acceleration of marine-terminating glaciers in coastal West Antarctica. East Antarctica is also seen to have a slight positive mass balance and to gain mass. But the mass balance for the whole AIS is expected to be close to -105 ± 51 Gt/yr. for the period 1992–2017.

1.2.5 Inter-annual variability

Long term mass change trends differ by huge masses between time scales even though the methodology adopted remains almost the same. This can be due to improvements in estimating mass changes from various observations, better corrections for surface processes, and occurrence of inter-annual climate processes. The influence of the first two reasons can be appreciated and quantified in the process whereas the influence of inter-annual climate process remains largely unanswered.

It is important to have the updated knowledge on the inter-annual variability due to various reasons. This include better quantification of signal-to-noise ratio (SNR) in climate trends, identifying opportunities for seasonal predictions and to assess the capacity of climate models to respond to global climate variability [Marion Donat-Magnin et al., 2020]. Periods coinciding with particularly strong climatic event could trigger irreversible grounding line retreat or increased precipitation modifying the long-term trend of changes. Inter-annual variability does not show uniform behavior across the ice sheet as multiple and varying inter-annual climate processes compete locally. Various studies talk about the influence of climate processes and presence of climate process signature in the ice sheet mass balance at multiple scales [Boening et al., 2012, Sasgen et al., 2010, Memin et al., 2015, Bodart & Bingham, 2019]. Inter-annual variability studies may also be useful to identify and quantify the processes that play a role in mass balance. These processes are subject to decadal changes and needs to have updated information to better understand mass balance changes. But very few studies have explored it based on mass balance estimates from a climate model to establish a possible climate origin.

1.3 Thesis overview

Aim

This thesis aims to identify, describe and quantify inter-annual changes in the Antarctic ice sheets (AIS). I use altimetry and gravimetry observations from multiple spaceborne missions and data from climate models. Having multiple observations of the same physical system will help us better understand various ice sheet processes and quantify its influence on the ice sheet and its mass balance estimates. After obtaining robust estimates of changes from each of the techniques, we aim to quantify the influence of inter-annual climate processes in the mass balance of the AIS which supposedly is significant and may masks other underlying trends.

Research questions

This thesis aims to answer the following research questions:

1. Do observations from multiple geodetic observations make similar estimate of the changes happening in the ice sheet?

2. Can SMB estimates from the climate model be used to make robust estimates of changes of AIS in coherence with other geodetic observations?

3. What are the key takeaways after characterizing seasonal and inter-annual signals obtained from varying techniques?

Outline of the thesis

A brief outline of this thesis is as follows:

Chapter 2 titled "Height changes from satellite observations" lists and discusses various satellite datasets available and used in the study for monitoring the Antarctic ice sheet (AIS). Currently available processing strategies is elaborated and various applications of each dataset is explored. We intend to list error and uncertainties associated with each dataset when applied for studies.

Chapter 3 (Height changes from modelling) discusses the methodology adopted to estimate changes in the AIS using the datasets from climate models. There is a detailed explanation on implementing a firn densification model to estimate height changes with appropriate experiments. A quantitative comparison between the change estimates from multiple techniques is discussed here with key findings in the process.

Chapter 4 talks about inter-annual variability. It has discussion on multiple height change estimates we have and tries to quantify their association. This chapter details methods adopted to extract inter-annual signals and ways to derive its properties. There is discussion on ways to combine inter-annual signals from multiple techniques to derive larger findings.

Chapter 5 titled "Influence of climate anomalies" lists and discusses various global and local climate anomalies. The influence of these climate anomalies on the changes in the AIS is explored using various climate indices and comparing it with the inter-annual mass or height change trends.

Chapter 6 concludes the thesis by discussing major findings from the previous chapters and with a perspective for the future.

Chapter 2

Height changes from satellite observations

To understand the evolution of every physical system it is necessary to have data associated with that particular system or adjacent systems which depend on it or drive it. Data may be procured directly in situ or collected from remote observations. Observations made over time should be processed using appropriate strategies and algorithms to derive meaningful insights and conclusions. Over the years processing of data has improved to obtain more accurate and near–real time estimates of changes.

2.1 Observations

Large size, remoteness and extreme climate conditions are few reasons why there was too little observations available for the Antarctic ice sheets (AIS) and these could not render any major characteristics. Scientific stations are mostly concentrated near the coasts, and only a few traverses during the austral summer expeditions provide sparse data from and about the interiors. In this context, remote sensing was found to be a solution to make observations spatially and temporally. Remote sensing has emerged and evolved as a new observer of the cryosphere particularly the AIS since the latter half of the twentieth century. Remote sensing missions primarily focused on studying the atmosphere and the oceans since the middle of 1970s [Cavalieri & Parkinson, 2008]. Within a couple of decades several sensors started giving a precise measurements of albedo, temperature, wind, surface velocity for ice sheets [Bindschalder, 1998, Masson & Lubin, 2006].

The surface topography has emerged as one of the key parameters that came into prominence later on [Kerr, 1999]. Surface topography data can be used to constrain ice flow models, to test or initialize them along with information on bed topography.

Similarly, various physical processes on the ice sheet often leave specific signature on the ice surface. Surface topography is used in mass balance studies as it monitors the surface elevation changes to give volume variations. Radar altimetry missions existed since the early 1990s monitoring the changes in elevation of the ice sheet. It has larger periods of monitoring in comparison with other altimetry techniques (LASER) and is strong enough to provide subsurface information as microwave has the ability to penetrate the snowpack and give key insights on the weather and other climatic parameters [Remy et al., 2001].

As altimetry is an indirect measure of mass changes of an ice sheet and thus global mean sea level (GMSL) changes, a necessity to directly measure mass changes existed. Distinguishing losses and gains of ice (known density) from those of firn (poorly known density) with altimetry measurements is often difficult. Spaceborne gravimetry, a novel and entirely different approach to quantify mass changes by measuring time - varying gravity field by satellite can overcome these limitations [Pritchard et al., 2010].

2.2 Satellite Gravimetry

2.2.1 Principle

The GRACE mission was launched in March 2002 aiming to estimate changes in Earth's geopotential which is effectively due to processes involving solid Earth, surface and atmospheric mass transport [Rummel, 1980; Kahn et al., 1982; Gaposchkin, 2000; Rowlands et al., 2002]. The precise inter-satellite range and range rate measurements between the two co-orbiting satellites at ∼500 km altitude and ∼220 km apart along-track using a K-Band microwave ranging system enables this [Tapley et al., 2004a, Tapley et al., 2004b, Pritchard et al., 2010]. These satellites orbit Earth from pole to pole about 15 times in a day. Figure 2.1 is a schematic representation of the GRACE satellites.

The leading satellite accelerates and the inter-satellite range increases as it flies over bodies with large mass on the Earth like the Himalayas or the AIS due to the gravitational pull it experiences (figure 2.2). Within a short time period, the trailing satellite experiences the pull at the same rate. These differences in the range between the leading and trailing satellites are later used to derive maps of Earth's geopotential time to time.

Monthly estimates of Earth's global gravity field is provided by GRACE at resolutions of a few hundred kilometers and higher. Over time, these estimates serve

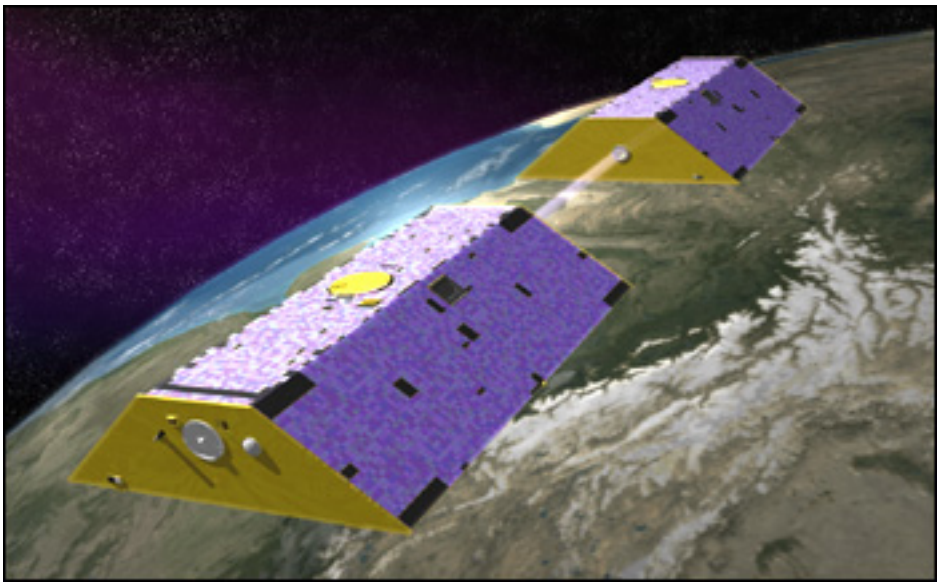

Figure 2.1: The GRACE mission satellites as they orbit Earth. The drawing is not to scale; the trailing spacecraft would actually be about 220 kilometers behind the lead spacecraft [Earth Observatory NASA].

as source for variations in Earth's gravity and hence mass distribution. Due to the unavailability of vertical resolution, it cannot isolate source of variations if it happens to be from solid Earth or atmosphere or Earth surface. Specific methodologies should be adopted by the user to identify the source and isolate the signals [Velicogna & Wahr, 2006].

The GRACE Follow-On (GRACE-FO) mission has an improved instrumentation and is operational since June 2018 with the aim of extending the 15 year monitoring done by the GRACE mission [Landerer et al., 2020]. The GRACE-FO gravity and mass change fields since June 2018 continue the GRACE record at an equivalent precision and spatio-temporal sampling with satellite–to-satellite laser ranging interferometry.

GRACE and GRACE-FO mission, since 2002 has made understanding responses to the changes in the global climate system possible by monitoring of the terrestrial water cycle, mass balance of ice sheets and glaciers, changes in sea level and ocean bottom pressure variations. These missions started as a geodetic experiment and evolved as a source for reliable mass transport products to assess and predict climate trends. This leaves us with a multi-decadal record of mass variability in the Earth [Tapley et al., 2019].

2.2.2 Gravity data processing

The official GRACE Science Data System continuously released monthly GRACE solution for three different processing centers: GeoforschungsZentrum Potsdam (GFZ),

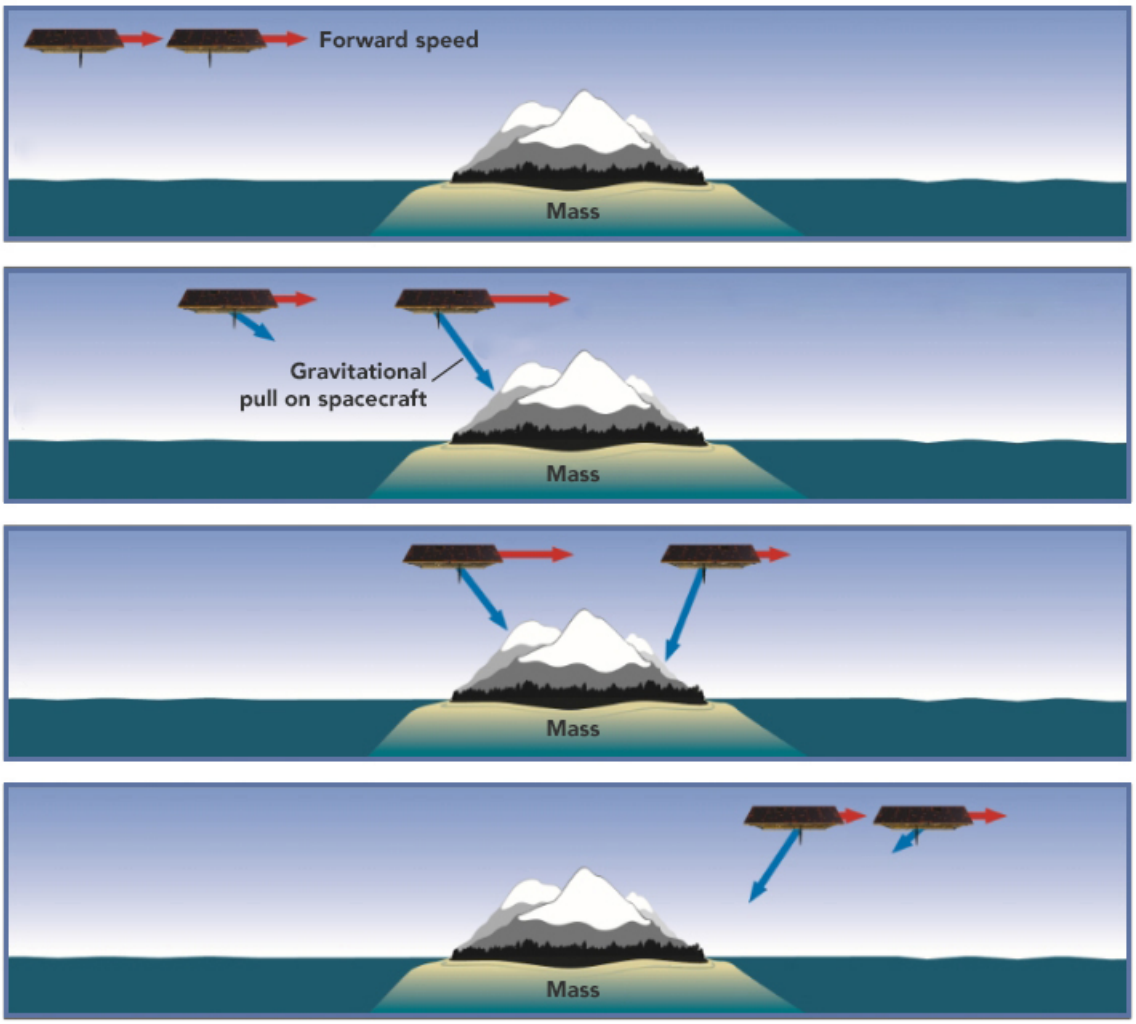

Figure 2.2: Working principle of GRACE satellites illustrated [Earth Observatory NASA].

Center for Space Research at University of Texas, Austin (CSR), and Jet Propulsion Laboratory (JPL). These solutions while the various gravity fields are similar, differences in processing strategies with different background models and tuning parameters result in solutions with regionally specific variations and error patterns [Sakumura et al., 2014]. The spherical harmonic approach (SSH) remained the standard approach during the first decade of GRACE observations.

Mass Concentration blocks (mascons) are another form of gravity field basis function. The "mascon" make the implementing of geophysical constraints much easier and is a much more rigorous approach comparing with the standard spherical harmonic approach of empirical post-processing filtering [Watkins et al., 2015]. The mascon basis functions with help of a priori information derived from near-global geophysical models prevent striping in the solutions. Apart from this, mass flux solutions from mascon suffer less from leakage errors compared to harmonic solutions and gain accurate estimates of mass with less dependence on scale factors. It

also gives greater resolution for smaller spatial regions, particularly when studying secular signals.

In order to process both Envisat and RACMO data sets homogeneously, we use GRACE solutions in the form of spherical harmonics [Memin et al., 2014]. This ensures inter-operability between the multiple distinct data sets. We use Stokes coefficients up to the harmonic degree 50, limiting the spatial resolution to about 400 km. This also limits contamination by noise, including meridional stripes.

Errors

Ice sheet mass balance from GRACE observations are subject to errors related to the limitations of these observations and the magnitude varies region to region. They are broadly errors due to lack of vertical resolution, coarse horizontal resolution, limited temporal resolution and measurement errors [Velicogna & Wahr, 2013].

Gravity changes observed can be due to changes at the surface or in underlying solid earth or in the overlying atmosphere. The exact vertical location of the changes is not exactly known from GRACE observations as the observed changes can be due to either from the three sources or combination of changes at multiple sources. Therefore, to quantify mass changes to an ice sheet, it is necessary to remove both the GIA signal and the signal associated with changes in the atmospheric mass distribution. GIA refers to the Earth's ongoing viscoelastic response to ice mass variability that occurred over the past tens of thousands of years. GIA signal forms a major part of the GRACE signal in Antarctica and is significant whereas it is less important in Greenland [Velicogna & Wahr, 2006a; Velicogna & Wahr, 2006b]. The GIA signal appears as a linear trend in mass M(t) of the ice sheet at time t, i.e., the mass change rate, dM(t)/dt is a constant, and has no impact on the mass acceleration. It is usually removed using a model based on ice history and the Earth's viscosity profile which has its own uncertainties associated with it.

GRACE processing centers such as CSR, GFZ or JPL use the atmospheric fields from the European Centre for Medium Range Weather Forecasts (ECMWF) to remove signal associated with Earth's atmosphere from the level one data as these signals are capable of tampering real estimates of mass changes. Errors in these corrections by the centers are negligibly smaller than the corrections to have influence mass balance estimates of an ice sheet [Velicogna & Wahr, 2013].

Due to the high altitude (∼450 km) at which GRACE satellites orbit, they are often insensitive to short scale terms in the gravity field. These short scale terms also decay with altitude more faster then large scale terms which causes it be source of larger errors. They are significantly down weighted in every processing scheme and omitted entirely at scales below a chosen cutoff which makes the GRACE solutions

band limited. Reduction of these terms happen while generating Stokes coefficients by truncating the solutions to a finite set of low-degree harmonics and while transforming it to mass estimates. The maximum degree (l_{max}) of the solution indicates the smallest spatial scale (r_{min}) that could be resolved. A rule–of-thumb is that $r_{min} \sim 20000/l_{max}$ km which implies for l_{max}=60, r_{min} ~330 km. This truncation not only removes small-scale features but also reduces the overall amplitude of the recovered signal and introduces ringing into the solution [Press et al., 1992]. In the absence of an appropriate processing strategy, it will degrade estimates of mass variability [Velicogna & Wahr, 2013].

Mass signals from outside an ice sheet contaminate the mass loss estimates due to the truncation and the post processing used to reduce short scale noise. Leakage can be probably due to changes in the storage of liquid water and snow on land outside the ice sheet, or ocean mass variability, or ice loss from nearby ice caps. These problems are complicated since GRACE does not provide spherical harmonic coefficients at degree=1. Monthly values of the degree 1 terms can be indirectly computed from the GRACE data, combined with GIA and ocean model output [Swenson et al., 2008]. When those terms are added back to the monthly sets of Stokes coefficients, the sensitivity kernel becomes more focused, and the leakage decreases. The impact on ice sheet estimates is significant, particularly for Antarctica because of its size and its position relative to the polar axis [Velicogna & Wahr, 2013].

Changes in water and snow on land outside the ice sheet can be estimated using monthly global water storage fields from a hydrology model like Noah version of the Global Land Data Assimilation System (GLDAS/Noah) [Rodell et al., 2004]. This is minimal because neither ice sheet is close to land that has appreciable water storage variability and the errors in these corrections would be even smaller. Contributions due to changes in the general circulation of the ocean are reduced by the processing centers prior to computing gravity field solutions, by using output from an ocean general circulation model (OGCM). Changes in water mass due to the exchange of water between the ocean and land can be added separately by computing the total water mass lost or gained every month and adding that amount of water to the ocean and computing the Stokes coefficients caused by that addition. An iterative procedure is used for ice sheets where initially estimates are made without the contribution of water mass and is recalculated after including this contribution and corresponding ocean corrections [Velicogna & Wahr, 2013].

GRACE ice sheet mass balance estimates are also subject to ice loss from nearby glaciers and icecaps too. This becomes difficult to resolve as glaciers in both Antarctica and Greenland are very close to the ice sheets. One can only consider them to be part of the ice sheet since there are not much particular data available for them [Velicogna & Wahr, 2013].

GRACE solutions are available at monthly intervals even when they are not true monthly averages. Chances of intrusion of sub monthly gravity fluctuations exist. To fix this, processing centers use model outputs to remove short period signals from the atmosphere, non-tidal ocean circulation, and Earth and ocean tides before solving them for gravity [Velicogna & Wahr, 2013].

2.2.3 Height changes from GRACE observations

GRACE observations available since 2002 are measurements of changes in the gravity potential of Earth. The release 6 (RL06) of the standard GRACE solutions was obtained from the University of Texas Center for Space Research (CSR, `http://www2.csr.utexas.edu/grace/` accessed on 30 January 2019), the Jet Propulsion Laboratory (JPL, `http://podaac.jpl.nasa.gov/grace` accessed on 30 January 2019), and the GeoForschungsZentrum (GFZ) Potsdam (`http://isdc.gfz-potsdam.de/grace` accessed on 30 January 2019). The solutions provide Stokes coefficients, i.e., fully normalized spherical harmonic coefficients of the gravity potential, on a 30-day sampling. Estimates of monthly variations in gravity potential were made with respect to that on March 2004 to ensure temporal consistency with the Envisat observations.

Mean and standard deviation of the measurement of changes in gravity from the solution provided by CSR Texas observed by GRACE mission during 2002 – 2016 for the AIS is shown in figure 2.3.

From figure 2.3, the changes are found non uniform across the AIS. Large variations in the gravity measurements are found mostly along the coast and the magnitude varies regionally. The mean of the gravity change observations is either largely positive or slightly negative across the ice sheet apart from coastal regions in West Antarctica between 90° W and 130° W where it is largely negative. The standard deviation of the observations too is high indicating large scale variability in this region. Regions in the interiors of East Antarctica has a negative mean and low standard deviation. Two regions are chosen due to: large variability and a negative mean (76° S 100° W namely Pine Island Glacier (PIG) region) and low variability and a positive mean (70° S 30° E namely Dronning Maud Land (DML) region) for further analysis. Time series of changes in gravity measurements at these two regions is given in figure 2.4.

Observations from these regions has differing trends as gravity potential seems to reduce at PIG region whereas it seems to increase in DML. It reduces around 50 μgal at PIG in 14 years whereas it increases by around 15 μgal at DML in the same

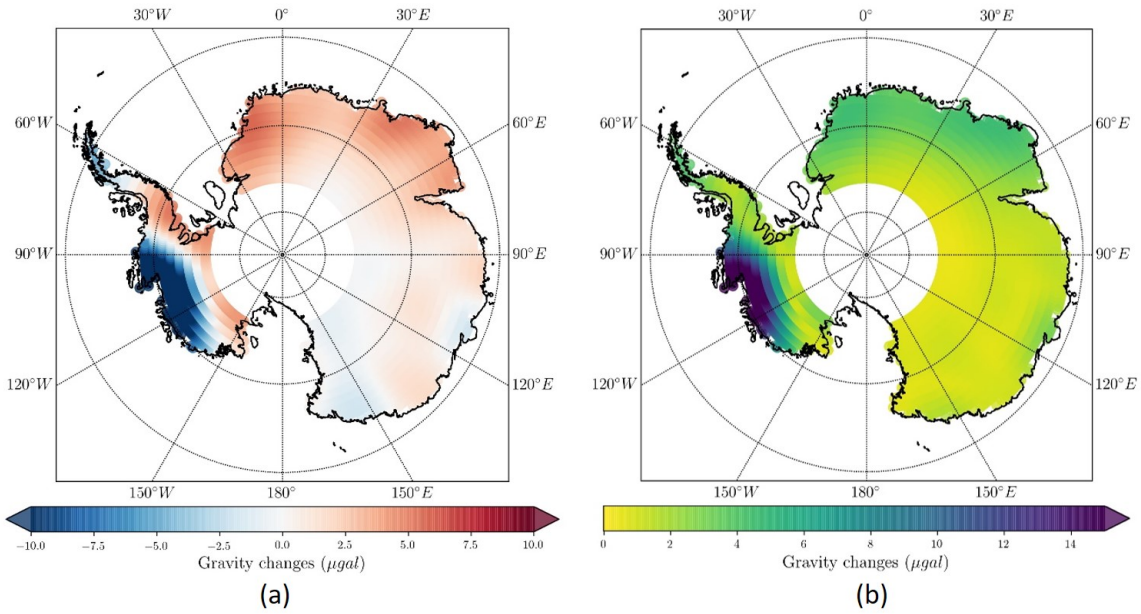

Figure 2.3: Mean (a) and standard deviation (b) of gravity changes (in μgal) observed using GRACE. Mean varies between -10 μgal (in blue) and 10 μgal (in red). Standard deviation varies between 0 μgal (in yellow) and 15 μgal (in violet).

period of time. Both differences and similarities exist in between measurements of changes from different GRACE solutions (figure 2.4). We use the average of the three GRACE solutions for the gravity potential in the further part of the studies as it increases the signal-to-noise ratio (SNR) of the time series [Sakumura et al., 2014]. How do we use changes in gravity to quantify changes in the ice sheet?

Bouguer reduction

In order to estimate changes in the height of the ice sheet based on changes in gravity measurements, Bouguer reduction can be employed. Bouguer reduction (named after Pierre Bouguer) of gravity involves complete removal of the topographic masses which refers to the mass outside the geoid. In this process, the area is assumed to be a Bouguer plate which is flat, horizontal and the masses between the geoid and surface have constant density ρ. Attraction, A of this plate is,

$$A = 2 * \pi * G * \rho * H \tag{2.1}$$

where G is the constant of gravitation ($6.67430 * 10^{-11} m^3 kg^{-1} s^{-2}$) and H is the thickness of the plate (in m) assumed to be with infinite area.

In this case, we alternatively use either of snow, ice or water density to make estimates of changes in snow, ice or water column height respectively and compare with other observations.

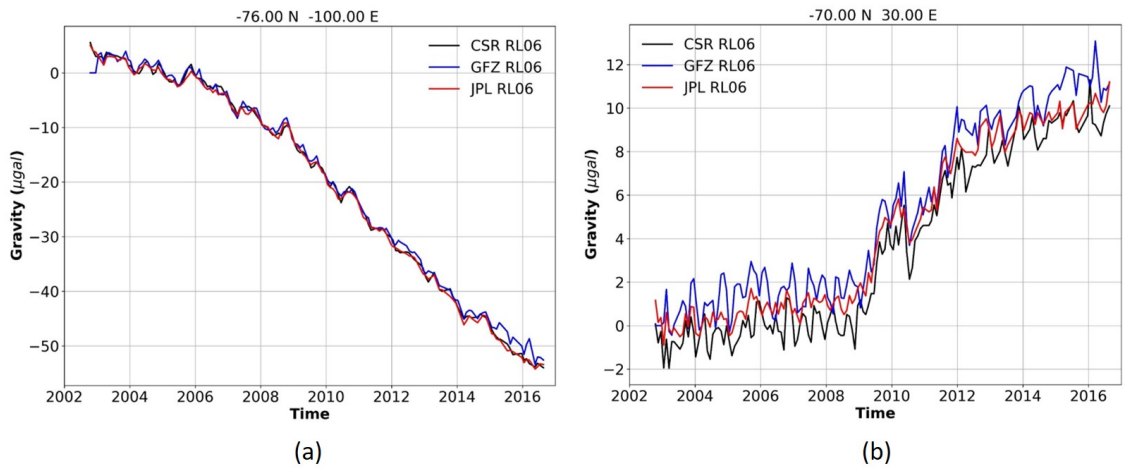

Figure 2.4: Time series of gravity changes in μgal for (a) PIG region and (b) DML region observed using GRACE mission during September 2002 to September 2016. Black (CSR), blue (GFZ) and red (JPL) represent different solutions. The abscissa is the time. The ordinate shows the gravity variations (in μgal), which varies in each subplot.

Consider changes in gravity is due to loss of snow. With standard density $\rho =$ 350 kg m^{-3},

$$\Delta A/\Delta t = 14.66 * \Delta H/\Delta t[\mu gal/s] \tag{2.2}$$

$$\Delta H/\Delta t = \Delta A/14.66[m/s]$$

Therefore, 1 μgal change in gravity over a period of time corresponds to approximately 6.82 cm of snow column height over the same period of time. Similarly, 2.4 cm of water column height or 2.6 cm of ice column height. This is not an accurate measure of changes in the ice sheet as we make it based upon several assumptions far from real world conditions including shape of the ice sheet and density of the matter which varies from that of snow to that of bedrock. However it gives an idea of magnitude of the changes.

Hence we convert the variations in the gravity potential to mass changes according to the assumption of the thin sheet layer [Wahr et al., 1998]. These mass changes can be converted into water equivalent height (WEH) variations which is a standard among global research community. Similarly, mass variations can be converted to ice equivalent height (IEH) or snow equivalent height (SEH) depending on the requirements to make analysis and comparisons.

Mean of WEH changes (in blue) from the three solutions for PIG and DML region is shown in figure 2.5. The quadratic trend represents the degree-2 polynomial fit of changes estimated (in black). This trend shows a general trend in the

changes and is reflective of the acceleration of present day ice sheet mass changes. PIG regions seems to loose mass whereas DML gains mass during 2002–2016 even though the magnitude of the changes are not the same.

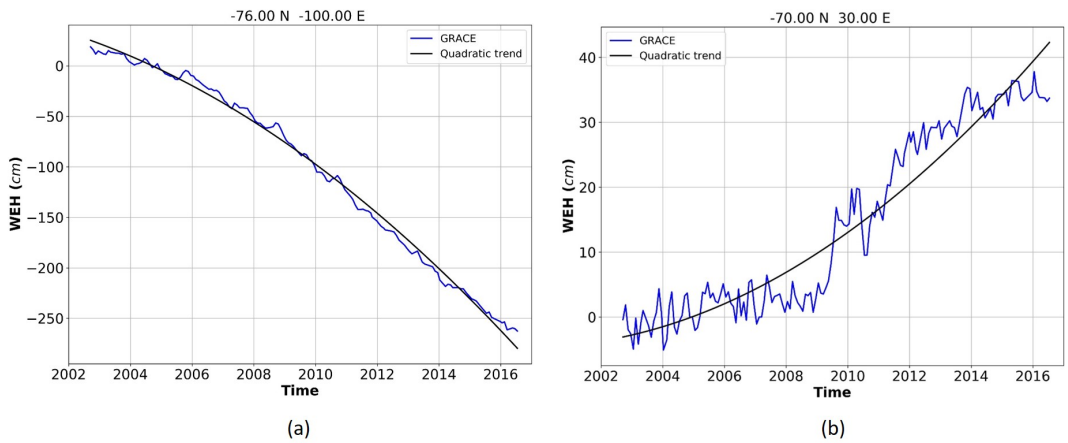

Figure 2.5: Time series of mean WEH changes in cm for (a) PIG and (b) DML region estimated from GRACE observations. The abscissa is the time. The ordinate shows the variations in WEH (in cm), which varies in each subplot.

The degree–2 polynomial fit of the estimated changes is removed to obtain the residual changes (figure 2.6). It can be expressed as changes in SEH or IEH or WEH depending on the density used to convert mass changes. In figure 2.6, SEH is represented in green whereas yellow and red correspond to IEH and WEH respectively. Both IEH and WEH are almost similar as there is not much difference in the standard density of ice and water.

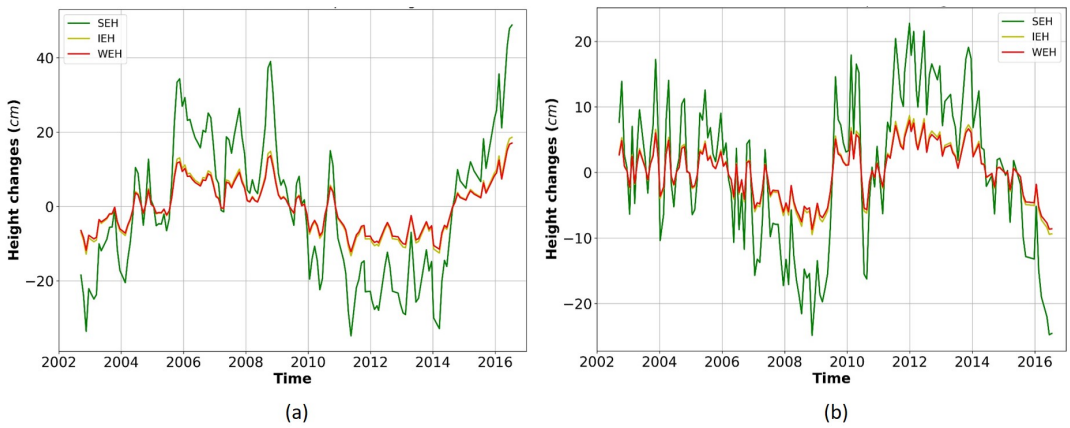

Figure 2.6: Residuals in SEH (in green), IEH (in yellow) and WEH (in red) at (a) PIG and (b) DML. The abscissa is the time. The ordinate shows the variations in WEH (in cm), which varies in each subplot.

The magnitude of variations is different between PIG and DML i.e., at PIG it

varies between -20 and 40 cm in SEH whereas at DML it is limited between -20 and 20 cm in SEH. The seasonal signal is not that clear as a lot of high frequency components seem to exist. This is better seen as the monthly means are plotted (figure 2.7) and there exist little differences in magnitude between adjacent months. At both regions, the signal peaks in October but with a minimal difference compared to the months close by.

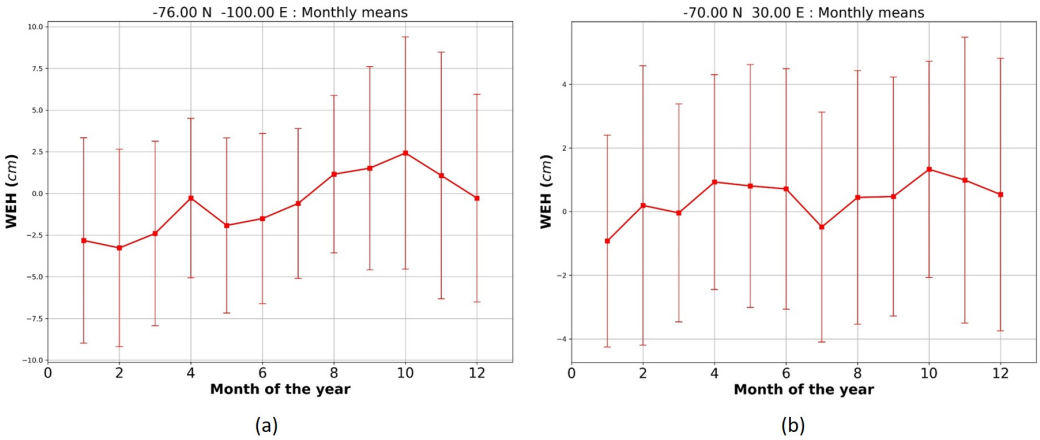

Figure 2.7: Monthly means of residual changes in WEH estimated from the GRACE solutions at (a) PIG and (b) DML. Error bars represent standard deviation (1 σ) from the mean. The abscissa is the time representing month of the year. The ordinate shows the changes in WEH (in cm), which varies in each subplot.

Standard deviation maps of residual changes give a larger picture of changes for the whole ice sheet for multiple time periods (figure 2.8). Magnitude of changes are lesser during 2002–2010 i.e., 0 to 4 cm in WEH (a) in comparison with 2002–2016 i.e., 0 to 6 cm in WEH (b). Once again, most of the changes happen in West Antarctica and in Antarctic Peninsula.

2.3 Satellite altimetry

2.3.1 Principle

In principle, a radar altimeter emits a radar wave in the nadir direction and has a sensor that receives the wave reflected from the surface. The surface height is derived combining the time duration of the travel and the accurate information of the satellite orbit. The sensor receives the energy backscattered from the surface and the subsurface which contains physical information about the media reflecting the radar wave when plotted with the arrival time as in figure 2.9. Thus the altimeter is

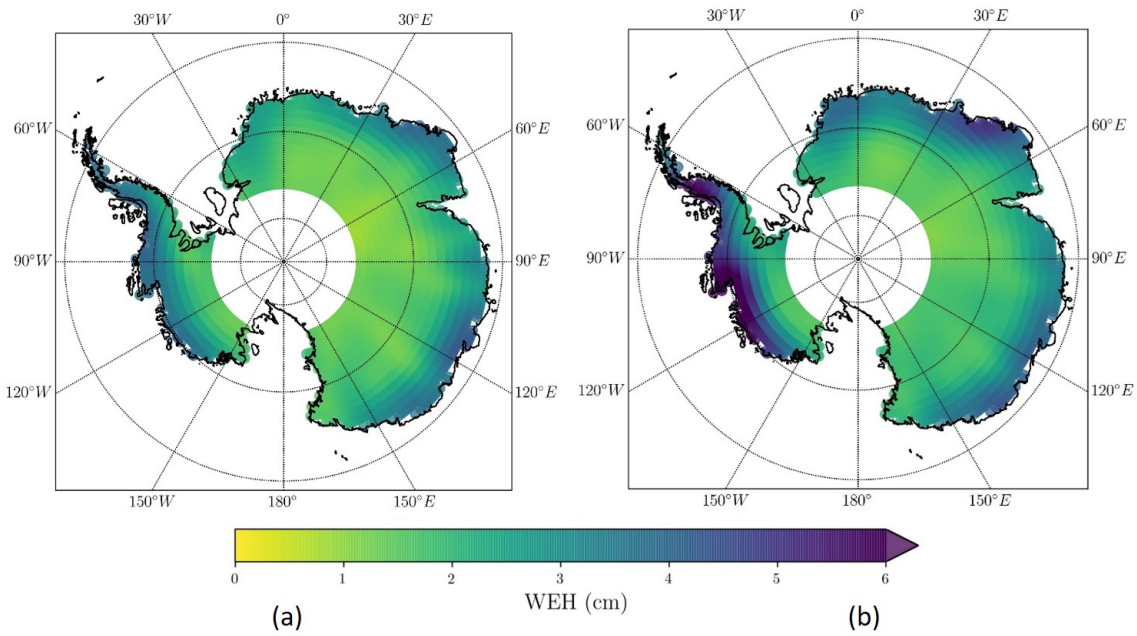

Figure 2.8: Standard deviation of residual changes in WEH (in cm) estimated from GRACE solutions during (a) Envisat period (2002 – 2010) and GRACE life time (2002 – 2016). Varies between 0 cm (in yellow) and 6 cm (in violet).

capable of providing the altitude, shape of the waveform with the parameters such as width of the leading edge and slope of the trailing edge and the total amount of energy backscattered from the surface.

Altimetric measurements are subject to instrument bias, terrestrial and oceanic tides, etc. and to delays in propagation due to atmosphere and ionosphere. The error budget when applied to continental surfaces like ice sheets is greater in comparison with sea surface topography and need some specific corrections [Remy & Parouty, 2009]. The dual-frequency altimeters used above the oceanic surface to correct for the wet troposphere and for the ionosphere induced delays were affected by snow surface signature from the ice sheets and failed to deduce atmospheric wetness and electronic content. In K_u band (13.6 GHz or wavelength of 2.3 cm), the classical altimetric band penetrates into both dry and cold snowpack and the reflection comes both from the surface (called the surface echo) and subsurface layering (volume echo) [Ridley & Partington, 1988]. Apart from the previous limitations, kilometric-scale topographic features and surface slope induces several problems as when the topography is not flat, the emitted wave gets reflected from upslope direction of the surface rather than the nadir [Brooks et al., 1978, Brenner et al., 1983]. This complicates measurement of changes near the coasts of Antarctica.

Initial attempts of mapping ice sheets using altimetry started in the late 70s and the mid-80s using Seasat (1978) and Geosat (1985–1990) missions which had an

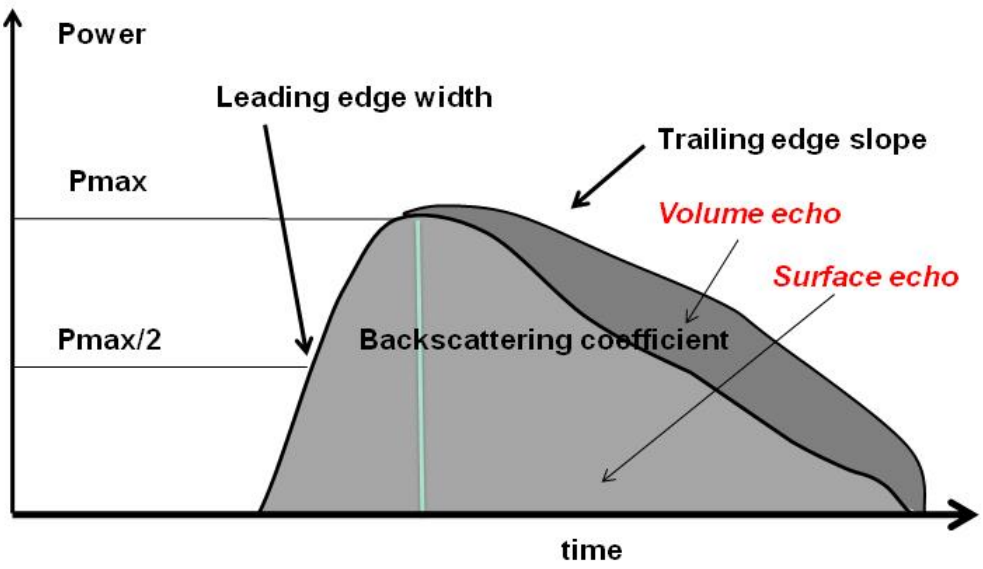

Figure 2.9: Altimetric waveform shape from Remy & Parouty [2009]. Altimetric observations also provide the return waveform which is the histogram of the backscattered energy with respect to time. The signal is the combination of a surface echo (in light grey) and of a volume echo (in dark grey).

inclination angle of 72 degrees and covered only the south of the Greenland ice sheet and a small section of the AIS [Brenner et al., 1983, Zwally et al., 1983]. European Remote Sensing Satellite (ERS-1), launched by the European Space Agency (ESA) in 1991, served as the first polar-orbiting satellite with a radar altimeter. Later, ERS-2 launched in 1995 and started covering large polar areas. It also had a high spatial resolution of 350 m along the satellite track and was operating in multiple repeat cycle modes to obtain a dense sampling of ice sheets. The Envisat mission launched in 2002 had dual-frequency altimeter (S and K_u-bands) for polar observations and had repeat cycle similar to ERS-1 (1991–1996) and ERS-2 (1995–2003) i.e., 35 days. Other missions launched to monitor polar regions include ICESat (Ice Cloud and land Elevation Satellite) launched by NASA (The National Aeronautics and Space Administration) in 2003, followed by ICESat–2 (since 2018-) which are LASER altimeters with reduced penetration of the input wave into snowpack and footprint as in the case of microwave signals. ALtiKa onboard the SARAL (Satellite with ARgos and ALtiKa) mission (since 2013-), a Indo-French mission, working in K_a band instead of K_u (or 35 GHz or wavelength of 0.8 cm instead of 13 GHz), too has the penetration reduced but the altimeter is very sensitive to surface slope or undulations. CryoSat–2 (since 2010-) and Sentinel–3 (since 2016 -) missions were launched by ESA has SAR (synthetic aperture radar) altimeters and has reduced penetration and footprint. Figure 2.10 gives an overview of various polar topography altimeter missions which operates at present, operated in the past and is planned

for the future [Kern et al, 2020].

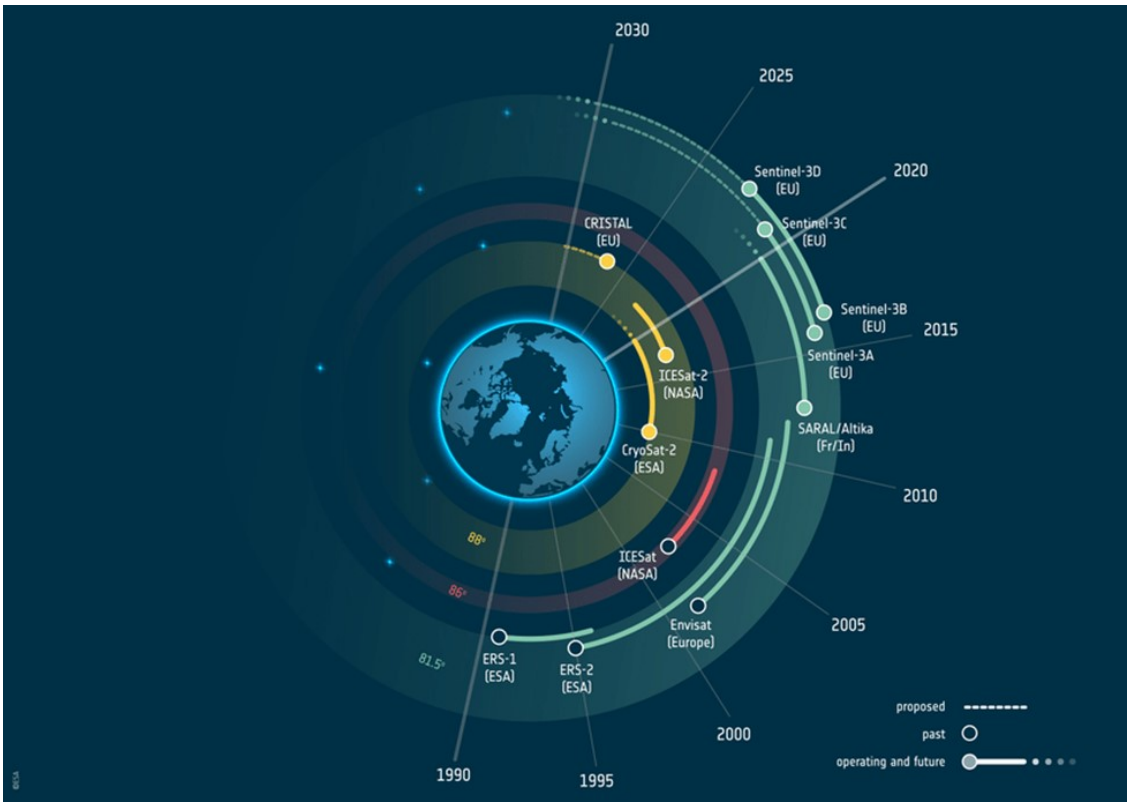

Figure 2.10: Past, operating, approved, and proposed polar topography altimeter missions [Kern et al, 2020].

Apart from polar studies and monitoring ice sheets, radar altimetry provides valuable information for other global geoscientific studies. Altimetry data over ocean are used to monitor mean sea levels, wave height, wind speeds, and surface topographical features. The success of altimetry missions has promoted the development of future missions that will provide more accurate data sets.

2.3.2 Altimetry data processing

As we discussed earlier, multiple missions have been monitoring changes in elevation of the ice sheet since 1990s. A robust common processing strategy is required to ensure seamless processing of data from multiple missions over time as the mission properties vary.

The first step consists in the retrieval of surface height from the waveform. Few algorithms, namely retrackings, are devoted to this. This is illustrated in figure 2.11. We use the retracking algorithm from LEGOS (Laboratoire d'Etudes en Geophysique et Oceanographie Spatiales), ICE-2 [Legresy et al. 2005].

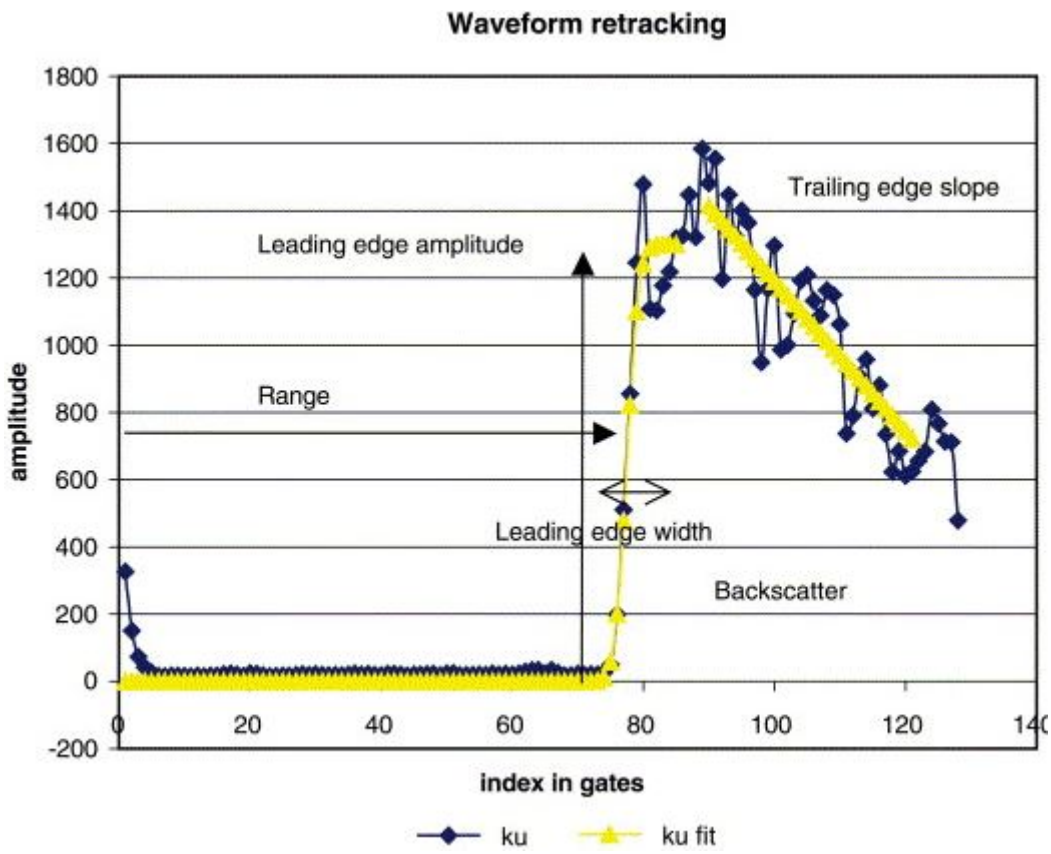

Figure 2.11: The altimetric waveform is represented in blue alongside the retracking fitting function (in yellow). The variables extracted from the altimetric waveform like range, leading edge width and amplitude, and trailing edge slope are shown. Adapted from Legresy et al. [2005].

The leading edge is fitted using an error function (erf) and the impact point is interpolated at the middle of the leading edge. The slope error is corrected from a topography map. The slope and the correction are estimated by iteration. Wind, snow compaction, or temperature affect both the surface and volume echo, so the height retrieval. Some of them are corrected when temporal changes are estimated. In Envisat's case there are 85 repeat cycles. 85 data sets are fitted with :

1. the altimeter backscatter, the leading edge, the trailing edge slope, in order to correct for the temporal change of the snowpack characteristics.

2. a 2-D polynomial depending on along and across-track direction in order to correct for surface small-scale topography and from across-track misrepeat. The main outputs are: the Leading edge amplitude (LeBs), the corrected range, the leading edge width (LeW), the trailing edge slope (TE) and the backscatter coefficient (Bs) corresponding to the waveform integration.

3. a time vector in order to deduce the trend.

So there is 85 equations with 9 unknowns or variables.

Height trend extraction from radar altimetry data usually uses only cross-over points. But along track processing methodology allows the use of different orbits like the geodetic mission of ERS-1 with the 35-day orbit to eliminate the problem of cross-track slope. The density of the data available is much higher. For one repeat cycle, about 80000 valid cross-over points are available over the AIS whereas 1.8 million points can be used after along-track editing and dedicated analysis. Especially near the coast along track processing allows availability of more data points even though with correction for cross-track slope in comparison with the cross-over analysis [Remy et al., 2014].

Along-track data are given at each 370 m. Points are processed at 1 km intervals as the repeat tracks lie within 1 km of the nominal track. At each location, 3 long track consecutive data exists for 85 repeat cycles. The error due to across-track topography is fixed by fitting a quadratic form in x and y whereas change in snow-pack characteristics is corrected by fitting the back-scatter and the two waveform shape parameters (leading edge width and trailing edge slope) [Remy et al., 2012]. 10 unknown parameters are fitted with about 500 observations and the temporal trend is inverted with robustly [Flament and Rémy, 2012]. Finally the processing provides the mean values of height, back-scatter, two waveform parameters, the temporal derivatives of these four parameters, and the residuals corresponding to the 85 cycles. Time series for each parameter are then obtained by re-trending the temporal residues [Remy et al., 2014].

2.3.3 Height changes from Envisat observations

Radar altimeter onboard the Envisat mission directly measure the elevation changes happening to the ice sheets. It was operational between September 2002 and October 2010 with measurements up to 81.5° S. Measurements on March 2004 is taken as the reference elevation as it corresponds to the first cycle with the most complete coverage [Memin et al., 2014]. Further on, along-track processing is employed that allows a dense data set, and grids of 5 km resolution are binned to 0.25° × 0.25° resolution grids [Flament & Remy, 2012; Memin et al., 2014].

Envisat data undergo GRACE-like processing so that we have homogeneity with GRACE solutions [Memin et al., 2014]. The aim is to obtain region–averaged elevation changes from monthly maps of elevation changes in AIS. This involves transferring maps of AIS elevation changes to the spherical harmonic domain by limiting the cut-off degree to n=50, followed by low-pass filtering with a cosine taper decreasing from 1 at n=30 to 0 at n=50 [Memin et al., 2011].

We obtain monthly maps of elevation changes on a 1° × 1° grid providing 2959-time series. Similar to figure 2.3, mean and standard deviation of changes in ele-

vation estimated from Envisat observations during 2002–2010 is shown in figure 2.12.

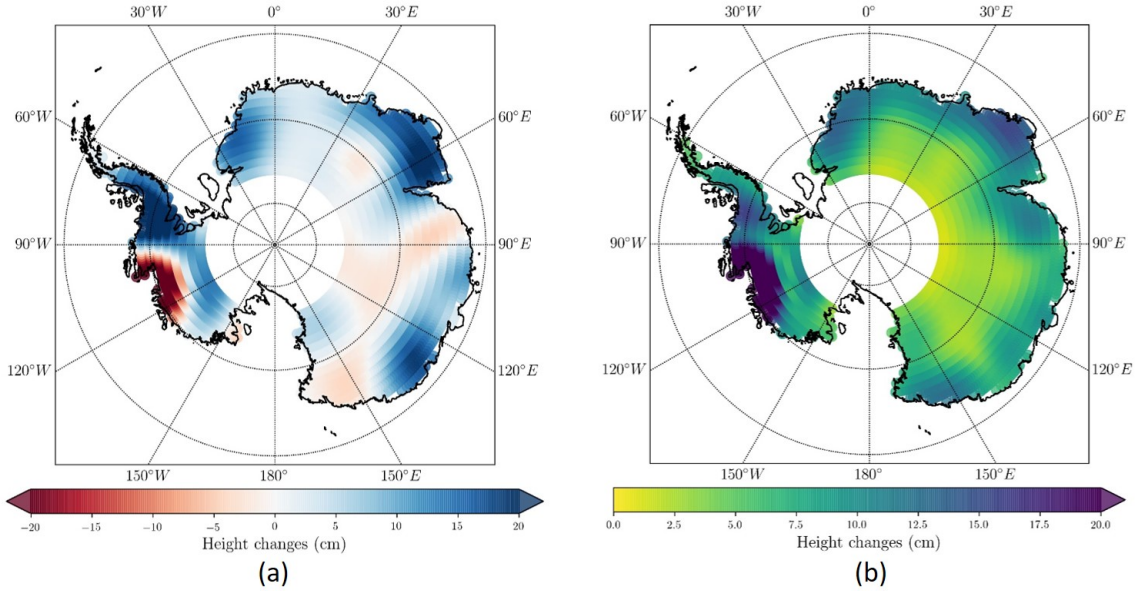

Figure 2.12: Mean (a) and standard deviation (b) of elevation changes (in cm) estimated using Envisat. Mean varies between -20 cm (in red) and 20 cm (in blue). Standard deviation varies between 0 cm (in yellow) and 20 cm (in violet).

Figure 2.12 and figure 2.3 depict similar patterns. Changes in the height take place mostly along the coast and the magnitude varies regionally. The mean of the height change observations is largely positive or slightly negative across the ice sheet apart from coastal regions in West Antarctica between 90 W and 130 W where it is largely negative. The standard deviation of the observations too is high indicating large scale variability in this region. Regions in the interiors of East Antarctica with negative mean and low standard deviation is found and needs further study for explaining. Further analysis is carried out using estimates at PIG and DML region as done in section 2.2.3.

Time series of height changes (in blue) from two different regions PIG and DML are shown in figure 2.13. We fit a degree–2 polynomial which represent the trend (present day and past) and the acceleration of present-day ice sheet mass changes resulting from a combination of changes in the height of snow and ice. This quadratic fit is subtracted from the original signal to obtain the residual changes (in red) in the elevation of the ice sheet as our focus is largely on understanding the temporal variability of the AIS features.

Height changes from these regions has differing trends as elevation seems to reduce at PIG region whereas it seems to increase in DML. Differences exist in the magnitude of the residual changes. In PIG, it varies between -20 and 25 cm whereas

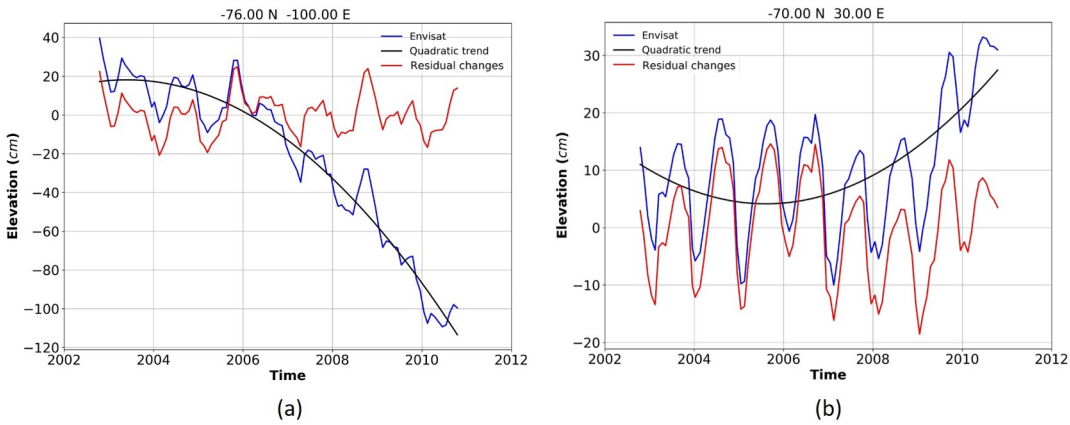

Figure 2.13: Time series of elevation changes in centimeters for (a) PIG and (b) DML estimated from Envisat observations during September 2002 to October 2010 in blue. The best-fitting quadratic trend is shown in black. Residual changes at each region is represented in red. The abscissa is the time. The ordinate shows the elevation changes (in cm), which varies in each subplot.

in DML, this variation is limited between -15 and 15 cm. The seasonal nature of the temporal changes too is very much evident at both regions as we see eight peaks and eight troughs with almost similar intervals during eight years of observation. Since the observations are available at monthly interval, we compute the monthly means of the residual changes to see the trends of seasonal behavior (figure 2.14). Elevations peak in tenth month or October in PIG region while it peaks in ninth month or September in DML region.

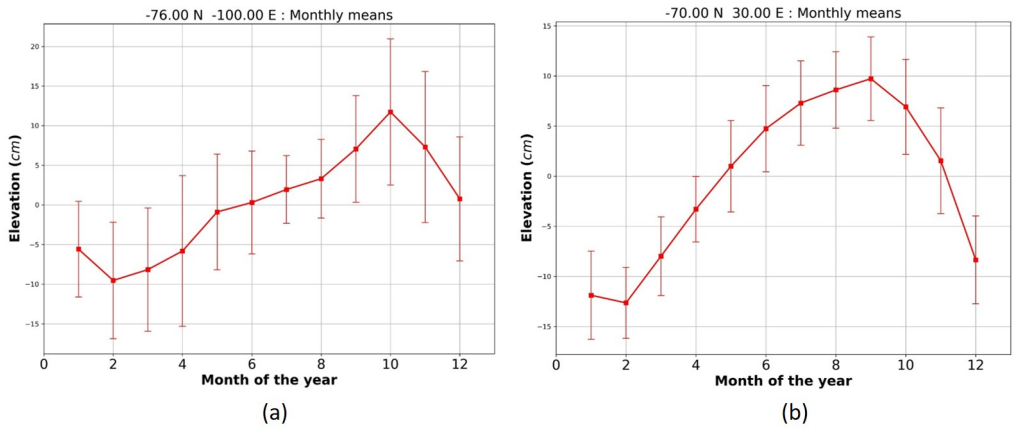

Figure 2.14: Monthly means of residual elevation changes estimated from the Envisat observations. Error bars represent standard deviation (1 σ) from the mean. The abscissa is the time representing month of the year. The ordinate shows the elevation changes (in cm), which varies in each subplot.

In order to understand the changes other than at these two regions, we computed the standard deviation of the residual changes in elevation for the whole AIS (figure

2.15). It gives major insights of changes in elevation across the AIS. The standard deviation map indicates areas where we have maximum deviation from the mean (up to 10 cm) in the elevation. Changes are majorly observed in West Antarctica, Antarctic Peninsula and along the coasts in East Antarctica.

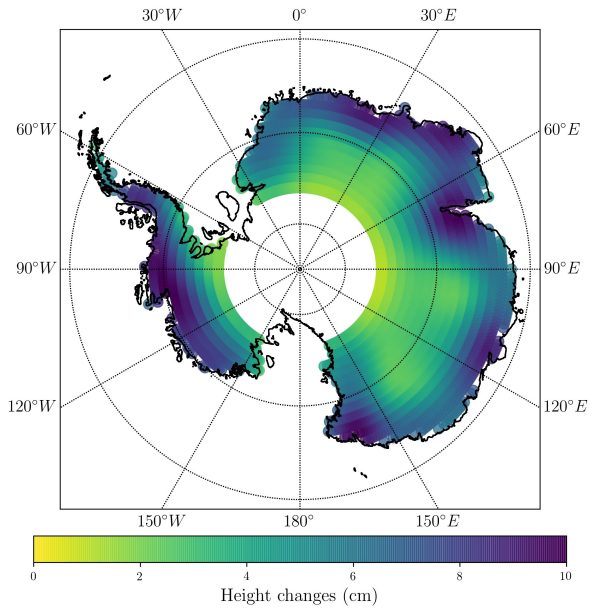

Figure 2.15: Standard deviation of residual changes (in cm) estimated using Envisat observations. Varies between 0 cm (in yellow) and 12 cm (in violet).

Estimates of changes from GRACE and Envisat exhibit both similarities and differences. It is important to note that they use completely different techniques to quantify changes to the ice sheet. Similarities were found in the spatial pattern of changes occurring throughout the AIS. But there exist differences in the magnitude of these changes which can be either a loss of mass or a gain of mass to the ice sheet. Seasonal changes were more clear in observations from Envisat whereas a lot of high frequency variations were found in GRACE observations. Even though both of them are spaceborne geodetic measurements their sensitivity or ability to correctly quantify changes due to a particular process varies. Since AIS is being driven by multiple processes over time, gaps exist between estimates made from geodetic measurements of the AIS. We use outputs from a climate model to make estimate of changes which will indicate a possible climate origin in the next chapter.

Chapter 3

Height changes from modelling

A model usually tries to copy or replicate a physical system. In this context, models are used to estimate parameters to characterize, understand and predict changes of the AIS due to several reasons. This includes lack of observations both in situ and remotely sensed and limitations of the remote sensing systems. There existed inter–mission gaps which refers to period when there are no observations between two adjacent missions. Limitations existed locally too such as limited usability of popular remote sensing observations over the Antarctica Peninsula (AP) due to its topography and size. The resolution of GRACE observations does not resolve the larger glacier basins in the AP region. Other techniques such as radar or laser altimetry are inaccurate over the steep mountain slopes where surface features are complex, and where abundant cloud cover blocks laser signals. Evolution of high performance computing and measurements or observations from other associated systems has helped in developing models which use quantitative methods to simulate the interactions or processes between the different physical systems. These models often give data for longer periods including times when direct measurements are not available and can be improved over time with availability of new information on these systems.

3.1 Climate Model

Numerical climate models with the help of quantitative methods simulate the interactions or processes between the important drivers of climate, such as atmosphere, hydrosphere, lithosphere, and cryosphere, using physical relations [Cullen, 1993]. General circulation models (GCMs) are a common tool in climate research. GCMs provide continuous time-series of atmospheric processes at a regular grids for the whole world and address the limitations of observational data. They can be used to estimate the AIS SMB in the past [Pollard, 2000], present-day [Bromwich et al., 1995; Van den Broeke, 1997; Lenaerts et al., 2015] and future [Turner et al., 2005]

by applying proper boundary/forcing conditions. But they are also subject to deficiencies with regard to the polar regions as they poorly represent processes related to polar ice and snow (like albedo and subsurface snow processes), and has coarse horizontal grid resolution (∼100 km) to accurately simulate topography related variables, such as precipitation and katabatic winds [Genthon & Krinner, 2001].

It will be computationally demanding for GCMs to accurately resolve these processes by increasing their horizontal resolution. Therefore, similar models can be applied regionally, with higher horizontal resolution and forcing at the boundaries using coarser GCM. These regional climate models (RCMs) can be adapted locally and have been used over Antarctica, to support field operations [Bromwich et al., 2005] and to simulate the interaction of the ice sheet with sea ice at regional-scale [Bailey & Lynch, 2000]. They can be forced by reanalyses where observations are assimilated in a regular grid and used to obtain longer simulations over Antarctica and understand the changes in climate [Bracegirdle & Marshall, 2012]. This involves thorough understanding of the surface energy balance (SEB), which explains the heat transfer and moisture transport at the Earth's surface. RCMs serve as important tools to improve our existing understandings of the polar SEB.

The SEB is expressed as:

$$M = SW_{net} + LW_{net} + SHF + LHF + G \tag{3.1}$$

where M is melt energy (M=0 Wm^{-2} if the surface temperature $T_s < 273.15$ K), SW_{net} and LW_{net} are the net short and long wave radiative fluxes, SHF and LHF are respectively the sensible and latent heat fluxes and G is the subsurface conductive heat flux. The fluxes directed towards the surface are defined positive and is in Wm^{-2}.

Modelled SMB trend during 1958-2007 for the Greenland ice sheet (GrIS) from the Regional Atmospheric Climate Model (RACMO2/GR) [van Meijgaard et al., 2008] is shown in figure 3.1. The model was applied over a domain that includes the GrIS and its surrounding oceans and islands at unprecedented high horizontal resolution (∼11 km).

Several RCMs have been used over the AIS based on this principle: the AMPS (Antarctic Mesoscale Prediction System) model, also known as Polar MM5 or its successor Polar WRF, has been used for Antarctic forecasts and hindcasts, but simulation lengths are usually limited (∼3 years) and are limited to specific regions [Bromwich, 2004]. The Regional Atmospheric Climate MOdel (RACMO) is the only model that has been extensively used to perform long (> 10 years) climate runs over Antarctica. The first extended (1980–1993) run with RACMO over the AIS

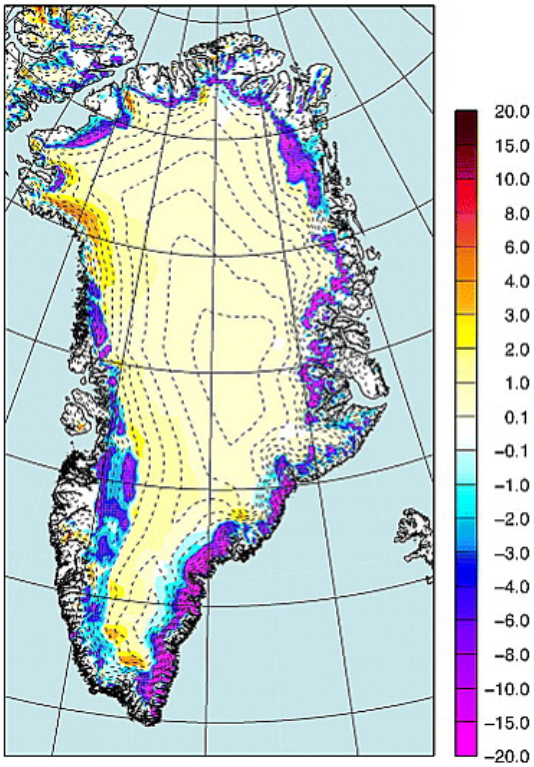

Figure 3.1: Modelled surface mass balance trend (1958–2007) in kg m^{-2} from Ettema et al., [2009]. Thin dashed lines represent 250 m elevation contours from Bamber et al., [2001].

was forced by data from the European Centre for Medium Range Weather Forecast (ECMWF) 15-year re-analysis (ERA-15) [Van Lipzig et al., 2002]. Improvements on AIS simulations like the implementation of a sophisticated snow scheme that calculates snow grain size and albedo, an increase of the simulation length ($>$ 30 years), and an increase of the horizontal resolution (27 km) happened with newer versions of RACMO and its forcings [Reijmer et al., 2005; Van de Berg et al., 2005; Lenaerts et al., 2012a].

In 2018, RACMO2.3p2 the updated regional climate model came into existence with a new, high-resolution data set of the contemporary near-surface climate and SMB of the AIS [van Wessem et al., 2018]. It had higher resolution for AP ($\sim$ 5.5 km) to better resolve the topography and other related variables. The model is a combination of two commonly used atmospheric models: the High Resolution Limited Area Model (HIRLAM) [Undén et al., 2002] and the European Centre for Medium-RangeWeather Forecasts (ECMWF) Integrated Forecast System (IFS) [ECMWF-IFS, 2008].

Other than SMB, the model provides with outputs like accumulation, precipitation, surface pressure, temperature, wind velocities, etc. The near-surface wind, temperature and SEB are compared with observational data from 9 AWS, run by the Institute for Marine and Atmospheric research of Utrecht University (UU/IMAU).

The spatial changes in SMB are evaluated using SMB observations from in-situ and ice balance velocities, and its temporal variability using GRACE estimates. The in-situ observations and balance velocities indicate a clear improvement in the spatial representation of the SMB in the interiors of East Antarctica whereas no improvements are seen for West Antarctica and the coastal regions [van Wessem et al., 2018]. The modelled temperature and wind climate at higher resolution of the Antarctic Peninsula is evaluated with near-surface temperature and wind measurements from twelve stations with AWS and manned observations combined with vertical profiling using balloon soundings at three stations. Similarly, SMB is validated with 132 in-situ SMB observations and discharge rates from drainage basins of 6 different glaciers. Limitations include, those related to the cloud microphysics, the horizontal resolution and partly to the melt-water percolation scheme in the snow model.

3.2 Height changes from RACMO2.3p2 outputs

A region or site in an ice sheet undergoes changes due to occurrence of several competing processes at varying time scales as discussed earlier. Outputs from a RCM is usually representation of various processes in that region like wind velocity reflect the presence or absence, magnitude and direction of wind. Therefore, changes to an ice sheet can be quantified using outputs from a RCM like RACMO2.3p2. Changes in the elevation of an ice sheet can be symbolically represented as a combination of multiple processes as shown in figure 3.2.

Surface elevation changes can be attributed as due to processes like accumulation, firn compaction, ablation, ice motion, and bedrock upliftment as in figure 3.2 [Zwally & Li, 2002]. It (in m/a) can be represented as:

$$\frac{dH(t)}{dt} = \frac{A(t)}{\rho_{sf}} + V_{fc}(t) + \frac{A_b(t)}{\rho_i} + V_{ice} + \frac{dB}{dt} \tag{3.2}$$

where accumulation rate, A(t) (in kg $m^{-2}a^{-1}$), is the component that increases the surface height at a rate of $\frac{A(t)}{\rho_{sf}}$ and ρ_{sf} is the density of the surface snow (in kg m^{-3}). $A_b(t)$ is the ablation rate (in kg $m^{-2}a^{-1}$) occurring only in the ablation zone and ρ_i is the density of the ice (in kg m^{-3}). V_{ice} represents the vertical velocity component of the ice at the firn or ice transition (in m a^{-1}). $\frac{dB}{dt}$ is the component representing vertical motion of the underlying bedrock (in m a^{-1}). $V_{fc}(t)$ is the velocity of firn compaction at the surface (in m a^{-1}), which is defined as the integral of the displacement of the firn layers over the length of the firn column [Li & Zwally, 2011; Li & Zwally, 2015]. This component at depth z is given by the density, ρ(z), and compaction rate, dρ(z)/dt, is expressed as,

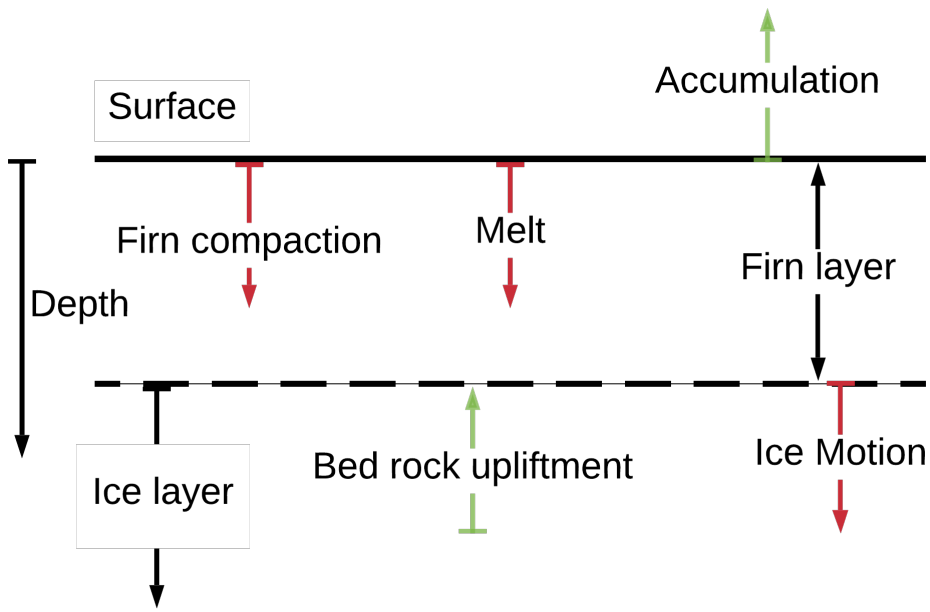

Figure 3.2: Symbolic representation of height changes of an ice sheet. Green components like accumulation and bed rock upliftment cause positive changes whereas red components (firn compaction, melt and ice motion) cause negative changes.

$$V_{fc}(z,t) = \int_{z^i}^{z} \left[\frac{d\rho(z)}{dt} \right] dz \tag{3.3}$$

where z_i is the transition depth between firn and ice where the density of firn is close to density of the ice ($\sim$ 917 kg m^{-3}). Contributions from accumulation and bed rock upliftment is positive whereas those from firn compaction, melt and ice motion is negative (figure 3.2).

But in simpler terms, height fluctuations of the ice sheet elevation with respect to the equilibrium shape over short periods is directly linked to the fluctuations of the accumulation rate as assumed by Remy & Parrenin [2004]. Hence equation 3.2 becomes,

$$\frac{dH(t)}{dt} = \frac{A(t)}{\rho_i} + V_{ice} \tag{3.4}$$

According to them, changes in bed rock elevation (bed rock upliftment), is of the order of 1 mm/year at most, and can be neglected. In this method, firn densification process and melting is not considered and finally temporal changes in height of the ice sheet is left to variations in the accumulation rate.

Here, SMB product from the climate model is considered as the input for estimating height changes as it combines information from multiple surface processes like accumulation, sublimation, erosion, meltwater run–off, etc. Even SMB product from the climate model undergoes GRACE like processing (discussed earlier).

Height changes estimated from the SMB product by this method for PIG and DML is shown in figure 3.3.

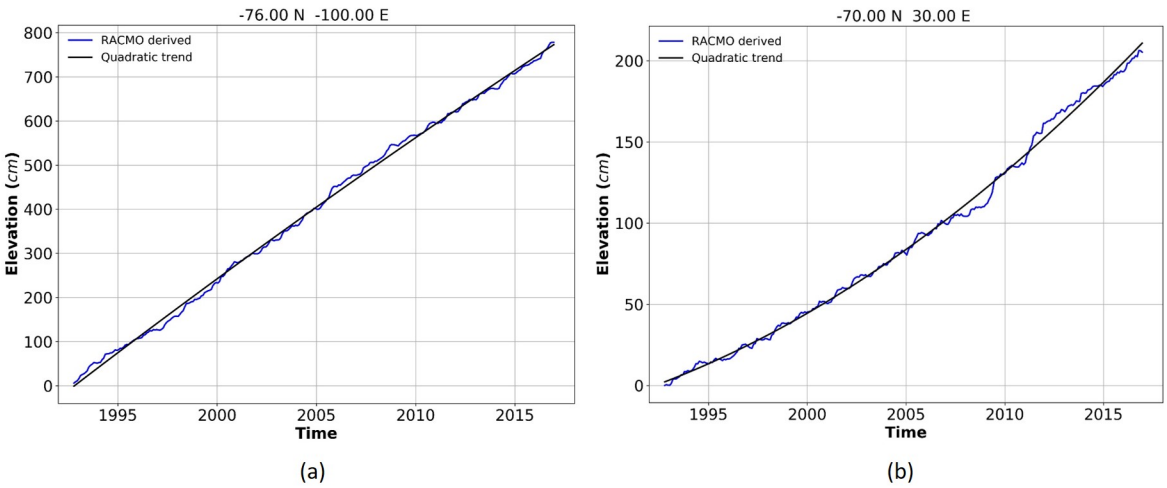

Figure 3.3: Time series of elevation changes in cm for (a) PIG and (b) DML estimated using outputs from RACMO2.3p2 during 1992–2016. The abscissa is the time. The ordinate shows the variations in WEH (in cm), which varies in each subplot.

Height change estimated using RACMO outputs show similar trend of gaining mass during the period 1992–2016 at PIG and DML region even though the magnitude varies largely. The trend at PIG (figure 3.3 a) is different and in the opposite direction compared to estimates made from GRACE and Envisat (figure 2.5 & figure 2.13). This can be attributed to lack of ice discharge component while making estimates using the SMB product from RACMO2.3p2. The quadratic fit is subtracted to obtain the residual changes (in red) and is plotted alongside the variations in SMB (in yellow) (figure 3.4). Height varies between -20 and 20 cm in PIG whereas only -10 to 10 cm in DML which can attributed to the differences in the magnitude of variations in SMB at both these regions (-20 to 100 kg m^{-2} in PIG and -10 to 50 kgm^{-2} in DML).

The seasonal signal is quite clear even though the SMB variations (in yellow) seems too noisy (figure 3.4) due to a lot of high frequency components. The seasonal variations in height changes is clearly visible in the monthly means plots (figure 3.5) as we see a continuous upward trend to the peak and downward trend after the peak. At PIG, the signal peaks in October whereas it peaks in August at DML. There are differences in the magnitude too as these regions are subject to differences in SMB.

We compare height changes estimated from the climate model with that es-

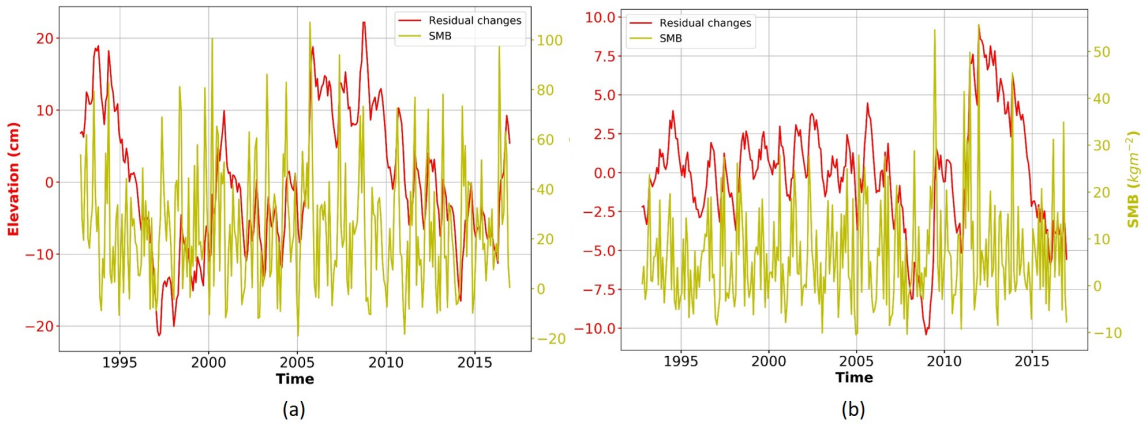

Figure 3.4: Residual changes in elevation (in red) and SMB (in yellow) at (a) PIG and (b) DML. The abscissa is the time. The ordinate shows the variations in elevation (in cm) and SMB (in kg m^{-2}), which varies in each subplot.

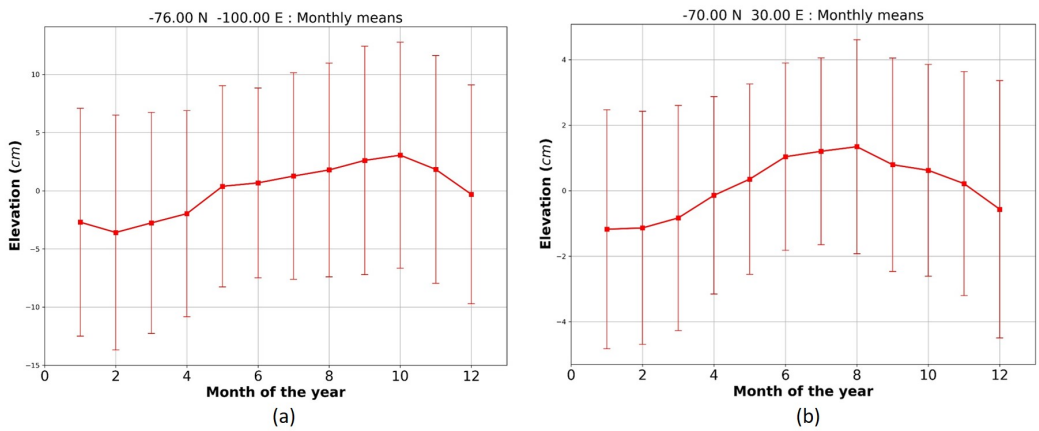

Figure 3.5: Monthly means of residual changes estimated from RACMO outputs at (a) PIG and (b) DML. Error bars represent standard deviation (1 σ) from the mean. The abscissa is the time representing month of the year. The ordinate shows the changes in elevation (in cm), which varies in each subplot.

timated from altimetry mission (in this case Envisat) or estimates from GRACE solutions (figure 3.6).

Height change estimates made using this assumption does not take into account of firn compaction that also induces height changes [McConnell et al., 2000; Helsen et al., 2008]. It is important to incorporate variations in surface temperature and firn densification for which we use a firn densification model.

3.3 Firn densification model

A firn densification model (FDM) aim at modelling the transformation of snow into glacial ice, which is one of the most fundamental processes in glaciology. In glaciol-

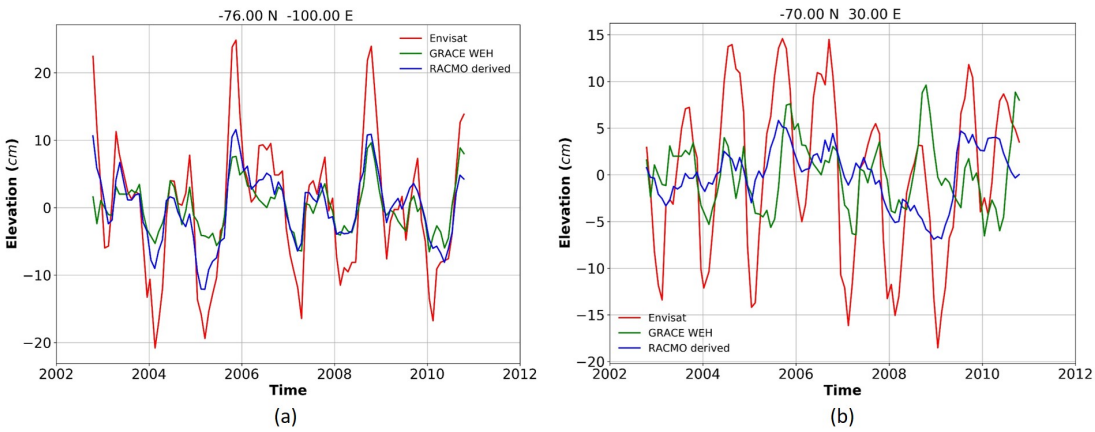

Figure 3.6: Height changes at (a) PIG and (b) DML from Envisat observations (in red), GRACE observations in WEH (in green) and RACMO (in blue). The abscissa is the time. The ordinate shows the variations in elevation (in cm), which varies in each subplot.

ogy, it serves several applications which include converting ice-sheet elevation change measurements to mass change, interpreting climate records in ice cores, estimating elevation change from climate model outputs, etc. In figure 3.7, a schematic representation of a firn densification model is given [Ligtenberg et al., 2011]. At the surface, snow and various processes happening are shown; precipitation (P), surface sublimation (SU_s), drifting snow sublimation (SU_{ds}) and erosion/deposition (ER_{ds}) and surface melt (Me). Downwards from the surface, snow gets denser and more compact and becomes ice at the bottom as it undergoes processes like densification, percolation, retention, refreezing, etc. The vertical column including snow, firn and up to ice is often referred as firn layer or firn column. Due to the varying surface climate conditions in the AIS, characteristics of the firn layer is subject to large range of variations in both space and time [Zwally and Li, 2002; Van den Broeke, 2008; Helsen et al., 2008]. The thickness of the firn layer can vary between nil in areas where sublimation, drifting snow erosion and/or melt exceed snowfall (ablation areas) to a few tens of meters in the relatively warm coastal areas to few hundreds of meters in the cold interiors of East Antarctica. The steady and transient states of the firn layer provide important information on firn air content and surface elevation changes which serve as crucial parameters to estimate the contemporary mass balance of the AIS using remote-sensing techniques [Rignot et al., 2008; Helsen et al., 2008; Van den Broeke et al., 2008]. Firn compaction velocity component can be resolved using firn densification models and climate model outputs like temperature, snowfall, melt, etc. to estimate changes in firn depth and density [Ligtenberg et al., 2011]. Later, these can be used to convert satellite elevation change measurements to mass changes [Davis et al., 2005; Wingham et al., 2009].

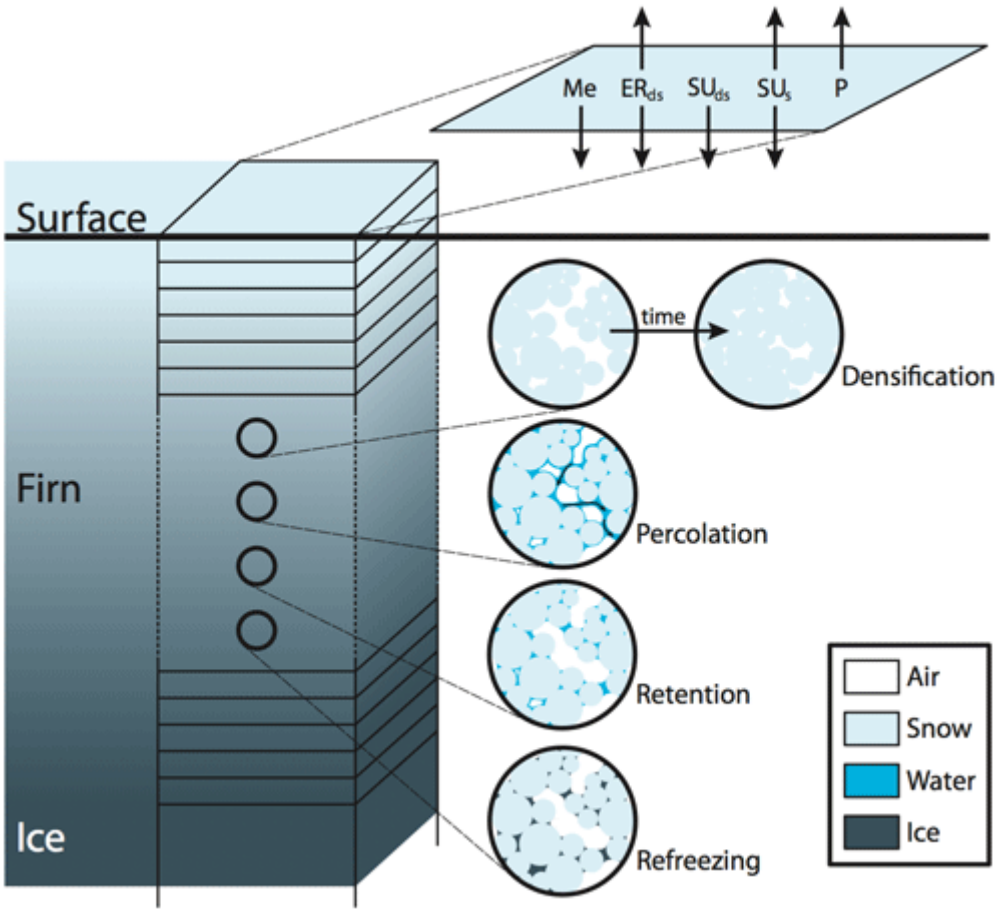

Figure 3.7: Schematic representation of the firn densification model (FDM) by Ligtenberg [2011]. At the surface the mass adding (arrow up) and mass removing (arrow down) SMB components are shown: precipitation (P), surface sublimation (SU_s), drifting snow sublimation (SU_{ds}) and erosion/deposition (ER_{ds}) and surface melt (Me). The four circles schematically illustrate the processes that are calculated within the model firn layer: firn densification and percolation, retention and refreezing of meltwater.

A number of theories exist for the dry densification of snow and firn since the 1950s and they lacked a clear understanding of the relative importance and contribution of possible component processes such as settling, re-crystallization, sublimation, volume and surface diffusion, etc. [Benson, 1959; Benson, 1962; Bader, 1962; Kojima, 1964]. Several firn densification models exist [Wilkinson, 1988; Herron and Langway, 1980; Barnola et al., 1991; Helsen et al., 2008; Arthern et al., 2010; Ligtenberg et al., 2011]. They work based on differing principles; Wilkinson [1988] is based on physical principles whereas Herron and Langway [1980], Barnola et al [1991], Helsen et al [2008] and Arthern et al [2010] use semi-empirical parameterizations. Some models have steady state density profile while other models simulate changes in the firn layer over time. Time-dependent firn densification models like Helsen et al. [2008] and Arthern et al. [2010], are both based on the model of Herron

and Langway [1980]. Arthern et al. [2010] was tuned to fit steady-state density profiles from Greenland and Antarctica with the assumption that firn compaction has an Arrhenius-type temperature sensitivity. Zwally and Li [2002] were able to add a different temperature sensitivity. This was later modified by Helsen et al. [2008] to make it suitable for Antarctica [Ligtenberg et al., 2011]. Ligtenberg et al. [2011] calculates steady-state as well as time-dependent firn density profiles for Antarctica with the same densification expression for both purposes and tuned to optimally fit observations alongside outputs from RACMO2. It includes snowmelt and refreezing processes, where it is known that refrozen meltwater can have higher density and can have significant effect on the density profile of the firn column and the rate of densification associated with it (figure 3.7).

Herron and Langway's [1980] model is the benchmark model for most of the firn densification models developed since 1980. This model was largely based on the Sorge's law coupled with data from the 17 firn cores. Hence, deriving a widely applicable equation for the rate of firn densification ($\frac{d\rho}{dt}$). The model assumes that the change in porosity is related linearly to the changes in stress from the new snow accumulation and the rate of densification has an Arrhenius dependence on temperature. Together, it can be expressed as,

$$\frac{d\rho}{dt} = c(\rho_i - \rho) \tag{3.5}$$

where,

$$c = kexp(\frac{-Q}{RT})b^a \tag{3.6}$$

k and a are constants. Q is the Arrhenius activation energy in $kJmol^{-1}$. R is the gas constant and has a value of 8.314 $kJmol^{-1}K^{-1}$. T is the temperature in Kelvin and b is accumulation rate in meter water equivalent per year ($mw.e.a^{-1}$). c is given by,

$$c = c_0, if \rho \leq 550kgm^{-3}$$

$$c_0 = 11exp(\frac{-10.16}{RT})b^{1.0} \tag{3.7}$$

and

$$c = c_1, if \rho > 550kgm^{-3}$$

$$c_1 = 575exp(\frac{-21.4}{RT})b^{0.5} \tag{3.8}$$

The constants k and a, and the activation energy Q, were all tuned using the firn-core data. Q is lesser than most of the other models, which makes it less sensitive to sub–annual temperature variability. ρ is in grams per cubic centimeter [Stevens et al., 2020].

Li and Zwally [2011; 2015] models are improvements over previous models of Li and Zwally [2002; 2004]. It aims to predict the surface elevation changes associated with the seasonal variability in accumulation and firn compaction rates. Li and Zwally [2011] and Li and Zwally [2015] are respectively tuned to model firn core data from Greenland and Antarctica. Therefore, they share the same basic form as,

$$\frac{d\rho}{dt} = \beta 8.36(273.2 - T_K)^{-2.061} b(\rho_i - \rho) \tag{3.9}$$

T_K refers to the firn temperature which is dependent on time and depth in Kelvin, and b refers to the mean accumulation rate over the lifespan of a firn layer ($mw.e.a^{-1}$). The difference between Li and Zwally [2011] and Li and Zwally [2015] is in the parameter β. For the Antarctic ice sheets,

$$\beta = \beta_1, if \rho \leq 550 kgm^{-3}$$

$$\beta_1 = -1.218–0.403 T_{m,c} \tag{3.10}$$

and

$$\beta = \beta_2, if \rho \leq 550 kgm^{-3}$$

$$\beta_2 = \beta_1(0.792–1.080 b_m + 0.00465 T_{m,c}) \tag{3.11}$$

where $T_{m,c}$ is the mean annual surface temperature in Celsius and b_m is the average accumulation rate for a long period, for the specific site to be modeled.

We use the model developed by Li and Zwally [2015] which is a one-dimensional time dependent formulation of firn densification with the support of heat-transfer equation. This has been forced using a time varying accumulation rate and surface temperature. This is implemented by adapting the community firn model (CFM) developed by Stevens et al. [2020] at University of Washington. As explained earlier, the major inputs to the model are accumulation rate, surface temperature, density of the snow and melt rate.

The CFM underwent several numerical experiments to replicate the results obtained by Li and Zwally [2015] before being used with inputs from RACMO. These are discussed in detail in section 3.3.1.

3.3.1 Numerical experiments

Several standard numerical experiments were carried out with our implementation of the densification model using monthly time steps with varying climate conditions for several locations on the AIS representing a wide range of temperature (T_m) and accumulation rates (A_m). Perturbations in accumulation rate and temperature are used to check for changes in surface height and time taken for the response for climatic conditions like low accumulation–low temperature and high accumulation-high temperature. Perturbations were of the kind where δA(t) = $\pm$0.5 A_m and δT(t) = $\pm$2° C at either shorter periods (few months) or larger periods (few years). One perturbation was applied keeping the other variable constant such as an impulse in accumulation rate by keeping temperature constant or vice versa. Before running the model, it is initialized to steady-state conditions under constant surface temperature (T_m) and accumulation rate (A_m). Two regions are chosen for the experiments which satisfy the necessary conditions; Byrd (70° S 110° W) with A_m = 0.14 $mw.e.a^{-1}$ and T_m = - 28° C and Vostok (77° S 110° E) with A_m = 0.035 $mw.e.a^{-1}$ and T_m = - 56° C. As discussed earlier, two regions with differing climatic conditions will have differing firn profile. This is seen in the density-depth profile from those regions (figure 3.8).

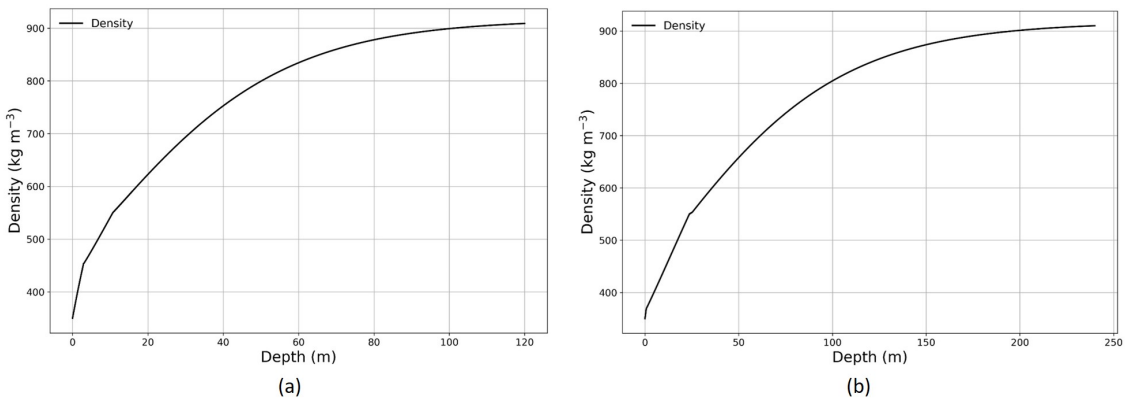

Figure 3.8: Density-depth profile at (a) Byrd and (b) Vostok regions. The abscissa is the depth from the surface (in m), which varies in each subplot. The ordinate shows density (in kgm^{-3}).

The firn-ice transition depth or the depth at which the density of firn is close to that of ice, is largely different at both regions. From figure 3.8, at Byrd the density of firn approaches density of ice at 100 m downwards from the surface whereas at Vostok it is found only at 200 m downwards from the surface which implies z_i[Byrd] = $\sim$ 0.5 z_i[Vostok]. This is found when the mean accumulation rate (A_m) in Byrd is almost 4 times of what is found in Vostok and the mean temperature (T_m) in Byrd is almost half of what is found in Vostok.

In the first experiment, temperature (Tm) is kept constant and a positive impulse in accumulation rate which is 50% of the mean accumulation rate (A_m) is applied for a period of 5 years. This is done at both regions Byrd and Vostok where the initial conditions are different as mentioned earlier and is shown in figure 3.9.

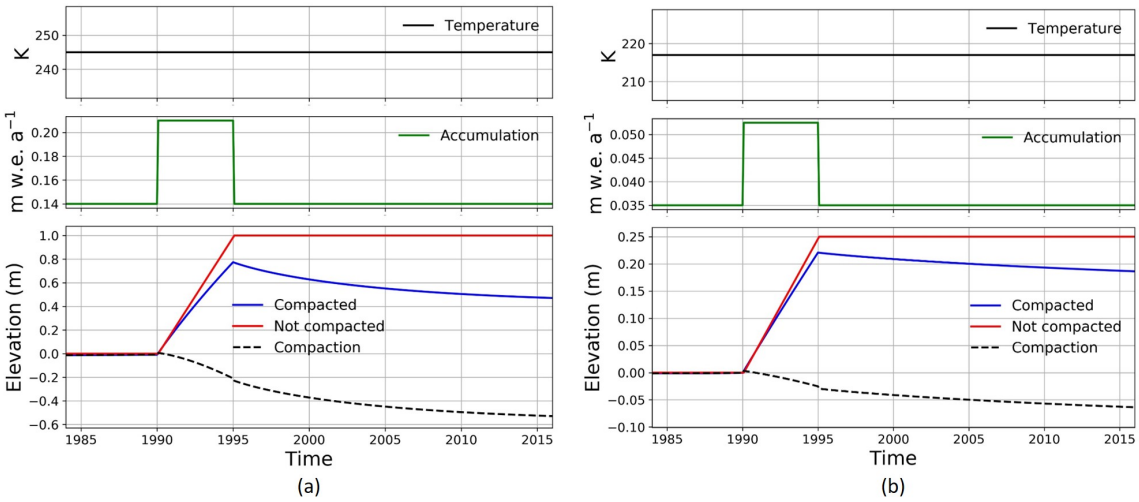

Figure 3.9: Parameter settings and results for the first experiment at (a) Byrd and (b) Vostok. The abscissa is time from 1985 to 2015. The top panel depicts temperature (in K) kept constant. The middle panel depicts accumulation rate (in m w.e. a^{-1}) which has an impulse of + 0.5 times the mean rate during 1990 to 1995. The bottom panel depicts the changes in elevation: compacted signal (in blue) and not compacted (in red) and influence of compaction (in black dash).

At Byrd, accumulation rate becomes 0.21 m w.e. a-1 during 1990-1995 and it is 0.0525 m w.e. a^{-1} at Vostok. Immediately after the onset of the impulse in 1990, at both regions the height starts increasing from the steady state figures kept at 0 m. In the initial phase, the non-compacted and compacted changes are almost the same until a gradual increase in the compaction component induces differences. At Byrd the non-compacted signal reaches the peak 1 m whereas it is only 0.25 m at Vostok due to the differences in the accumulation rate. The compacted signal reaches $\sim$ 0.8 m and $\sim$ 0.22 m at Byrd and Vostok, respectively which is smaller than the non-compacted signal largely due to increasing compaction. In this case, as the accumulation rate is the only varying component, the changes in compaction rate can be considered as compaction only due to variation in rate of accumulation.

In the second experiment, impulse in accumulation rate is applied in both directions: positive and negative successively at the same magnitude (50% of A_m). This implies at Byrd, accumulation rate will be 0.21 m w.e. a^{-1} during 1990-1995 and 0.07 m w.e. a^{-1} during 1995-2000. Similarly, at Vostok, the accumulation rate will be 0.0525 m w.e. a^{-1} and 0.0175 m w.e. a^{-1} during 1990-1995 and 1995-2000

respectively. Results from the experiments are summarized in figure 3.10.

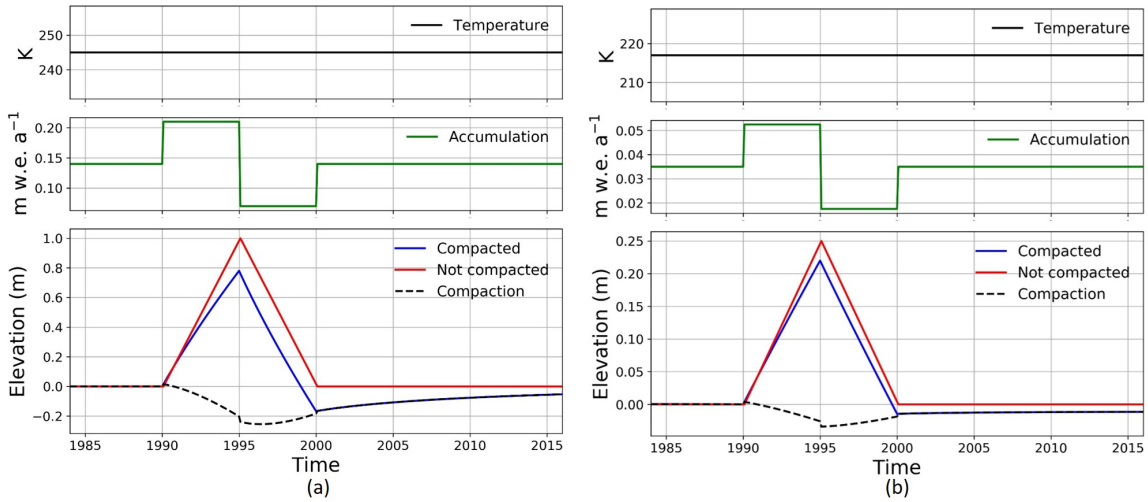

Figure 3.10: Parameter settings and results for the second experiment at (a) Byrd and (b) Vostok. The abscissa is time from 1985 to 2015. The top panel depicts temperature (in K) kept constant. The middle panel depicts accumulation rate (in m w.e. a^{-1}) which has an impulse of 0.5 times the mean rate in both directions (positive during 1990-1995 and negative during 1995-2000). The bottom panel depicts the changes in elevation: compacted signal (in blue) and not compacted (in red) and influence of compaction (in black dash).

Similar to the previous experiment, the height starts increasing from the steady state value kept at 0 m at the occurrence of the impulse in 1990 at both regions. At the onset of the negative impulse in 1995, the compacted height changes decrease at a larger rate compared to the increase which is due to lesser accumulation and compaction to the previous accumulation. The compacted signal gradually recovers towards the previous steady state after the negative impulse since 2000. The rate of recovery varies with the climatic conditions as we see differences between Byrd and Vostok. Similar experiments were carried out at varying climatic conditions with shorter impulse periods which are closer to real world conditions to test for the sensitivity of the model to quick and short term perturbations.

In a third experiment, perturbations in surface temperature is induced on to the model inputs. In this case, the accumulation rate (A_m) is kept constant and surface temperature (T_m) is increased by 2° C for a period of 5 years. This implies for Byrd Am = 0.14 m w.e. a^{-1} and Tm = - 28° C with temperature raised to - 26° C during 1990-1995. Similarly, for Vostok these values are 0.035 m w.e. a^{-1}, - 56° C and - 54° C respectively. Figure 3.11 depicts the inputs and outputs from the experiment.

Contrary to the previous experiments, there is a decrease in surface height at the onset of an increase in temperature. It reaches up to - 0.04 m in Byrd and – 0.006

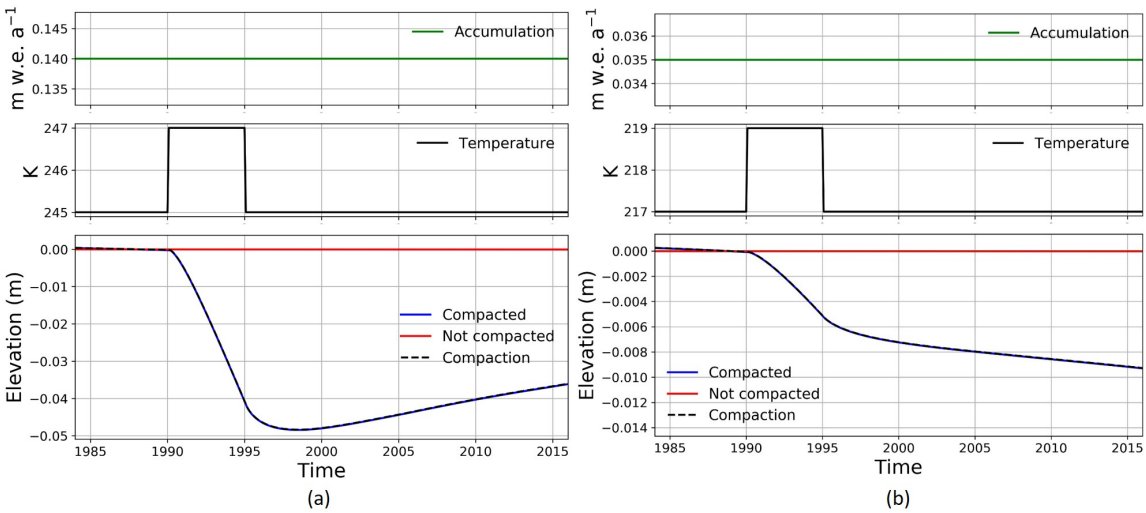

Figure 3.11: Parameter settings and results for the third experiment at (a) Byrd and (b) Vostok. The abscissa is time from 1985 to 2015. The top panel depicts accumulation rate (in m w.e. a^{-1}) kept constant. The middle panel depicts temperature (in K) which has an impulse of 2° C during 1990-1995. The bottom panel depicts the changes in elevation: compacted signal (in blue) and not compacted (in red) and influence of compaction (in black dash).

m in Vostok in 1995 which marks the end of the impulse. After the period of the impulse, the height further reduces at a slower rate for different period of time at Byrd and Vostok before returning to the steady state where the changes in elevation is zero (dH/dt = 0). It can be concluded that a sustained change in temperature (possibly due to climate change) can have nearly linear changes in surface height as there is changes in the mean surface temperature for the firn column [Li & Zwally, 2015].

3.3.2 Height changes from the firn densification model

After several tests and experiments, the model is used to estimate changes in surface height using outputs from RACMO2.3p2. While using the model for this computation, we assume a constant snow density across the AIS at 350 kg m^{-3}. The depth at which firn density is closer to that of the ice varies across the AIS depending on the varying climatic conditions. This depth, which is referred to as critical depth, depends on the climate conditions including rate of accumulation and average temperature. After several tests and experiments on the depth of firn column, a constant firn column depth of 220 m is used inspired from Verjans et al. [2020]. A fresh firn column is modeled at each location in which the density at the top will be that of the snow and at the bottom will be that of the ice. The model is pre-initialized for a period ($\sim$ 100 years) long enough to generate the firn column based upon the currently available climate variables.

Height changes estimated using the FDM at PIG and DML is shown in figure 3.12.

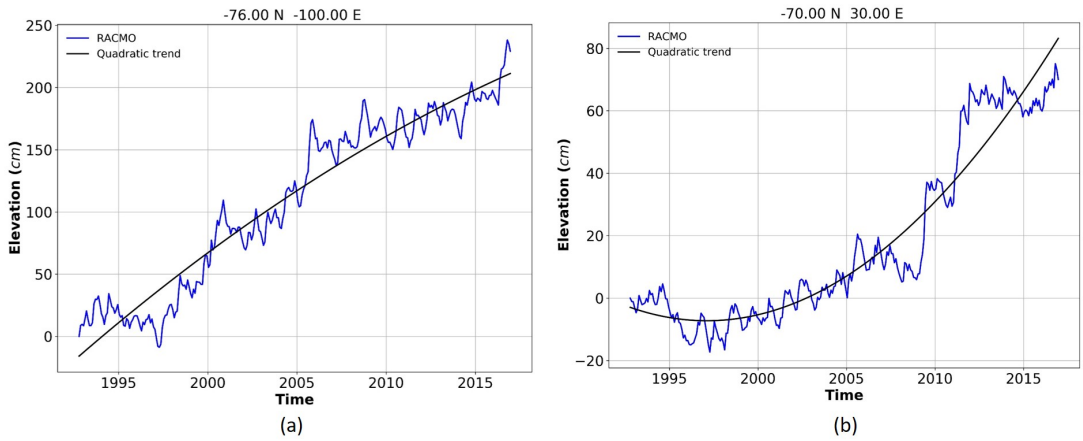

Figure 3.12: Time series of elevation changes in cm at (a) PIG and (b) DML estimated using outputs from RACMO2.3p2 and the firn densification model during 1992–2016. The abscissa is the time. The ordinate shows the variations in elevation (in cm), which varies in each subplot.

At both regions, surface elevation is found to increase even at differing rates. For PIG, this trend is different from estimates from Envisat (figure 2.13), GRACE (figure 2.4) and previous estimates from RACMO (figure 3.3). Differences with Envisat and GRACE measurements are due to the involvement of ice dynamics in the geodetic measurements apart from the SMB. The difference in trends between the current and previous estimates from RACMO is due to the presence of a firn column and addition of the firn densification process while computing the new estimates. A degree-2 polynomial trend (in black) is modeled based on the estimate to compare with Envisat and GRACE derived height changes. Estimates made with the climate model outputs and the firn densification model is further explored comparing the residual changes from these estimates in figure 3.13.

Residual changes in elevation show similar pattern but with differing magnitude as the compacted signal varies between -50 and 50 cm in PIG whereas the non-compacted signal has variations in the range of -20 to 20 cm. Similarly, at DML the compacted signal varies between -20 and 25 cm but the non-compacted signal is limited to -10 and 10 cm. The changes in SMB estimates (in yellow) which is used as an input for estimating the variations in surface height is also shown. The seasonal behavior in the compacted height change signal and is further explored using the monthly means plot (figure 3.14).

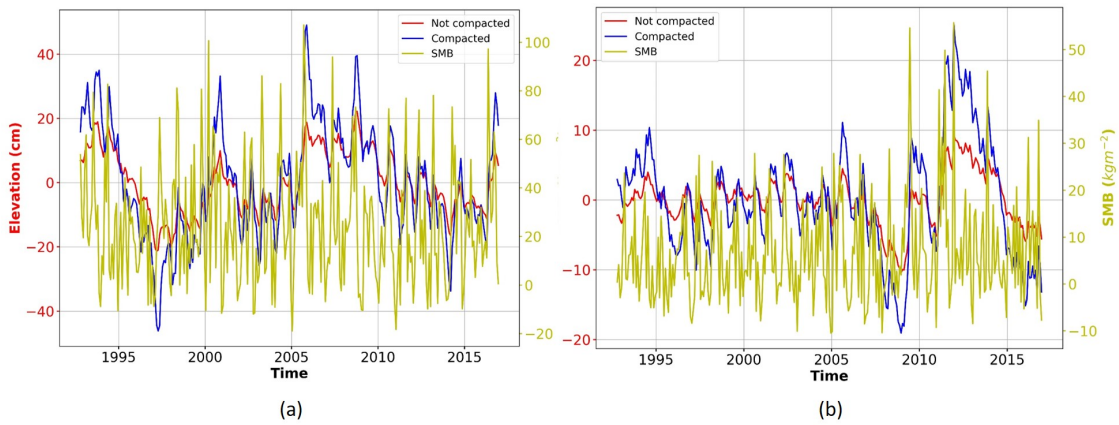

Figure 3.13: Residual changes in elevation both compacted (in blue) and not compacted (in red) and SMB (in yellow) at (a) PIG and (b) DML. The abscissa is the time. The ordinate shows the variations in elevation (in cm) and SMB (in kg m^{-2}), which varies in each subplot.

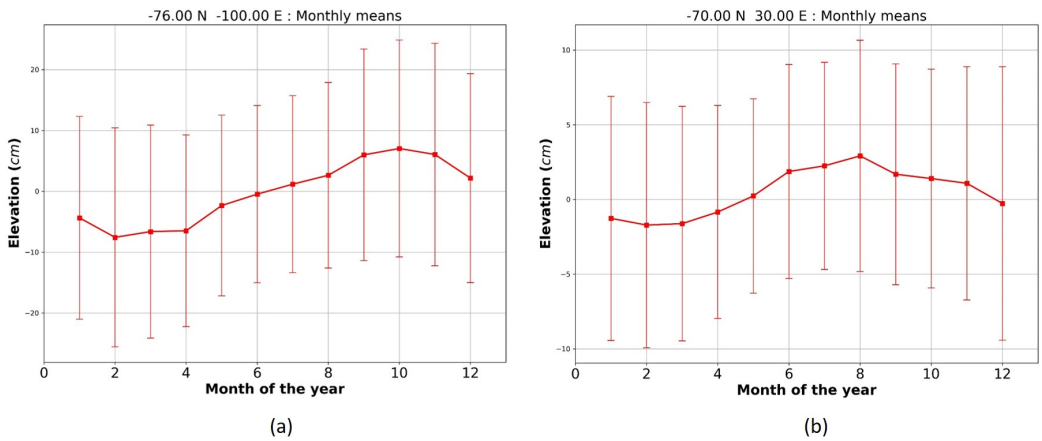

Figure 3.14: Monthly means of residual changes estimated from RACMO outputs and the firn densification model at (a) PIG and (b) DML. Error bars represent standard deviation (1 σ) from the mean. The abscissa is the time representing month of the year. The ordinate shows the changes in elevation (in cm), which varies in each subplot.

Monthly means plot of estimates from RACMO outputs and the firn densification model show similar patterns to that from the non-compacted signal (figure 3.5). Similar to the previous estimates, the signal peaks in October at PIG and it peaks in August at DML. The magnitude is different at both regions as the variations are almost double than compared to the previous estimates. Variations in surface height estimated using RACMO outputs and the firn densification model are put into comparison with estimates from Envisat and GRACE (figure 3.15).

Estimates from the three different techniques agree with each other quiet well at both regions. It indeed shows differing character among these two regions. At

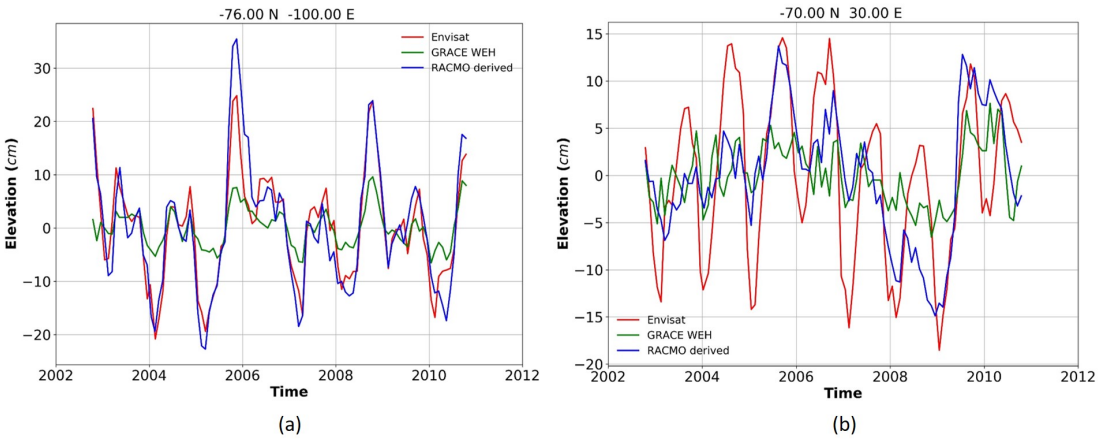

Figure 3.15: Height changes at (a) PIG and (b) DML from Envisat observations (in red), GRACE observations in WEH (in green) and RACMO and firn densification model (in blue). The abscissa is the time. The ordinate shows the variations in elevation (in cm), which varies in each subplot.

PIG, the patterns agree well as it increases and decreases together. The magnitude of changes too is agreeable especially between Envisat and RACMO. Changes from GRACE in WEH over estimates most of the times. At DML too, clear seasonal patterns can be observed in all of the three estimates with those from Envisat being too dominant. At particular periods, good agreement exists in magnitude of changes among these estimates too. Totally, compared to figure 3.6 where non-compacted height change estimates are plotted, the estimates from the firn densification model is much better in shape and magnitude. Larger analysis is carried out among estimates in section 4.1.

Standard deviation maps of residual changes give a larger picture of changes for the whole ice sheet for multiple time periods (figure 3.16). Magnitude of changes are lesser during 2002 – 2010 i.e., 0 to 12 cm in elevation (figure 3.16 a) in comparison with 2002 – 2016 i.e., 0 to 14 cm in elevation (figure 3.16 b) and with 1992 – 2016 i.e. 0 to 16 cm in elevation (figure 3.16 c). Similar to previous estimates, most of the changes happen in West Antarctica and in Antarctic Peninsula region. Very minimal changes are found in the interior regions of the AIS at all periods and changes are majorly focused along the regions in proximity to the coast and ocean.

Standard deviation maps from multiple estimates during the common period (2002-2010) are used to make an initial comparison between them (figure 3.17).

Maximum of the standard deviation of changes from each technique fall in the range of 10 to 12 cm. Changes are majorly found along the coast in each of these method. Estimates of changes from Envisat and RACMO are lesser and comparable with each other in comparison with those from GRACE in the interiors of the

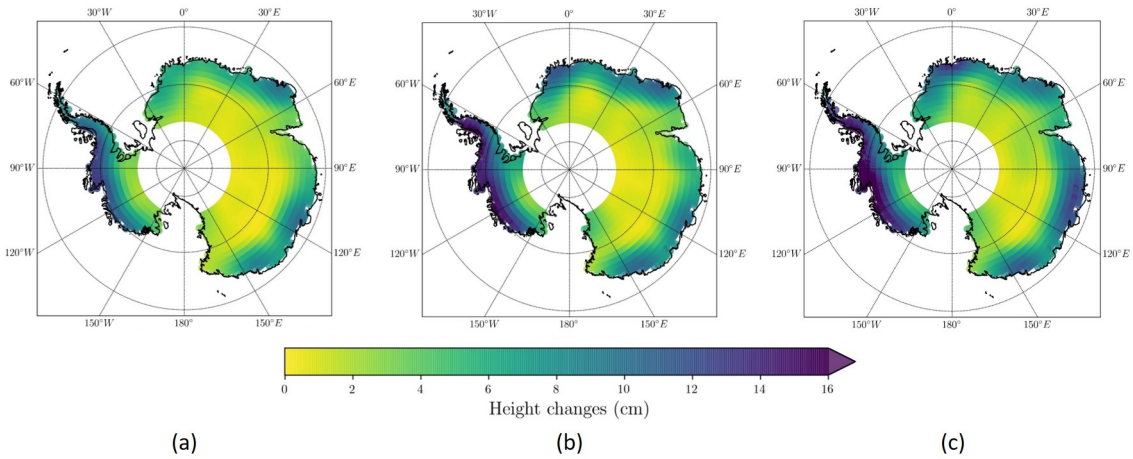

Figure 3.16: Standard deviation of temporal changes (in cm) computed from RACMO outputs during (a) 2002–2010 (Envisat period), (b) 2002–2016 (GRACE period) and (c) 1992–2017. Varies between 0 cm (in yellow) to 16 cm (in violet).

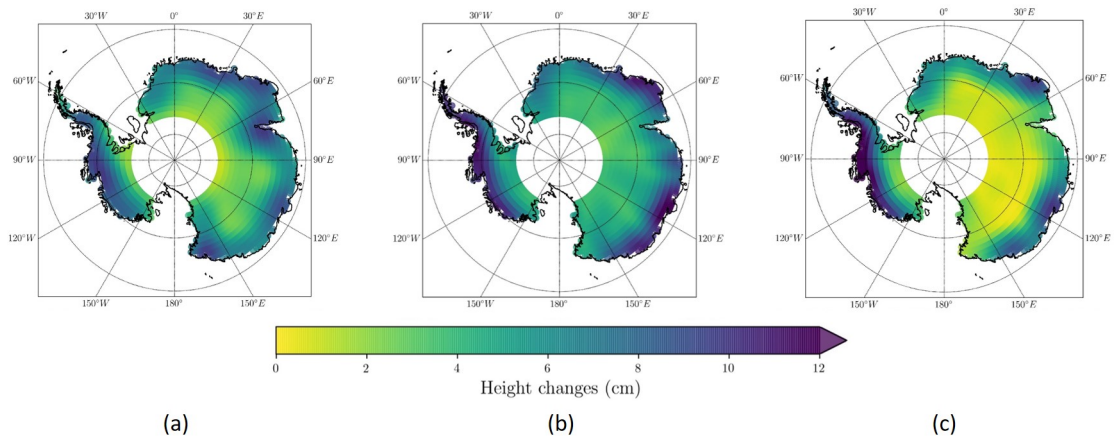

Figure 3.17: Standard deviation of temporal changes (in cm) observed using (a) Envisat, (b) GRACE in SEH and (c) RACMO for the period 2002-2010. Varies between 0 cm (in yellow) to 12 cm (in violet).

AIS. This is majorly due to low SMB values in the interiors due to negligibly low accumulation rates and extreme climatic conditions as estimates from RACMO is largely based on variations in accumulation rate and surface temperature. Other variations exist between standard deviation maps from differing estimates such as higher values in the region between 60° E and 90° E (close to Mac. Robertson Land) in Envisat estimates comparison with other two estimates.

In the next chapter, we make much detailed comparisons among estimates scientifically trying to corroborate the reasons in the context of the AIS. Another aim is to investigate the height change patterns for the inter-annual variability discussed in section 1.2.5.

Chapter 4

Inter-annual variability

Inter-annual variability in AIS remains poorly addressed as discussed in section 1.2.5. These variability needs to be properly understood including its origin or causes, magnitude of influence, frequency of occurrence, etc. By using three distinct estimates of changes in the AIS (altimetry, gravimetry and climate models), we try to explain the poorly known and understood inter annual variability.

4.1 Comparison between height changes

The estimates of changes in AIS are from three distinct sources with differing techniques. Comparing each of these estimates with one another is of paramount importance to improve our understanding of mass changes over the AIS. It is achieved by carrying out a correlation analysis followed by a regression analysis among these estimates.

4.1.1 Correlation analysis

At each region, coefficient of correlation is computed between height change estimates from a pair of two distinct techniques for a common period. In this case, correlation coefficient for height change estimates from Envisat and GRACE (figure 4.1 a), Envisat and RACMO (figure 4.1 b) and GRACE and RACMO (figure 4.1 c) during the period 2002–2010 is computed. The coefficient values ranges between -1 and 1. In an ideal case, the coefficient of correlation between two independent time series is close to 1. A positive coefficient indicates that both estimates of height changes increase or decrease together and vice versa. A value of 0 indicate a lack of any relation between the two estimates. It does not give much insights about the magnitude of changes among two distinct estimation techniques.

High positive correlation is observed between each of the estimates in West

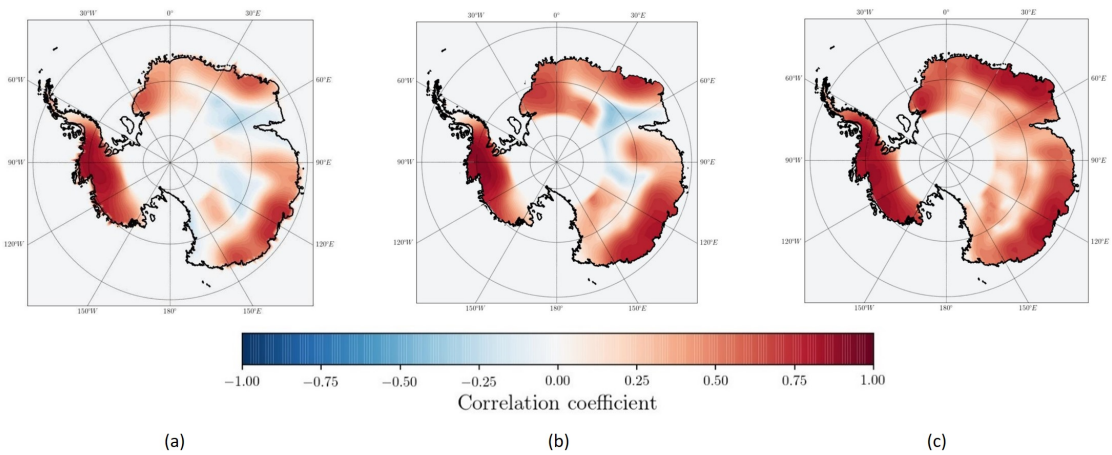

Figure 4.1: Coefficient of correlation between height changes estimated from (a) Envisat and GRACE, (b) Envisat and RACMO and (c) GRACE and RACMO, during the period 2002 - 2010. Positive and negative correlation coefficients are in red and blue respectively.

Antarctica and coastal regions of East Antarctica. Estimates from GRACE and RACMO are found to have maximum regions with positive correlation coefficient with high values at all longitudes except in the interiors (figure 4.1 c). At PIG, the coefficients of correlation between estimates from Envisat and GRACE, Envisat and RACMO and GRACE and RACMO is 0.61, 0.90 and 0.74 respectively. Similarly, at DML the correlation coefficient values are 0.35, 0.56 and 0.70. Regions between 30° E and 120° E seems to have regions with negative or zero correlation in height change estimate pairs of Envisat with both GRACE and RACMO (figure 4.1 a & b). This anomaly can be likely attributed to the presence of strong katabatic winds in that region and sensitivity of Envisat observations to this phenomenon. In these regions, estimates from Envisat will be either out of phase or completely different from estimates from both GRACE and RACMO. To further understand the relation between the estimates from differing techniques a regression analysis is employed.

4.1.2 Regression analysis

Similar to the correlation analysis, regression analysis is carried out among the different height change estimates for the period 2002–2010. At each region, a coefficient of linear regression and the corresponding uncertainty is computed between height change estimates from a pair of two distinct techniques. This coefficient reflects how well time and amplitude variations of a time series are similar to that estimated from another observation. The coefficient of linear regression, C between two data sets D_1 and D_2 is given by:

$$C[i,j] = \frac{\left[C_{12}[i,j] + \frac{1}{C_{21}[i,j]}\right]}{2} \tag{4.1}$$

where C_{12} and C_{21} represent the coefficient of regression for D_1 with respect to D_2, and vice versa, respectively. i and j stand for the latitude and longitude of the region, respectively. Uncertainty associated, U is expressed as:

$$U[i,j] = U_{12}[i,j] + \frac{U_{21}[i,j]}{C_{12}[i,j] * C_{21}[i,j]} \tag{4.2}$$

where U_{12} and U_{21} represent the uncertainty obtained while calculating C_{12} and C_{21}, respectively. These coefficients of linear regression and their corresponding uncertainties are mapped in figure 4.2 (a – f).

In an ideal case, the coefficient of regression is close to 1 and the corresponding uncertainty is close to 0. A positive coefficient indicates that both estimates of height change increase or decrease together, whereas having a negative coefficient implies the other way around. Along with that, the magnitude of the coefficient characterizes the relation between the amplitude of the signal. A coefficient closer to 1 indicates that height estimates from the two techniques are identical in phase and amplitude.

Height changes estimated from GRACE in SEH and those derived from RACMO are close to the ideal scenario largely across the AIS (figure 4.2 c & f). This along with maps of regression coefficient between Envisat and GRACE in SEH indicate changes are largely due to changes in snow height. The regression coefficient would have been far from ideal if GRACE estimates are taken as IEH or WEH. Similar to the correlation coefficient maps between estimates from Envisat with both GRACE and RACMO (figure 4.2 a & b), regions with negative regression coefficient and larger uncertainty values can be observed between 30° E and 120° E and sometimes extending up to 150° E (figure 4.2 a & d, b & c). This further explains the sensitive nature of Envisat observations towards katabatic winds present in the interiors of East Antarctica.

Apart from PIG and DML, we chose two more locations having near ideal conditions while performing correlation and regression analysis; Coats Land (CL) around 80° S 28° W and Wilkes Land (WL) around 70° S and 120° W. Table 4.1 lists coefficient of regression and corresponding uncertainty between multiple height change estimates during 2002-2010.

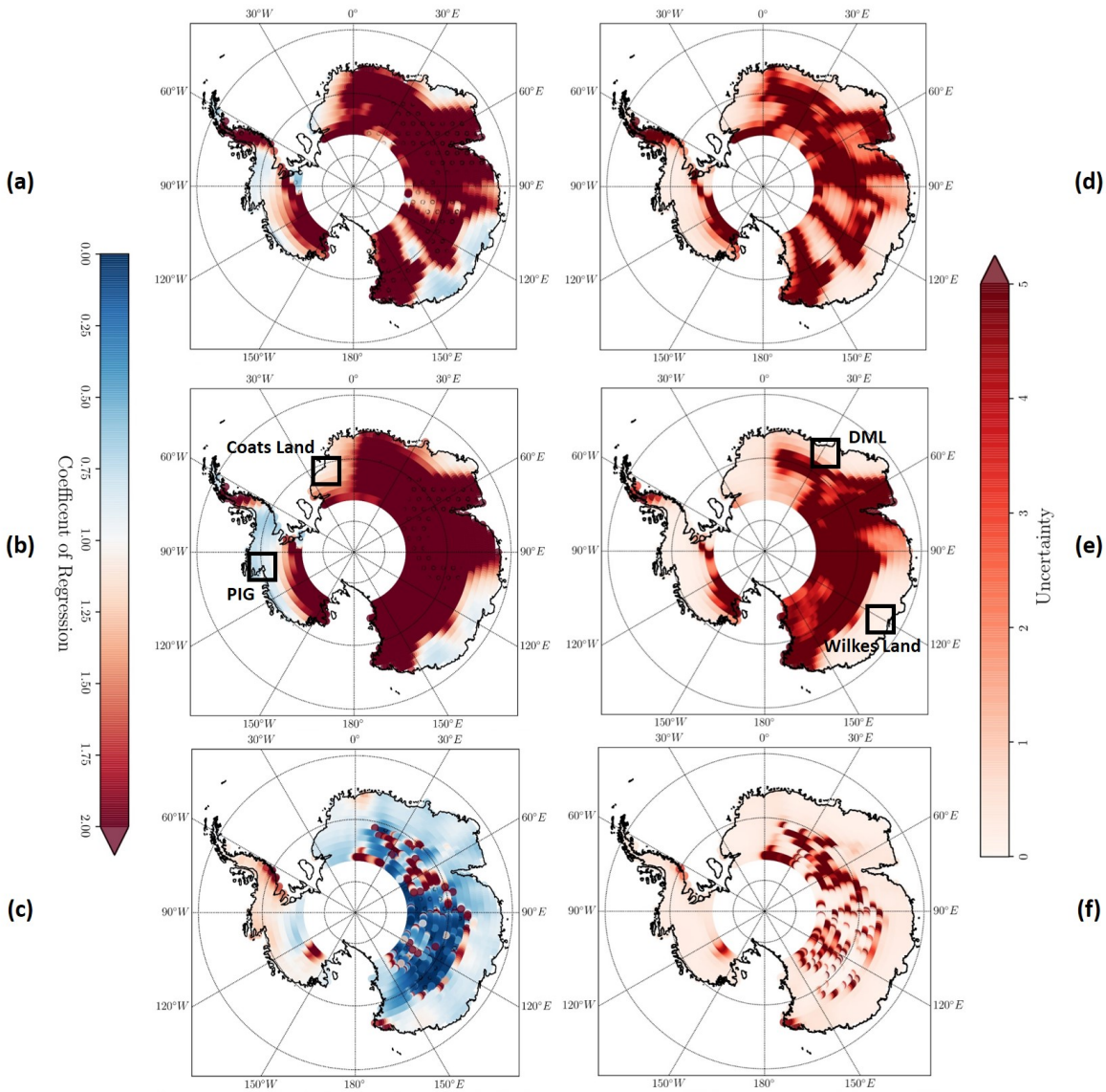

Figure 4.2: Coefficient of regression (left) and uncertainty (right) maps between height changes estimated from (a, d) Envisat and GRACE in SEH, (b, e) Envisat and RACMO, and (c, f) GRACE in SEH and RACMO, during the period 2002–2010. In the coefficient of regression maps, color indicates the magnitude, and the dark circle refer to regions where the coefficient is negative. Larger uncertainty values are indicated using dark red.

Table 4.1: Regression coefficients between height changes computed using our three data sets at four different locations with respective coordinates in square brackets. Values in the bracket denotes uncertainty.

Site	**Envisat & GRACE**	**Envisat & RACMO**	**GRACE & RACMO**
PIG	1.08 (0.29)	0.87 (0.08)	1.16 (0.24)
CL	1.39 (0.92)	1.66 (0.80)	0.74 (0.20)
DML	1.57 (0.84)	1.56 (0.48)	0.81 (0.16)
WL	0.96 (0.36)	1.04 (0.02)	0.86 (0.24)

The time series of height changes from theabove mentioned locations is shown in figure 4.3 (a-d). Estimates from Envisat (in blue) are during 2002-2010 whereas those from GRACE and RACMO are during 2002-2016.

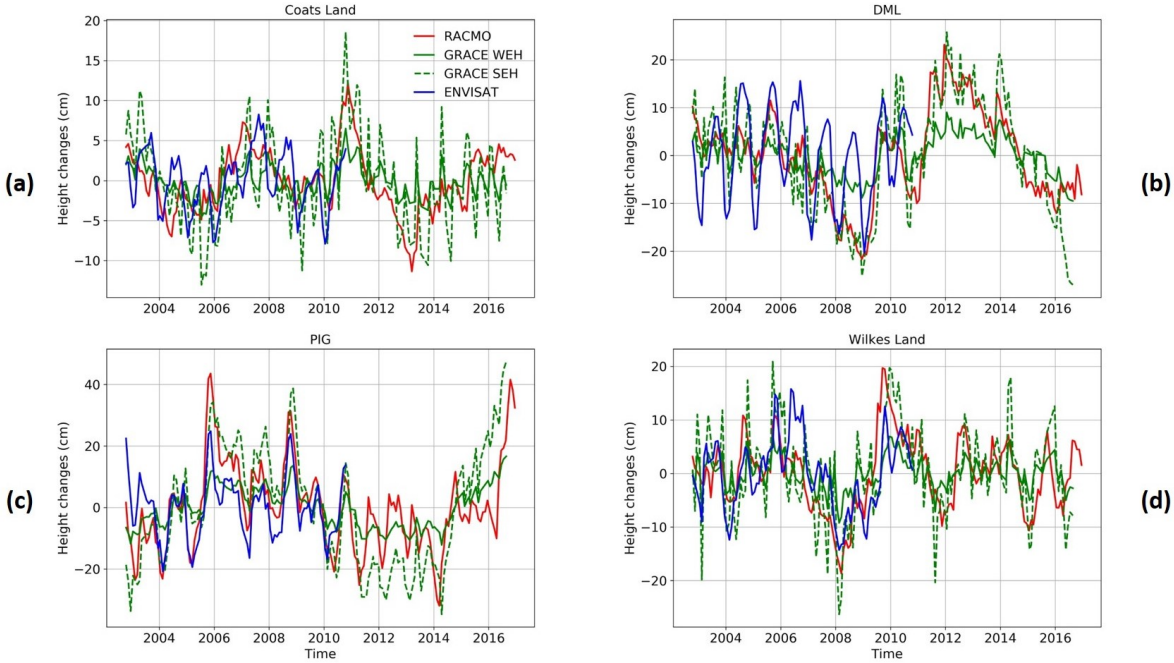

Figure 4.3: Height changes are shown for CL (a), DML (b), PIG (c), and WL (d) with that computed from RACMO in red, GRACE solutions in green, separating WEH (solid) from SEH (dash), and Envisat observations in blue. The abscissa is the time. The ordinate shows the amplitude (in cm), which varies in each subplot.

Observations from PIG and DML were already discussed for the common period in the previous chapter (figure 3.15). At each region, SEH estimate from GRACE has comparable magnitude with estimates from Envisat and RACMO rather than the WEH estimate. Estimates from Envisat show strong seasonal behavior irrespective of the location or the region. Varying nature of the magnitude of variations among different regions are also found in these time series similar to figure 3.15. Good agreement exists between estimates from GRACE and RACMO after the Envisat period (2002-2010) at all regions depicted here. Peaks and troughs with more than one year gaps are too found at several regions at different time periods. Peaks can be found at PIG in early 2006, mid-2008 and mid-2016 and similarly at other regions. Now we move towards exploring inter annual variability in the AIS using various height change estimates.

4.2 Extraction of inter annual signals

Several methods have been adopted to extract the inter annual signal around Antarctica. For example, Cerrone et al. [2017] used a band-pass filter applied on climate parameters above the Southern Ocean (SO). On the other hand, Autret et al. [2013] used an empirical mode decomposition (EMD) to analyze the automatic weather station data at coast. Here, we first apply the EMD to all of our time series covering the AIS as it is found superior to other techniques to analyze signals for the studied period.

Empirical mode decomposition

The empirical mode decomposition (EMD) perform self-adaptive decomposition of the signal on the basis of nonlinear functions extracted from the signal itself [Huang et al., 1971]. EMD decomposes the signal into intrinsic modes which correspond to physical characteristics of the studied signal using a sifting process. This sifting process consists of defining a local phenomenon or feature considering the oscillations of the signal between a maxima and a minima. This procedure is applied iteratively on the original signal to extract constituent modes and their trends.

The EMD applied to height changes in Antarctica during the period 2002–2010 commonly yields 4 to 6 modes. The largest group, representing 65% of our time series, has 5 modes. Time series resulting in 4 and 6 modes represent 33% and 2%, respectively. An example of the EMD applied to height changes is given in figure 4.4

For a time series with 5 modes, the first mode represents the quasi-monthly disturbances which is largely referred to as noise. Seasonal cycles and signals with periodicity less than or up to one year constitute the second mode. The third mode has periodicity values greater than 1 year. A quasi-4-year cycle dominates the fourth mode. Higher modes constitute components with longer periods [Autret et al., 2013]. To extract the inter-annual changes, we reconstruct the time series by combining modes which are independent of high frequency changes, seasonal changes and very long-term trends. Therefore, we combine modes 3 and 4 and modes 4 and 5 to reconstruct the inter-annual changes at locations where we have 5 and 6 modes, respectively. We only use the mode 3 where only 4 modes are obtained after the EMD.

At each location, we extract the inter-annual signal which is the height change estimates independent of noise, seasonal signal, and very long-term trends. The extracted inter annual signal for CL, DML, PIG and WL is shown in figure 4.5.

At every selected region, the inter-annual height changes from the three tech-

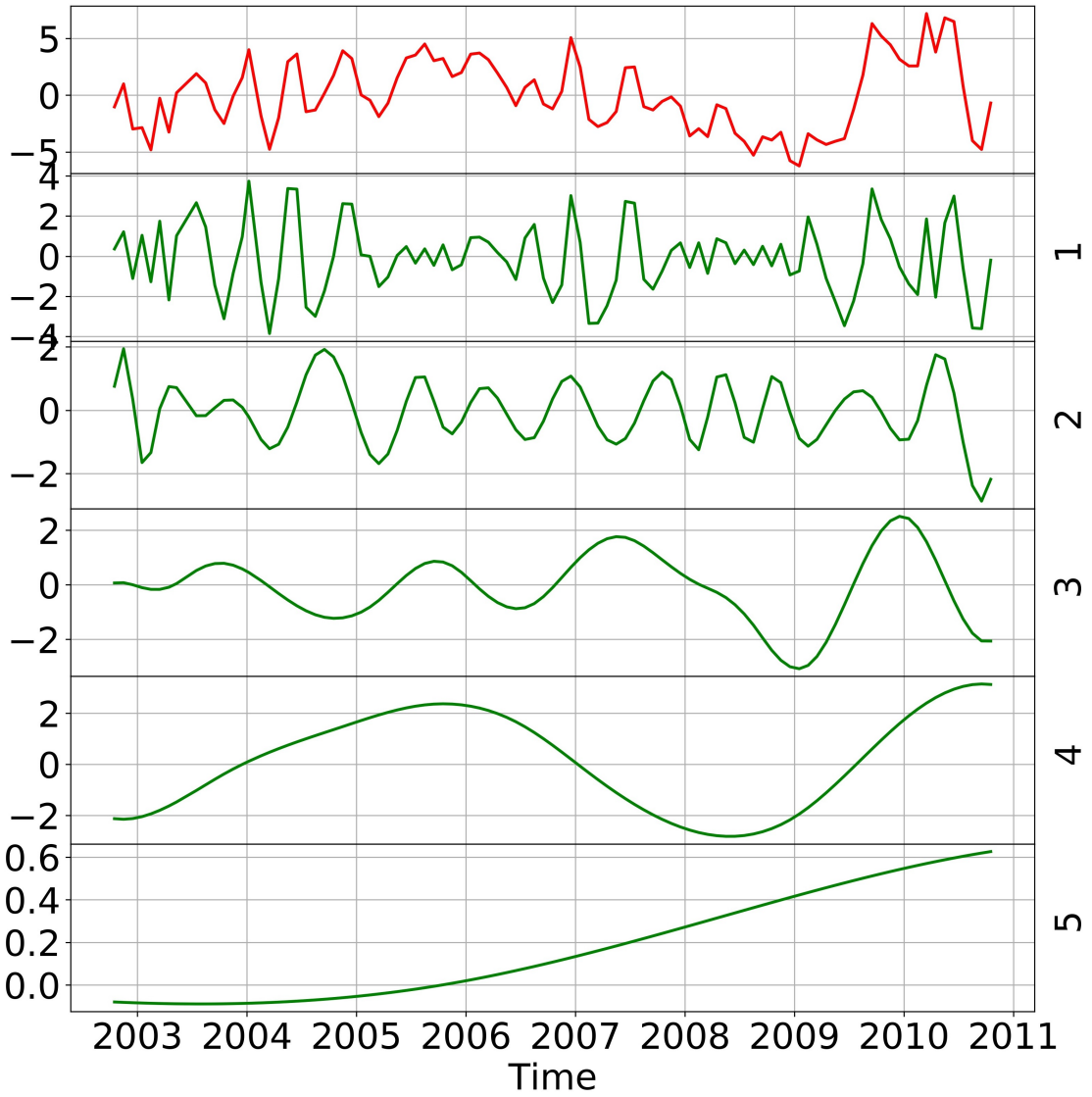

Figure 4.4: An example of EMD applied to height changes at DML. SEH from GRACE normalized to standard deviation at DML in red and constituent modes in green. The abscissa is the time. The ordinate shows the amplitude of the signal (in left) and the corresponding mode (in right).

niques exhibit comparable properties which include period and amplitude. The mean and maximum coefficient of correlation is 63 and 86%, 72 and 91%, and 65 and 91% between inter annual height changes derived from Envisat and GRACE, Envisat and RACMO, GRACE and RACMO, respectively (table 4.2).

Table 4.2: Correlation coefficients between inter-annual height changes derived using EMD analysis.

Site	**Envisat & GRACE**	**Envisat & RACMO**	**GRACE & RACMO**
PIG	0.26	0.91	0.28

CL	0.86	0.43	0.67
DML	0.71	0.70	0.91
WL	0.67	0.82	0.73

The inter-annual signal has higher magnitude variations in PIG, DML, and WL, where it has an amplitude of ∼10 cm. In CL, the amplitude of the inter-annual signal falls to ∼5 cm. This difference is likely due to the location of the regions. Indeed, PIG, WL, DML are coastal regions with no permanent ice shelf, whereas CL is close to the permanent Ronne Filchner ice shelf, thus being likely less subject to ocean influences. Apart from the amplitude, similarities and differences can be derived in terms of periodic content. Indeed, the inter-annual signal in CL, DML, and WL shows longer periods than that at PIG. It is further investigated for the whole AIS in section 4.3.

The information retained in the extracted signal (% IA) is given as,

$$\%IA[i,j] = \left[\frac{RMS(S[i,j]}{RMS(O[i,j])}\right] * 100 \tag{4.3}$$

where S and O represent the extracted inter-annual signal and monthly height changes respectively. i and j stand for the latitude and longitude of the region respectively. Maps of % IA for inter annual-signal from each technique is shown in figure 4.6.

The percent of energy retained by the inter annual signal is above average at all cases (figure 4.6 a, b, c). Maximum retention is found in inter annual signal extracted from height change estimates from RACMO (figure 4.6 c). Larger the value implies larger is the share of inter-annual signal in the original height change signal. Larger values are found majorly along the coasts irrespective of the technique used to estimate height changes.

Next, to characterize the inter-annual changes over the whole of the AIS, we use the reconstructed height changes from the EMD.

4.3 Characterizing inter-annual signals

Inter-annual signal obtained by reconstruction of modes after EMD holds the key for inter-annual variability. It needs to be characterized to scientifically understand the properties of the extracted inter annual signal. We use the least squares method to identify the period that represents the inter-annual signal the best.

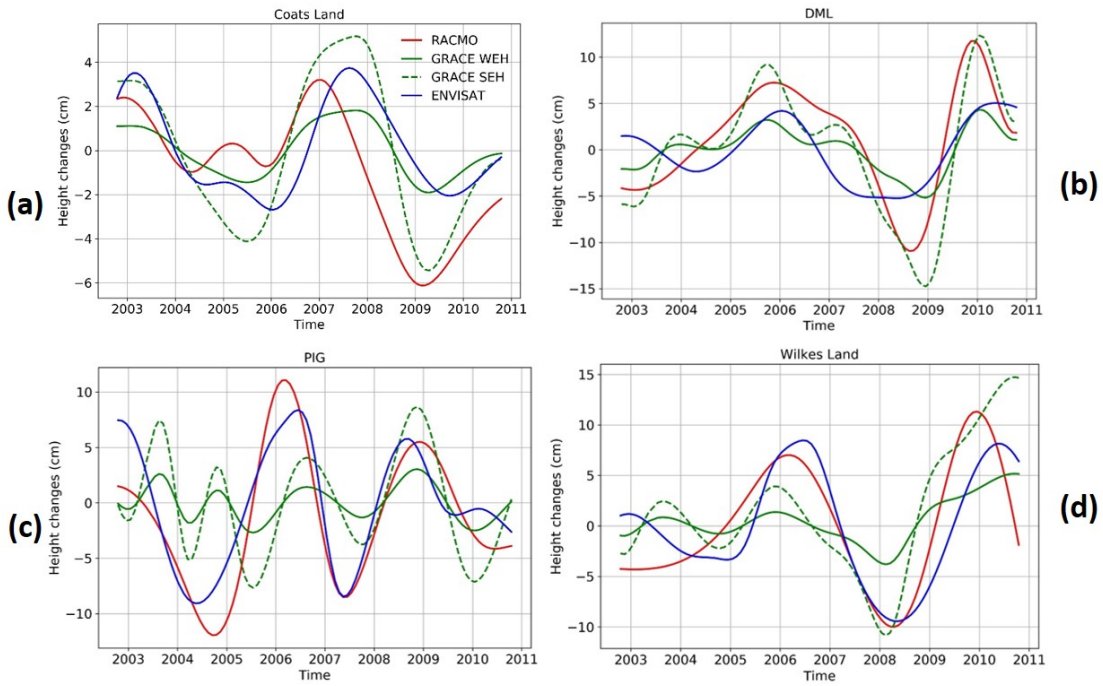

Figure 4.5: Inter-annual height changes after mode reconstruction following the EMD analysis at CL (a), DML (b), PIG (c), WL (d). Height change estimates are from RACMO (red), GRACE in WEH (green), SEH (dashed green) and Envisat (blue). The abscissa is the time. The ordinate shows the amplitude of the signal (in cm), which varies in each subplot.

4.3.1 Least squares method

In this method, the purpose is to find a single period among a range of periods (in this case 2 years to 8 years), that best fits the inter annual signal. Best fit is considered when the difference between the RMS of the inter annual signal and that of the single period fit is the lowest. If S represents our derived inter annual changes, and F_T represents the periodic fit with a period of T, then:

$$\Delta RMS[i,j] = RMS(S[i,j]) - RMS(F_T[i,j]) \tag{4.4}$$

i and j are latitude and longitude of the region respectively. Period T, is chosen for which the ΔRMS is the lowest for all set of values in T. To assess the fitting process across the AIS, RMS reduction % R (in %) is computed for the single period fit from the inter annual signal (figure 4.7). It is expressed as;

$$\%R[i,j] = \left[1 - \frac{\Delta RMS[i,j]}{RMS(S[i,j])}\right] * 100 \tag{4.5}$$

where ΔRMS is the difference between the RMS of inter annual signal and best fitting single period model. In an ideal case, ΔRMS will be 0 and % R will be 100%. Therefore, % R tends to 100% if the model fits perfectly, and 0% otherwise.

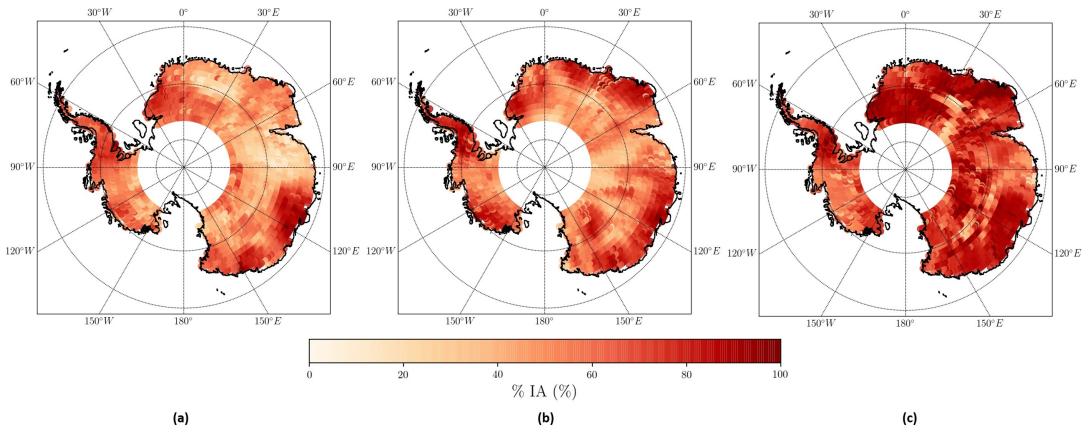

Figure 4.6: Energy ratio of the inter-annual signal extracted from (a) Envisat, (b) GRACE and (c) RACMO. Higher values (in dark red) indicate higher energy contention in the inter-annual signal and lower values (in white) indicate negligible less energy retention.

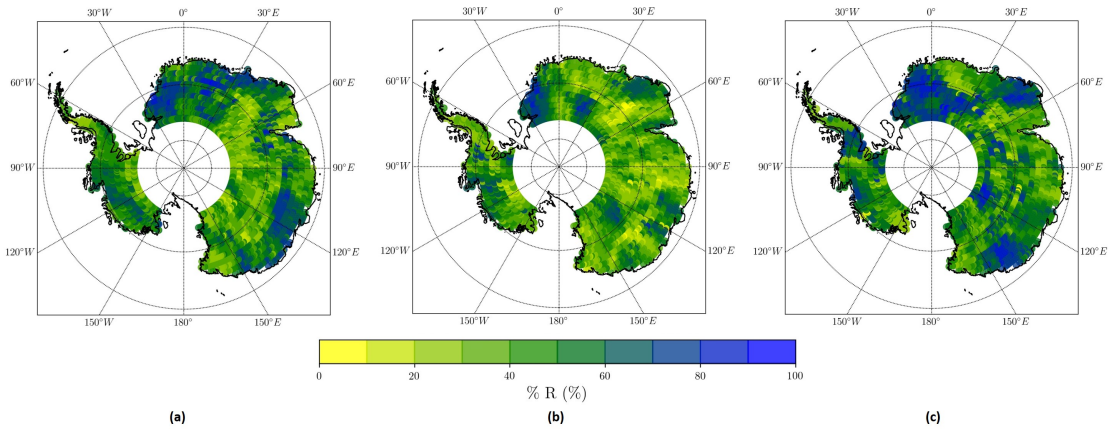

Figure 4.7: RMS reduction (in %) of the best single period fitting model for height changes estimated from Envisat (a), GRACE (b), and RACMO (c). Value ranges between the least value 0% (yellow) and the highest value 100% (blue).

Regions with the largest RMS reduction are very similar whatever the method used to quantify the changes of the ice sheet be (Envisat, GRACE and RACMO). These regions are that of PIG, CL, WL, Enderby Land (EL, between 30 and 60° E), and Terre Adélie (TA, west of 150° E). There, the RMS reduction is larger than 50%. It can reach up to 80% in CL and TA. GRACE derived height changes lead to the lowest RMS reduction, while that from RACMO are the largest.

4.3.2 Periodicity

The frequency of occurrence of the inter annual component is an important metric while investigating inter-annual variability as it translates into effects of specific cli-

mate processes. Therefore, the period associated with the inter annual signal or the best fitting single period model of the inter annual signal is a key characteristic to derive. For each technique and at every region for the whole AIS, period of the best fitting model represents the periodic behavior of the inter annual signal. Maps of periodicity of the inter annual signal for the AIS is shown in figure 4.8.

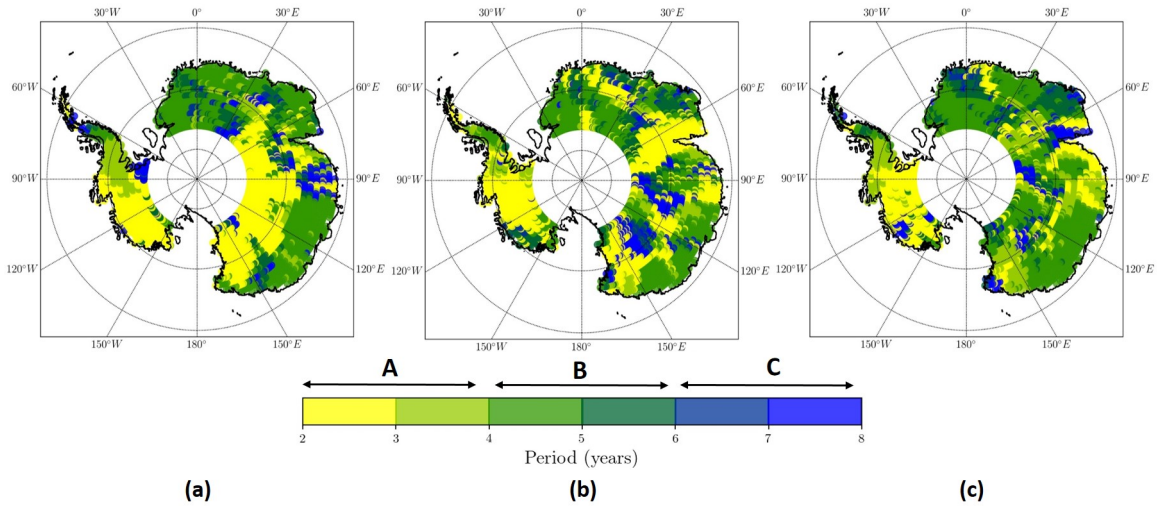

Figure 4.8: Maps of the period of the best fitting model for height changes estimated from Envisat (a), GRACE in SEH (b), and RACMO (c) after EMD. Value ranges between the lowest value 2 years (in yellow) and the highest value 8 years (in blue). The period range is broken down into three classes: A, B, and C.

The period values range between 2 and 8 years. Regions within latitudes North of 75° S and between 30° W and 165° E (see the period of inter-annual signal in Figure 4.5 a,b,d), barring few exceptional regions, like that of Mac Robertson Land, have period values between 4 and 6 years. West Antarctica (see the period of inter-annual signal in Figure 4.8 c) and the Antarctic Peninsula have period values between 2 and 4 years. Only few regions in the whole AIS have period values in the range 6 to 8 years. The distribution of period values can be understood with the help of histogram plots for each maps (figure 4.9).

Two peaks can be identified in three of the histograms; between 2 and 4 years and between 4 and 6 years (figure 4.9). Based on the maps and histogram plots, the period values can be grouped into three classes; class A, class B and class C. Class A has periods less than 4 years whereas class C has periods greater than 6 years. Hence class B is the set of periods between 4 and 6 years. The count of regions falling in each class can be understood from the histograms. But every region does not have the same area as the earth is spherical in shape. Area wise coverage in the AIS by each class is given in the table 4.3.

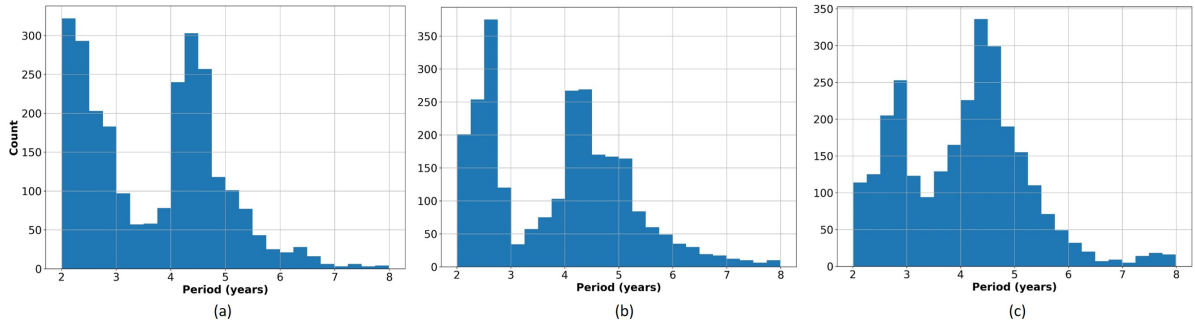

Figure 4.9: Histogram of period values extracted from inter-annual signals from Envisat (a), GRACE (b) and RACMO (c). The abscissa is the period (years). The ordinate shows the count of each period.

Table 4.3: Percentage of area covered by each class from each data set.

	Class A (<4 Years)	**Class B (4–6 Years)**	**Class C (>6 Years)**
Envisat	45.25	44.32	10.42
GRACE	46.57	45.18	8.25
RACMO	39.82	52.13	8.04

The class that covers the largest area is class B, representing 44 to 52% of the total studied area. Class A has a total coverage ranging between 40 and 47% of the investigated regions. The final class, and the smallest class by area covered, class C, is found at exceptional regions indicating no clear spatial patterns and covers only 8 to 10% area.

4.3.3 Amplitude

Amplitude is another key parameter from the inter annual signal alongside the periodic nature (figure 4.5). It is extracted as the amplitude of the best fitting periodic model found during the least squares estimate. Amplitude thus extracted for the whole AIS from the differing techniques is shown in figure 4.10.

Amplitude maps show quasi-identical patterns across estimates derived from Envisat, GRACE, and RACMO. The inter-annual signal is the strongest along the coast of the Antarctic Pacific sector and in EL and WL, even though the estimates seem to vary in magnitude depending on the data sets. Comparing amplitude maps of GRACE in SEH and WEH, SEH amplitude map is found comparable in magnitude with that from RACMO and Envisat rather than WEH. It supports the idea that the inter-annual changes are majorly driven by changes in density closer to that of snow. It is also worth noting that the inter annual signals are greater than an average magnitude along the coasts of the AIS, except in regions between 60° E and

110° E where it seems to have very less magnitude. The area where the inter-annual signal has significant influence and strength falls within a buffer of ∼600 km or 5° from the AIS coastline. This buffer region shows common periods across different data sets. To explore the inter-annual signal in this region and extract common modes of variability from our three data sets, we perform locally a PCA (Principal Component Analysis) on the height changes.

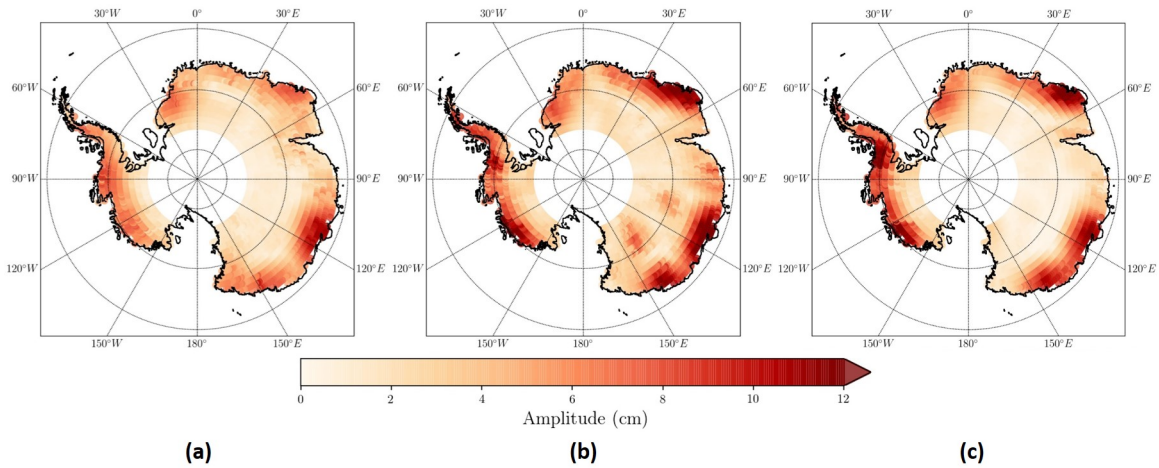

Figure 4.10: Maps of the amplitude of the best fitting model for height changes estimated from Envisat (a), GRACE in SEH (b), and RACMO (c) after EMD. Value ranges between 0 (in white) and 12 cm (in red).

4.4 Principal component analysis

PCA on a multivariate time series is a statistical technique with linear combinations of these variables for deriving the variance-covariance matrix of a set of m—dimensional variables [Wei, 2018]. A large m—dimensional data can be sufficiently expressed by k principal components, where k < m and, hence, a reduction of the number of degrees of freedom of the problem. PCA on a set of correlated variables converts it into a set of uncorrelated variables through an orthogonal transformation. This technique can be used on general variables or standardized variables and hence either the covariance matrix or correlation matrix is used. The goal of the method is to represent a large m—dimensional process with much smaller k principal components that would explain a large part of the variance of the data.

Regions are selected along the coast of the AIS and within the buffer region discussed in the previous section at equal intervals of 15° longitudinally to perform a PCA locally on the inter annual height changes (figure 4.11).

PCA is performed locally on three independent time series normalized to their standard deviation and obtained three principal components (PCs): PC1, PC2,

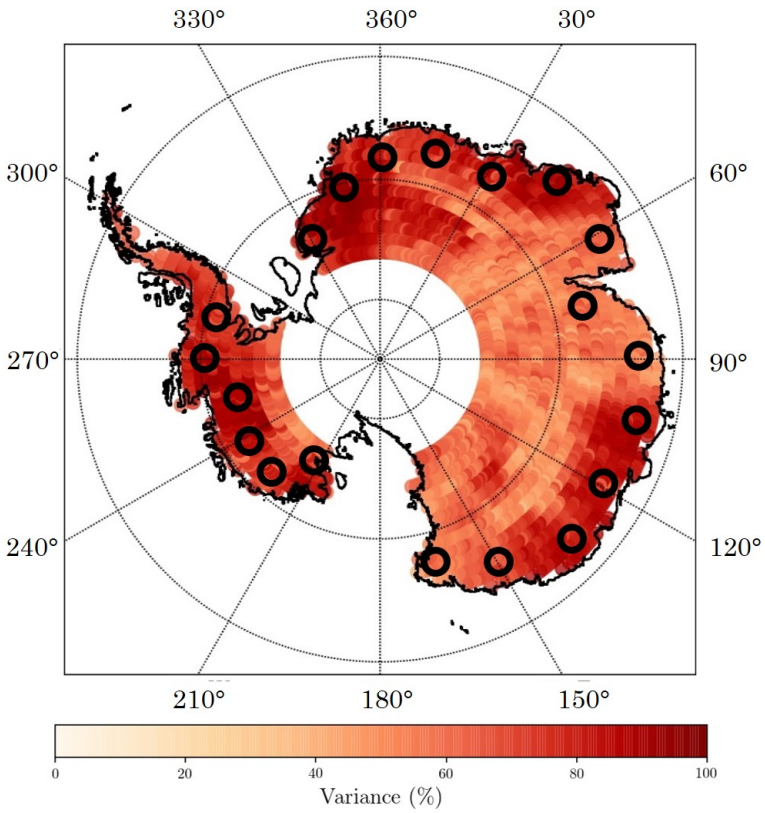

Figure 4.11: Explained variance map of the PC1 with locations (black circles) of sites selected to perform the PCA. Darker color indicates larger explained variance.

and PC3. The first principal component, PC1 has a mean variance of 76% and a standard deviation of 11% (table 4.4). Means of the variance of the second and third principal components (PC2 and PC3) are, respectively, 17% and 6%.

Table 4.4: Explained variance in percentage after Principal Component Analysis (PCA) at the 20 regions.

Longitude[°]	**First Principal Component (PC1)**	**Second PC (PC2)**	**Third PC (PC3)**
15	73.20	20.83	5.96
30	80.99	14.16	4.85
45	81.93	12.72	5.35
60	71.86	21.38	6.76
75	68.97	17.85	13.18
90	46.29	33.26	20.45
105	84.97	9.54	5.48
120	82.76	11.42	5.81
135	84.11	9.40	6.49
150	72.91	22.24	4.85

165	57.86	32.08	10.06
-	-	-	-
-	-	-	-
210	57.97	34.84	7.18
225	77.05	17.79	5.16
240	79.63	13.78	6.59
255	76.20	20.30	3.50
270	91.21	5.95	2.84
285	75.64	16.89	7.47
-	-	-	-
-	-	-	-
330	77.09	20.91	2.00
345	91.39	6.39	2.22
360	90.97	6.27	2.75

At these regions, the explained variance of PC1 varies between a maximum values greater than 90% and minimum value close to 46%. Explained variance of PC1 for the whole of the AIS is also shown in figure 4.11. Regions having high variance for PC1 are the same as regions where we have near ideal scenario as explained in section 4.1.2. It too ranges between a minimum 40% and a maximum values greater than 90%. PC1 is hence kept on focus as it accounts for the largest amount of variability.

Coefficient of contribution from each data set in the PC1 is given in table 4.5. Sites with explained variance greater than 70% also has near equal coefficient for each of the three data sets.

Table 4.5: Coefficient of each data set in PC1 at the 20 regions.

Longitude[°]	**Envisat**	**GRACE**	**RACMO**
15	0.49	0.60	0.63
30	0.54	0.59	0.60
45	0.55	0.59	0.60
60	-0.54	0.64	0.55
75	-0.57	0.56	0.60
90	0.51	0.49	0.71
105	0.58	0.59	0.56
120	0.58	0.56	0.59
135	0.58	0.57	0.59

150	0.57	0.65	0.51
165	-0.23	0.69	0.68
-	-	-	-
-	-	-	-
210	-0.14	0.71	0.68
225	0.60	0.61	0.51
240	0.60	0.55	0.58
255	0.64	0.50	0.59
270	0.59	0.57	0.57
285	0.59	0.61	0.53
-	-	-	-
-	-	-	-
330	0.60	0.64	0.48
345	0.58	0.57	0.59
360	0.59	0.57	0.57

PC1 obtained locally is plotted in the order of longitudes figure 4.12. The shaded region located between 165° and 210° E and 285° and 330° E correspond to regions where observations are not available due to the presence of permanent ice shelves.

A detailed time series analysis of the PC1 shows two positive and two negative anomalies in most of the regions during our period of study. It is consistent with the conclusions obtained in the previous section 4.3.2. A shift, gradually eastward, in the time of occurrence of the positive anomalies in PC1 while moving eastward from 15° to 285° E can be noticed. To further investigate this, a spatial analysis of the PC1 height changes is carried out. In this method PC1 height changes for each time interval is taken as a time series which implies March 2004 will have a time series with 24 values one each for each selected region, where 4 values are null since the presence of ice shelves. Even the time is taken as an average of 3 observations adjacent to it for easier representation and analysis i.e., March 2004 observation at 90° E will be average of observations from February, March and April 2004. The resultant matrix with time in y axis and longitude in x axis is plotted similar to figure 4.12 in figure 4.13.

Patterns similar to the previous figure (figure 4.12) is visible here too. The gradual eastward shift mentioned earlier, is clearly seen during the spatial analysis as positive anomalies traverse from 15° to 285° E during the period April 2004–June 2009. To investigate this further, we estimated the occurrence time of the positive

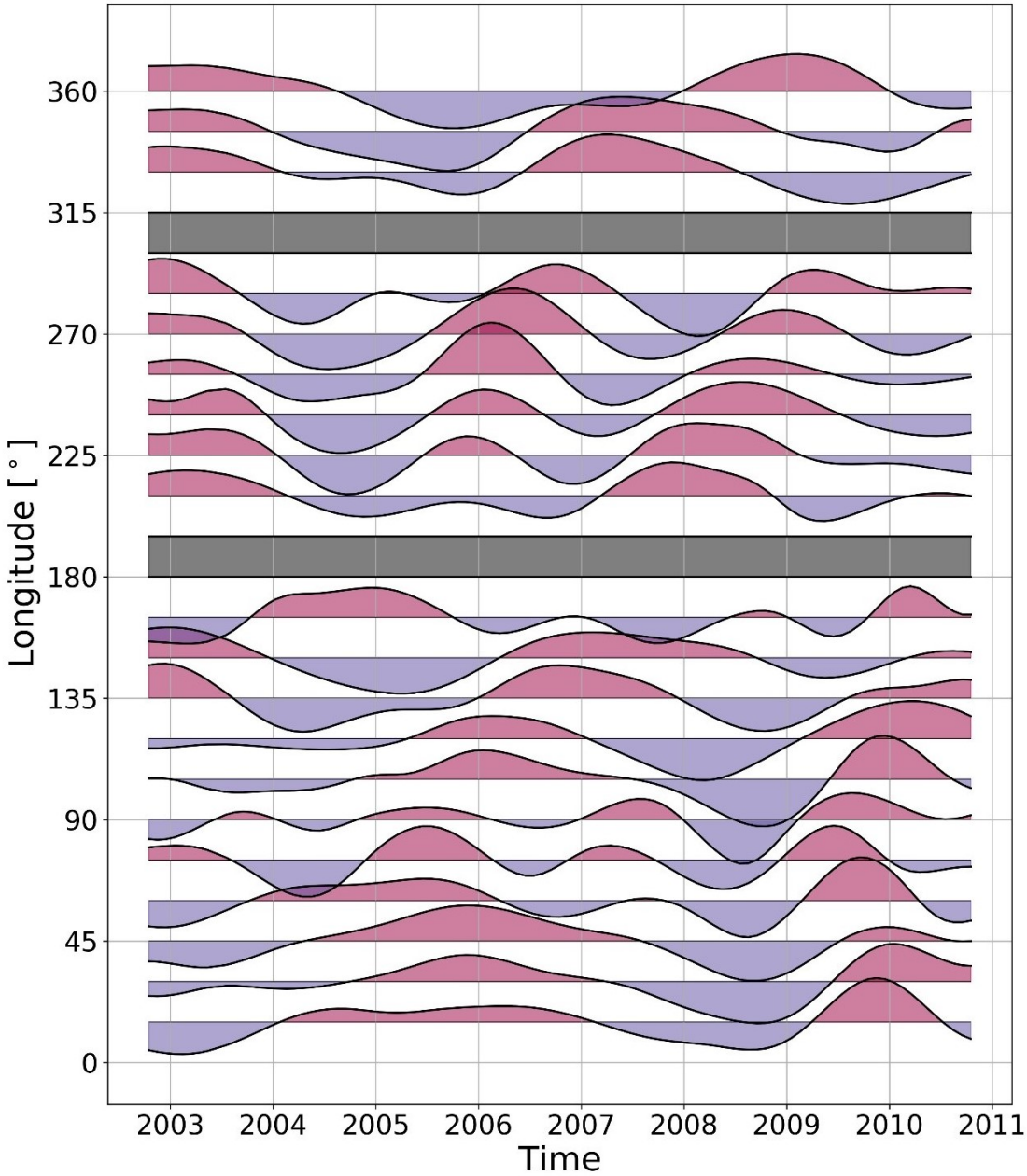

Figure 4.12: PC1 height changes ordered by longitude. The grey colored region represents ice shelves. Positive and negative anomalies are in red and blue, respectively. The abscissa is the time. The ordinate shows the amplitude of the signal and observations from each region sampled alongside the AIS coast at equal intervals.

anomalies that are longitudinally successive at each location based on figure 4.12. The key findings are summarized in figure 4.14.

The positive anomaly at 15° E has its first peak in July 2004. This anomaly shows a smooth trend of propagation up to 285° E, in almost 5 years, with 30° and 45° E being two exceptions. Between 15° and 30° E, the peak of the positive anomaly appears to be lagged by about one year and seems to circle the rest of the

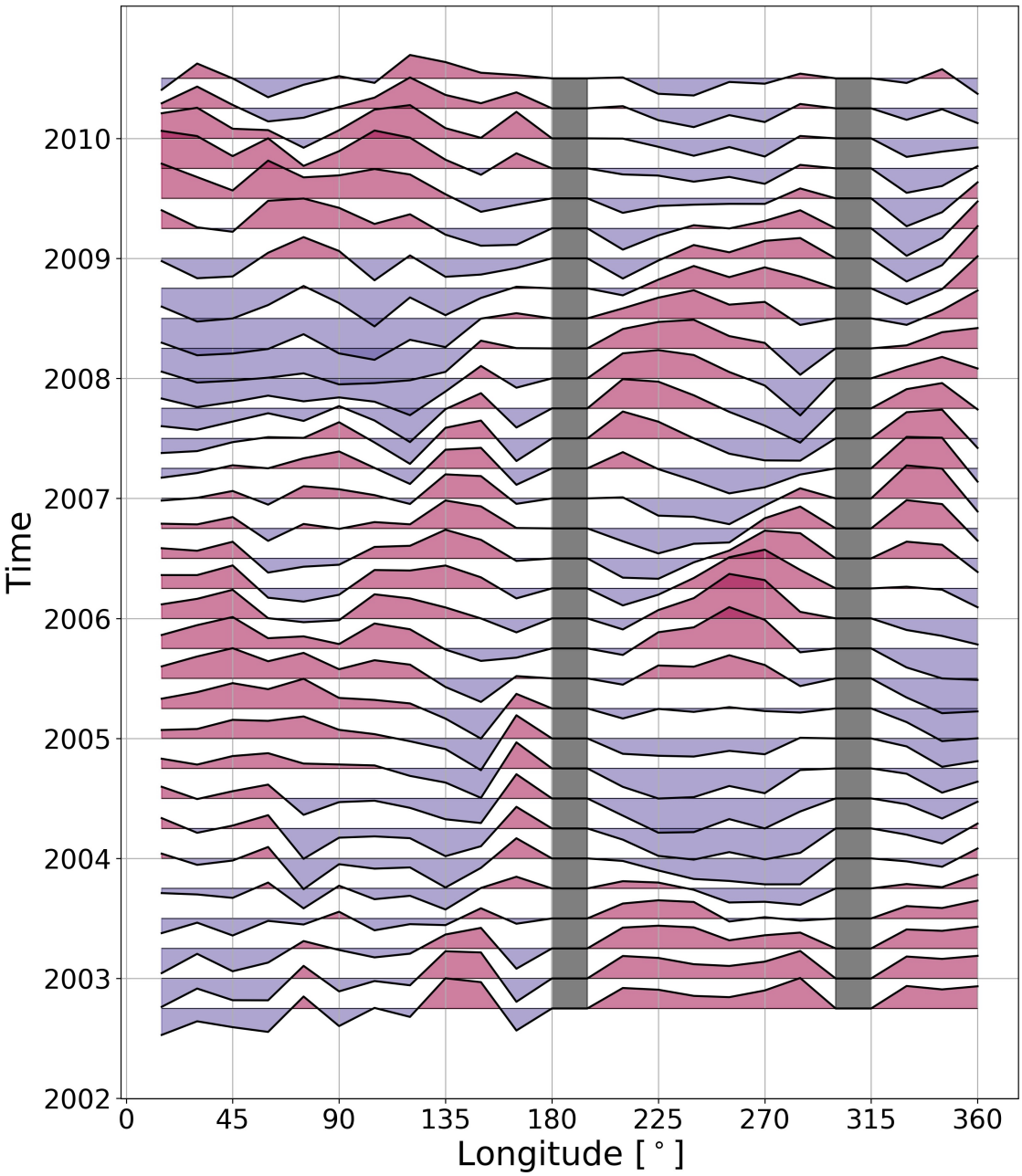

Figure 4.13: PC1 height changes ordered by time. The grey colored region represents ice shelves. Positive and negative anomalies are in red and blue, respectively. The abscissa is the longitude of region sampled alongside the AIS coast at equal intervals. The ordinate shows the amplitude of the signal and observations at each time period.

AIS at a quasi-constant rate after 45° E. We have estimated the period to traverse the whole AIS by avoiding the regions where we have explained variance lower than 70% for PC1 (table 4.4). Longitudes 75°, 90°, 165° and 210° E fall under this category. Hence, the mean time for encircling the entire AIS is about 5.5 years (green line in figure 4.14). We observe maximum amplitude for this anomaly at 45° E. The anomaly is the weakest at 165° E, which is the endpoint of a decreasing trend since 135 E. This also coincides with increasing distance from 65° S latitude, which

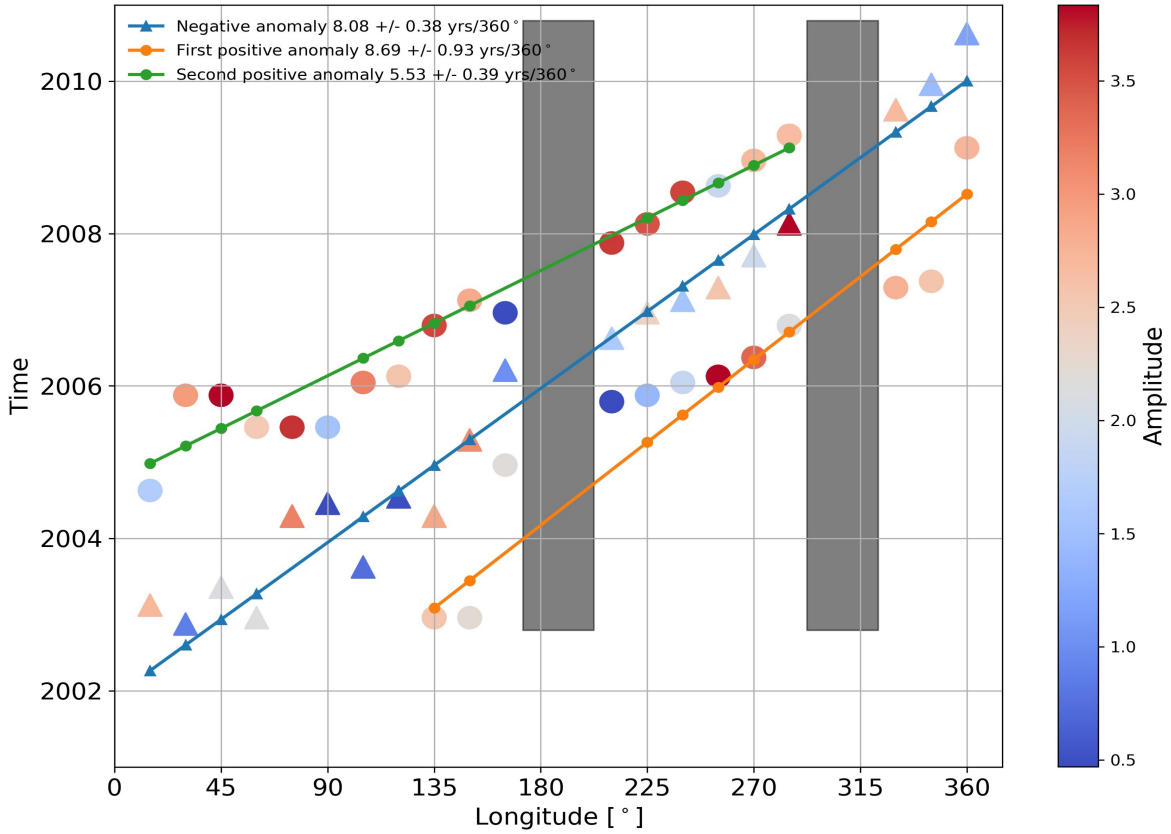

Figure 4.14: Time occurrence of anomalies in PC1 that are longitudinally successive around the AIS. Circles and triangles represent positive and negative anomalies, respectively. The abscissa is the longitude of region sampled alongside the AIS coast at equal intervals. The ordinate shows the time of occurrence of peak at each region. The color depicts the absolute amplitude of the anomaly at each location from PC1. Linear trends are estimated considering negative anomalies (blue), positive anomalies between 135° and 360° E (orange), and positive anomalies between 15° and 285° E (green), ignoring locations with variance < 70%.

reaches its maximum at 165° E. The same feature is observed at 255° E, where we have lesser amplitude compared to other sampling locations in the Antarctic Pacific (AP) sector (210° to 285° E).

Similar analysis is carried with the negative anomalies, as indeed we observe a negative anomaly originating in later half of 2002 at 15° E and propagating eastward till late 2010 at 360° E. Similarly, another trend is observed between 135° and 360° E of positive anomalies during December 2002 to January 2009. Both these trends take approximately 7.5 to 9.5 years to traverse across the AIS. As we observe, this phenomenon of propagation of anomalies is a continuous one, and we have not identified any particular starting point and ending point. These anomalies seem to be enhanced or diminished regionally.

To further understand the causes of these behavioral patterns in the inter-annual signal we study various climate anomalies influencing Antarctica and surrounding

systems in the next chapter.

Chapter 5

Influence of climate anomalies

The Antarctic system was found to be a subject of climate driven fluctuations with inter-annual periods [Schneider et al., 2012; Massom et al., 2010]. This is described using the variability in sea ice coverage in Southern Ocean (SO) over time. This variability is usually associated with various inter annual climate processes which can be both local and global influence. Among them, El Niño Southern Oscillation (ENSO) a global phenomenon brings along anomalies in and around Antarctica [Boening et al., 2012; Kwok et al., 2016; Deb et al., 2018]. Similar anomalies were detected which had a periodicity of 4 to 6 years and circle the AIS in 9 to 10 years namely Antarctic circumpolar wave (ACW), a large scale co-varying oceanic and atmospheric anomaly propagating eastward across the SO on sub-decadal time scales [Mémin et al., 2015; White & Peterson, 1996; Peterson & White, 1998; White & Simmonds, 2006]. Climate processes like this are quantified using a climate index or a combination of multiple climate indices. A climate index is a calculated value that can be used to describe the state and the changes in the climate system. It allows a statistical study of variations of the dependent climatological aspects, such as analysis and comparison of time series, means, extremes, and trends.

Variability of similar scales is found in the inter annual signals across the AIS as discussed in section 4.3.2. We discuss the influence of various climate processes in the next sections.

5.1 El Niño Southern Oscillation

ENSO is one of the major climate variability occurring on the timescales of 2–7 years and modifying both atmospheric and oceanic parameters globally. This includes anomalies in SST, sea ice extent, ice shelf thinning rates, and surface melt events in and around AIS [Boening et al., 2012; Kwok et al., 2016; Deb et al., 2018]. ENSO also causes simultaneous high and low pressure systems leading to larger cloud formation and precipitation. This often leads to fluctuations in precipitation

and hence in the normal mass change trends [Boening et al., 2012; Sasgen et al., 2010; Bodart & Bingham, 2019].

Though ENSO is a single climate phenomenon, it has three states, or phases, it can be in. The two opposite phases, “El Niño” and “La Niña,” require certain changes in both the ocean and the atmosphere because ENSO is a coupled climate phenomenon. “Neutral” is in the middle of the continuum.

During an El Niño phase, the central and eastern tropical Pacific Ocean surface warms, or has a SST value greater than the average (figure 5.1). It coincides with an increase in precipitation over the tropical Pacific Ocean. This also forces the low-level surface winds blowing from east to west along the equator (easterly winds) to weaken or rarely start blowing in the opposite direction (from west to east).

Whereas during a La Niña event, the vice versa happens. The central and eastern tropical Pacific Ocean surface cools or has SST values lower than average (figure 5.1). Precipitation too reduces over the central tropical Pacific Ocean. It also coincides with normal easterly winds along the equator and it becoming even stronger.

And in the neutral phase, tropical Pacific SSTs are generally close to average. But there happens periods during which the ocean can look like it is in an El Niño or La Niña state, but the atmosphere not representing the same (or vice versa). Therefore, the conditions oscillate between these three phases time-to-time. Figure 5.1 represents the anomalies in SST during El Niño and La Niña.

Fluctuations associated to ENSO are usually quantified using climate indices like the Southern Oscillation Index (SOI) or the Oceanic Niño Index (ONI), which provides a measure of the strength of the related events.

5.1.1 Southern Oscillation Index

The Southern Oscillation Index (SOI) is one of the measures of the large-scale fluctuations in air pressure taking place between the western and eastern tropical Pacific during El Niño and La Niña episodes. This index is driven by the differences in air pressure anomaly measured at Tahiti and Darwin, Australia. More precisely it is defined as the doubly standardized difference in mean sea-level pressure between Tahiti (131° E 13° S) and Darwin (210° E 18° S) [Ropelewski & Jones, 1987; Parker, 1983]. It can be expressed as,

$$SOI = \frac{(StandardizedTahiti - StandardizedDarwin)}{MSD} \tag{5.1}$$

where standardized Tahiti and standardized Darwin can be expressed as,

$$StandardizedX = \frac{(ActualXSLP - MeanXSLP)}{StandardDeviationX} \tag{5.2}$$

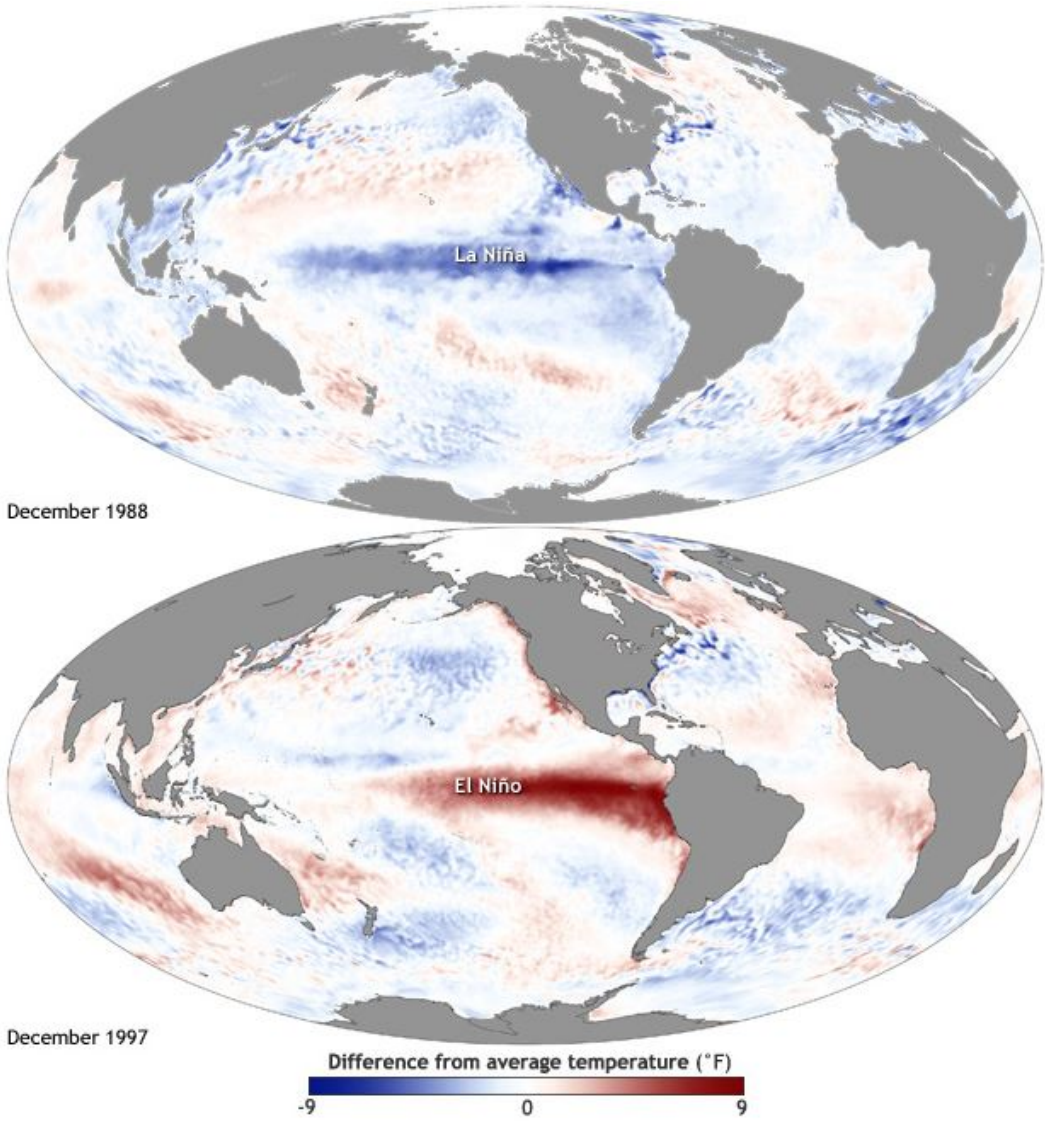

Figure 5.1: Thematic maps of anomalies in sea surface temperature in the Pacific Ocean during a strong La Niña event (top, during December 1988) and El Niño event (bottom, during December 1997). Maps by NOAA Climate.

where standard deviation X can be expressed as,

$$StandardDeviationX = \sqrt{\sum(actualXSLP - meanXSLP)^2/N} \tag{5.3}$$

where N is the number of months and monthly standard deviation (MSD) is taken as,

$$MSD = \sqrt{\sum(StandardizedTahiti - StandardizedDarwin)^2/N} \tag{5.4}$$

where N is the number of months and X can be both Tahiti and Darwin respectively while calculating standardized air pressure anomaly at each region. Note

the anomalies are departures from the 1981-2010 base period. It is provided by the Climate Prediction Center (CPC) of the National Oceanic and Atmospheric Administration (NOAA) (`https://www.cpc.ncep.noaa.gov/data/indices/` accessed on 30 June 2020).

The smoothed time series of the SOI correspond very well with changes in sea surface temperatures in the eastern tropical Pacific. Negative values of the SOI represents air pressures lower than normal pressure at Tahiti and greater than normal air pressure at Darwin indicating an El Niño event where ocean warms across the eastern tropical Pacific. The vice versa happens during a positive phase in SOI and thus a La Niña event with cooler ocean across the eastern tropical Pacific. Figure 5.2 shows the variations of SOI since 1990.

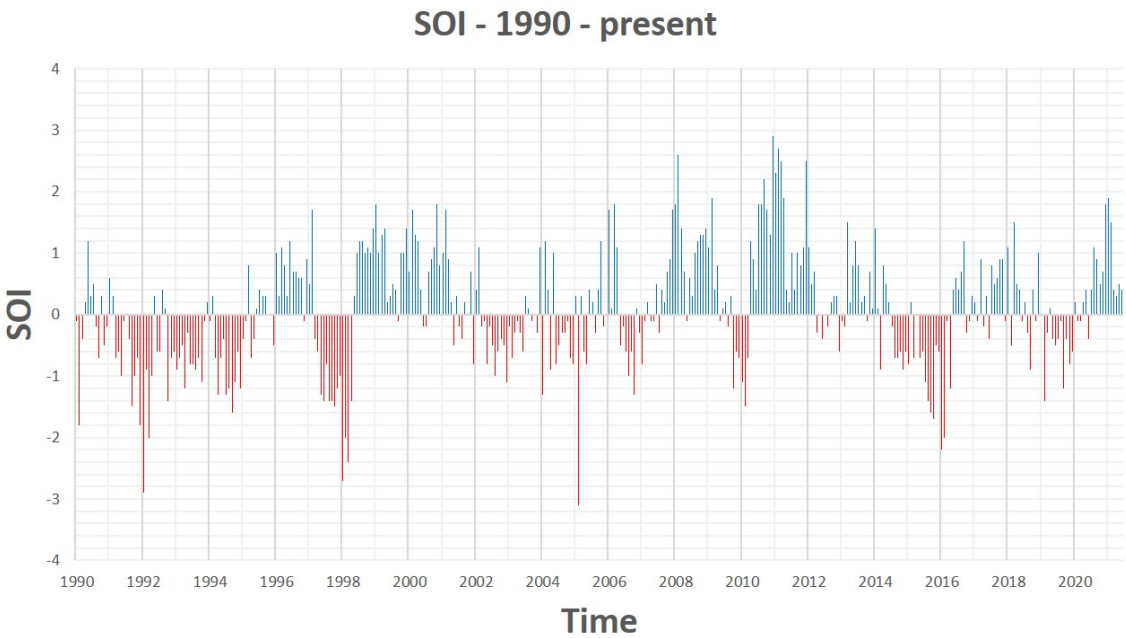

Figure 5.2: SOI vs time from 1990 to present to indicate El Niño or La Niña periods and their magnitude. Positive SOI values are in blue and negative values are in red.

The time series of the SOI since 1990 (figure 5.2), depicts that the El Niño-La Niña cycle has an average period of about four years whereas it varies in the range of 2 to 7 years based on historical records. Between 1980 and 2000, the cycle was very active with with 5 El Niño episodes (1982/83, 1986/87, 1991-1993, 1994/95, and 1997/98) and 3 La Niña episodes (1984/85, 1988/89, 1995/96). Out of which, there were the strongest El Niño episodes of the century (1982/83 and 1997/98) and consecutive periods of El Niño conditions between 1991 and 1995 without a La Niña event. This cycle seems to have considerable variability between one decade to another.

Sasgen et al. [2010] have discussed the influence of ENSO in mass change patterns

using SOI, GRACE solutions, and weather model data. They have found that the inter-annual mass variability along the Antarctic Peninsula and the Amundsen Sea sector, obtained from GRACE, contains ENSO signatures. These mass estimates are exclusive of offset, linear trend, and annual harmonic and are found to be mainly a consequence of accumulation variations governed by changes in precipitation rates. Similarly, ENSO influence over Antarctic ice shelves is also well discussed using weather and altimetry data by Paolo et al. [2018]. They have been able to link ice-shelf height variability in the AP sector with changes in the regional atmospheric circulation driven by the ENSO with indices including ONI.

5.1.2 Oceanic Niño Index

The Oceanic Niño Index (ONI) is another climate index used largely to measure the strength of a La Niña or an El Niño occurrence. It has become the primary indicator that NOAA uses for identifying El Niño (warm) and La Niña (cool) events in the tropical Pacific. It is the running 3-month mean SST anomaly for the Niño 3.4 region (i.e., 5° N-5° S, 120° - 170° W) from the ERSST.v5 (Extended Reconstructed Sea Surface Temperature) [Huang et al., 2017]. It is also provided by CPC of the NOAA (`https://origin.cpc.ncep.noaa.gov/products/analysis_monitoring/ensostuff/ONI_v5.php` accessed on 30 September 2020). Events are defined as 5 consecutive overlapping 3-month periods at or above the +0.5° anomaly for warm (El Niño) events and at or below the -0.5° anomaly for cold (La Niña) events. These values makes it possible to classify events into weak (with a 0.5 to 0.9 SST anomaly), moderate (1.0 to 1.4), strong (1.5 to 1.9) and very strong ($\geq$ 2.0) events. For an event to be categorized as weak, moderate, strong or very strong it must have equaled or exceeded the threshold value for each class at least 3 consecutive times.

From figure 5.2 and figure 5.3 of the SOI and ONI respectively, it can be concluded that they are anti-correlated. Positive values of ONI indicate an El Niño event whereas for SOI positive values indicate a La Niña event and vice versa. Table 5.1 shows classification of periods since 1950 based on the occurrence of El Niño or La Niña events using ONI. They are further grouped into weak, moderate, strong and very strong versions of either El Niño or La Niña. We have used ONI for our studies with the measurements from the AIS.

Mémin et al. [2015] have detected anomalies with a period of about 4–6 years in a combined analysis of surface-mass and elevation changes between August 2002 and October 2010. Our results suggest at least 44% of the total studied area have periods between 4 and 6 years (class B in Table 4.3). By using climate model driven height change estimates for our study, we confirm that the inter-annual geodetic

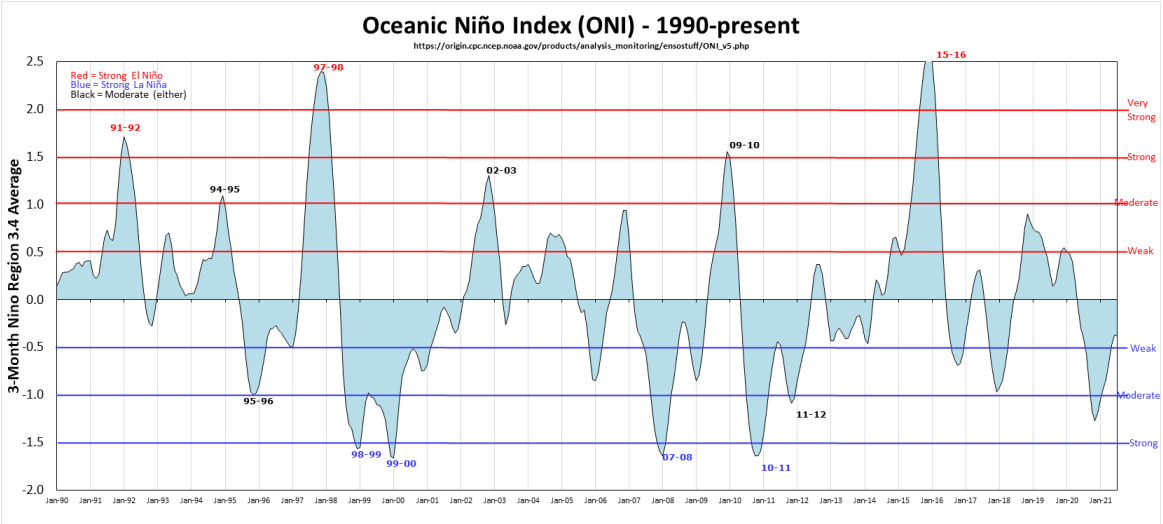

Figure 5.3: ONI vs time from 1990 to present to indicate El Niño or La Niña periods and their magnitude. El Niño or La Niña events fall into four categories: weak, moderate, strong and very strong.

anomalies observed in Antarctica are due to changes in atmospheric conditions. Interestingly, Zhan et al. [2021] associated climate related events to dominate mass change trends in AIS by carrying out a complex principal component analysis. The frequency of their primary component matches with our major period class.

Table 5.1: Periods since 1950 to present classified into groups of El Niño or La Niña events based on their magnitude into weak, moderate, strong and very strong.

El Niño				La Niña		
Weak	**Moderate**	**Strong**	**Very Strong**	**Weak**	**Moderate**	**Strong**
1952-53	1951-52	1957-58	1982-83	1954-55	1955-56	1973-74
1953-54	1963-64	1965-66	1997-98	1964-65	1970-71	1975-76
1958-59	1968-69	1972-73	2015-16	1971-72	1995-96	1988-89
1969-70	1986-87	1987-88		1974-75	2011-12	1998-99
1976-77	1994-95	1991-92		1983-84	2020-21	1999-00
1977-78	2002-03			1984-85		2007-08
1979-80	2009-10			2000-01		2010-11
2004-05				2005-06		
2006-07				2008-09		
2014-15				2016-17		
2018-19				2017-18		

Correlation coefficient maps between the ONI and inter-annual height changes obtained from Envisat, GRACE, and RACMO are given in figure 5.4.

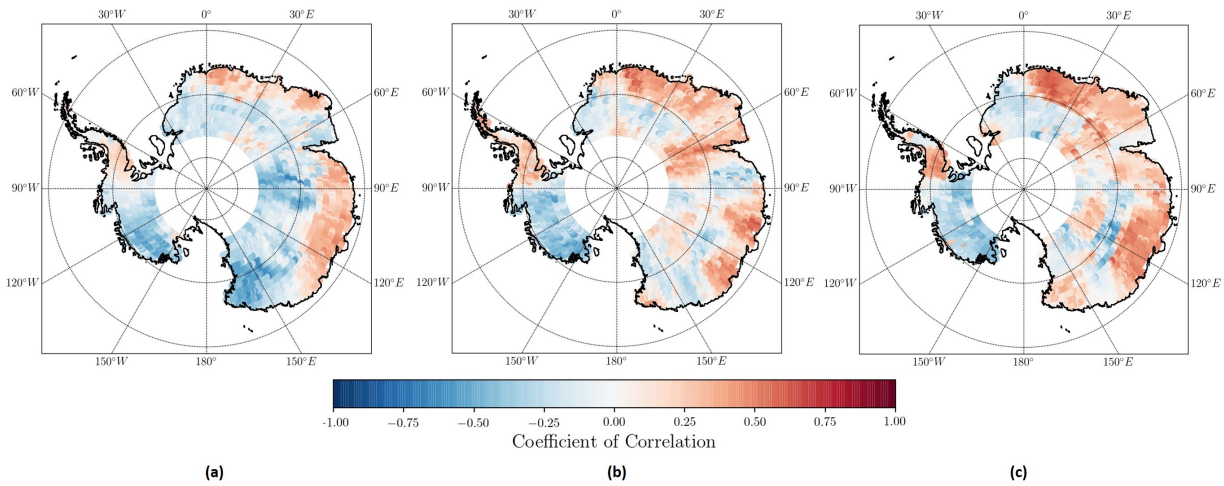

Figure 5.4: Correlation maps between ONI and inter-annual height changes estimated from (a) ENVISAT, (b) GRACE, and (c) RACMO. Positive and negative correlation coefficients are in red and blue, respectively.

Figure 5.4 reveals the influence of ENSO on the height change patterns as the correlation coefficient ranges between -0.7 and 0.7 through the whole AIS. Positive correlations are commonly found in the East Antarctica beyond 0° E up until 130° E in every map along the coast. This coincides with area where we find inter-annual signals having periods in the range of 4 to 6 years and higher amplitude values. Maximum positive correlation is obtained in regions around DML and WL, especially when height changes are derived from RACMO and GRACE. Most of the regions in the West Antarctica exhibit negative correlation coefficients, which is consistent with what we observe in the periodicity maps. Zhang et al. [2021] also attributed the inter-annual changes in ice mass over the AIS to precipitation related events associated with ENSO analyzing GRACE data and other mass balance estimates. Even though they limited studies based on regional estimates, they, too, discussed about varying characteristics between East Antarctica and West Antarctica. We further discuss climate process that might cause this varying behavior of the inter annual signals in West Antarctica.

5.2 Southern Annular Mode

The SAM or Antarctic Oscillation is the dominant mode of atmospheric variability in the Southern Hemisphere (SH) imposing a major shift in the broad-scale climate of the hemisphere influencing precipitation and temperature on month-to-month and inter-annual timescales [Marshall, 2003]. It is quantified based on the zonal pressure difference between the latitudes of 40° S and 65° S. The station-based SAM index uses records from 6 stations located close to 65° S and 6 stations located near 40° S exist since 1957 (figure 5.5).

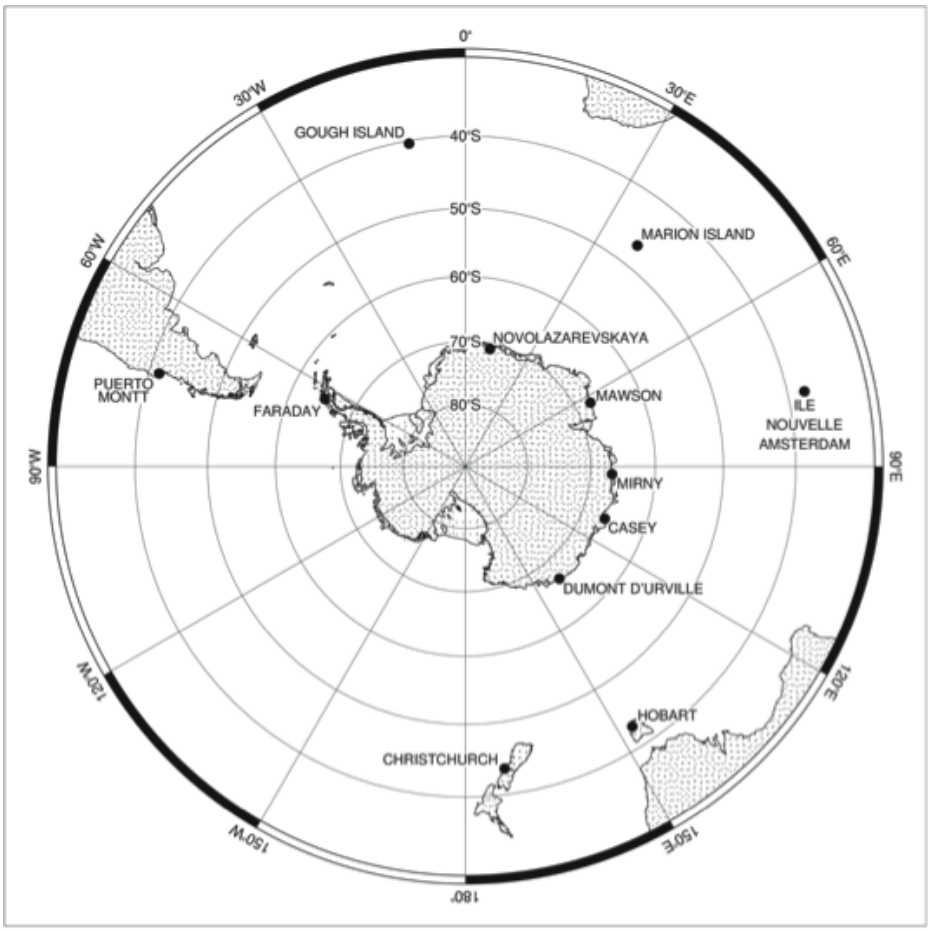

Figure 5.5: Locations of the 12 stations used to calculate the observation-based SAM index. 6 locations are close to 65° S and leftover 6 are close to 40° S. Adapted from Marshall [Marshall & National Center for Atmospheric Research Staff, 2018].

Positive values in this station-based SAM index indicate stronger-than-average westerlies over the mid-high latitudes (50° S – 70° S) and weaker westerlies in the mid-latitudes (30° S–50° S). SAM index since 1990 thus obtained is shown in figure 5.6. Studies indicate the possibility of the strong positive SAM event during 2010 to have caused the dry conditions in southwest Western Australia.

Depiction of observation based SAM index helps us understand the nature of SAM events. SAM events either positive or negative are more frequent compared to ENSO based on SOI and ONI (figure 5.2 & figure 5.3).

The influence of ENSO on the AIS is either enhanced or diminished depending upon the phase of SAM [Fogt et al., 2011]. Mostly the significant relationship is brought about by La Niña events occurring with positive phases of the SAM and vice versa with El Niño events and negative phases of SAM. The South Pacific teleconnection magnitude is found to be strongly dependent on the SAM phase. Teleconnections too are mostly found with El Niño and SAM- or La Niña and SAM+. This variations in the South Pacific ENSO teleconnection is associated with

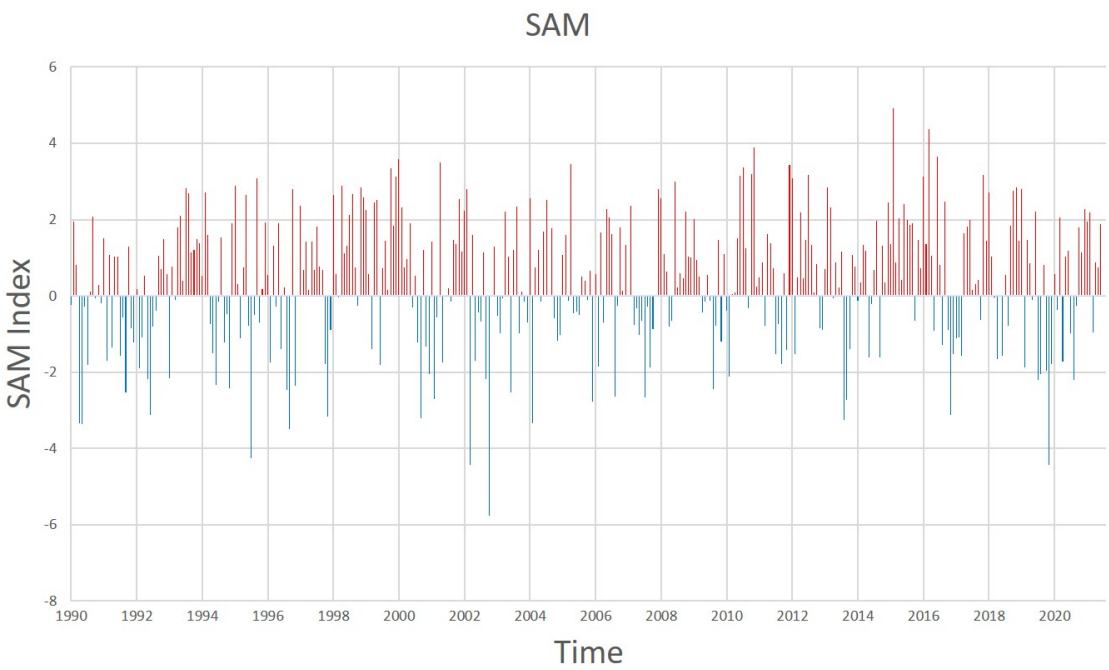

Figure 5.6: Seasonal values of the observation-based SAM index since 1990 to present. Positive values in red and negative values in blue.

the interaction of the ENSO anomalies and SAM linked zonal pressure differences. During the teleconnected phases, the zonal pressure anomalies in the Pacific act to reinforce the circulation anomalies in the mid-latitudes, altering the circulation in to maintain the ENSO teleconnections. In the reversed cases, the anomalies oppose each other in the mid-latitudes, forcing a reduction in the magnitude of the ENSO teleconnection at high latitudes [Fogt et al., 2011].

5.3 Amundsen Sea Low

The ASL or the Amundsen–Bellingshausen Seas Low (ABSL) is a quasi-stationary area of climatological low pressure system that exerts considerable influence on the climate of West Antarctica. It is present because of the large number of synoptic-scale and sub-synoptic-scale low pressure systems in this sector of the circumpolar trough [Fogt et al. 2012]. The formation and enhancement of these systems is largely due to the asymmetry of the Antarctica both geographically and topographically [Lachlan-Cope et al. 2001; Walsh et al. 2000]. There exists large seasonal variability in both location and central pressure of the minimum mean sea level pressure (MSLP) associated with the ASL [Fogt et al. 2012; Turner et al. 2013b]. It influences the wind anomalies, snowfall, temperature patterns, and sea ice extent. Atmospheric variations in this region is the largest in the Southern Hemisphere and this exhibits significant correlations with other variability like the SAM and ENSO.

The circulation in the ASL sector region is strongly influenced by large-scale patterns of atmospheric variability, such as the SAM and ENSO [Kwok and Comiso 2002; Turner 2004]. The ASL may be considered as a Southern Hemisphere analog to the Aleutian Low due to its association with ENSO variability across basins. Hence, the ASL plays a significant role in the climate variability across West Antarctica and the oceans bordering it. It is challenging to have a single index for the variability driven by ASL as the region undergoes extreme changes and the low pressure center migrates. Figure 5.7 shows an snapshot of seasonal mean sea level pressure around Antarctica where the low pressure center is marked using a '+' symbol.

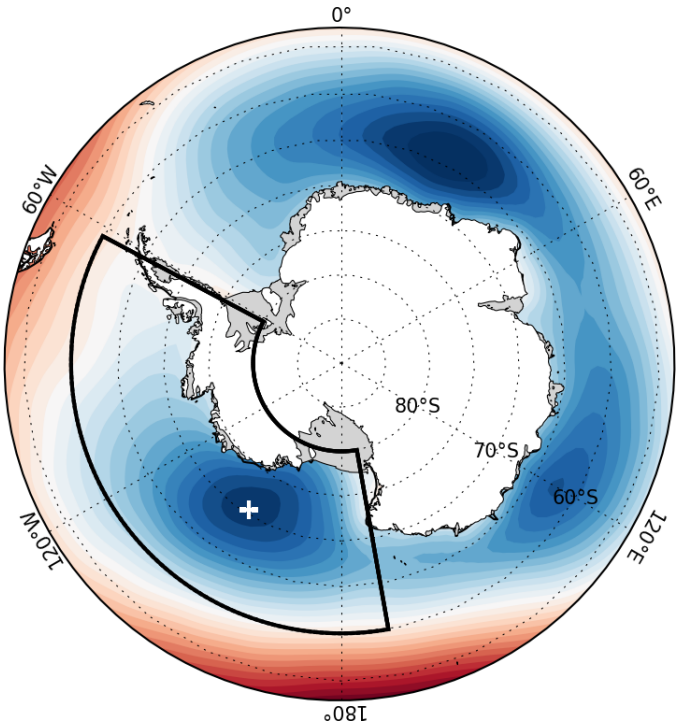

Figure 5.7: An instance of seasonal mean sea level pressure differences around Antarctica with the geographical location of the ASL marked with a '+' symbol where up to 10 hPa difference is experienced on an average. Lower mean sea level pressure values are in blue and the higher mean sea level pressure values in red. The black line box represents the region used to derive the ASL indices. Adapted from Hosking [Hosking & National Center for Atmospheric Research Staff, 2020].

Multiple indices associated with the ASL, like its absolute and relative central pressure, and the coordinates of the region of these central pressures, derived from the ECMWF reanalysis are given in (figure 5.8).

Figure 5.8 indicates the ASL shifting across 180° E and 300° E at short intervals. But 11 month smoothed time series indicates that it is largely concentrated in the Antarctic Pacific sector (200°-260° E). Similar to the variations in SAM, the ASL too seems to have more frequent variabilities compared to the ENSO. These differences

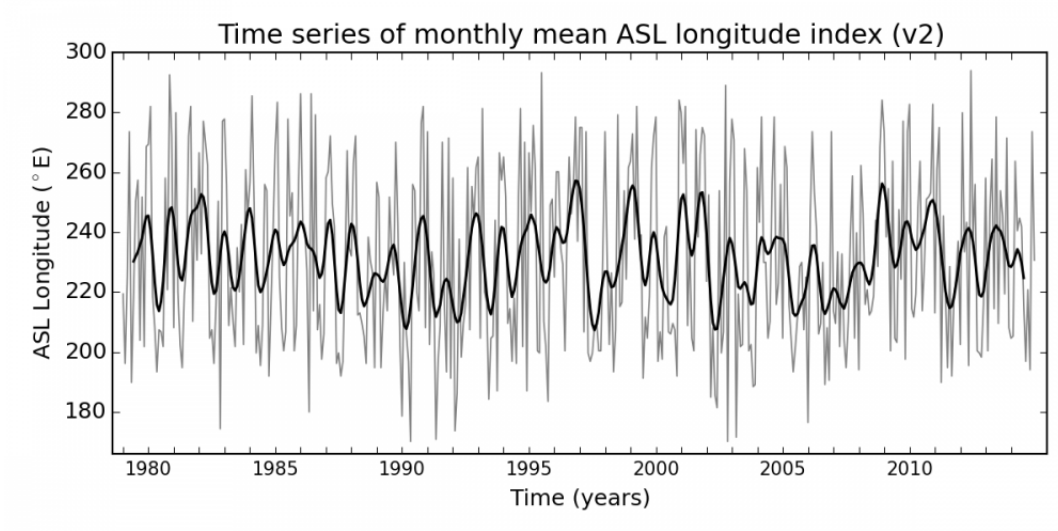

Figure 5.8: Time series of monthly shifts in ASL's longitudinal location derived from ERA-Interim data (grey line) along with the 11-month smoothed time series (black line). Adapted from Hosking [Hosking & National Center for Atmospheric Research Staff, 2020].

can supposedly explain the variation in behavior of inter annual signals between East and West Antarctica.

Given the broader frequency content of SAM and ASL, these drivers are the likely cause for deviation of period values from class B (4 to 6 years) in West Antarctica and the Antarctic Peninsula. These regions have periods less than 4 years (class A), which may be due to the influence of the SAM or the ASL in phase or out of phase with the ENSO. Depending upon the phase and the time of occurrence, ASL and SAM either strengthen or weaken the ENSO signature. The influence of ASL and SAM is strongly felt along the Amundsen Sea sector, as well as in the Antarctic Pacific sector, which overlaps with above mentioned regions [Paolo et al., 2018].

5.4 Antarctic Circumpolar Wave

The ACW is a phenomenon where large scale co-varying oceanic and atmospheric anomalies propagate eastward across the Southern Ocean (SO) on sub decadal time scales [White & Peterson, 1996; Peterson & White, 1998; White & Simmonds, 2006]. This phenomenon influences weather variables, like SST, sea ice extent, sea level pressure (SLP), and wind velocities, which is similar to what ENSO does. A schematic representation of various parameters in the SO is shown in figure 5.9.

ACW is commonly found as a wavenumber-2, wavenumber-3, and the Pacific-South American (PSA) pattern in studies associated with a combination of oceanic and atmospheric models [Christoph, 1998; Mo, 1985]. A zonal or a hemispheric

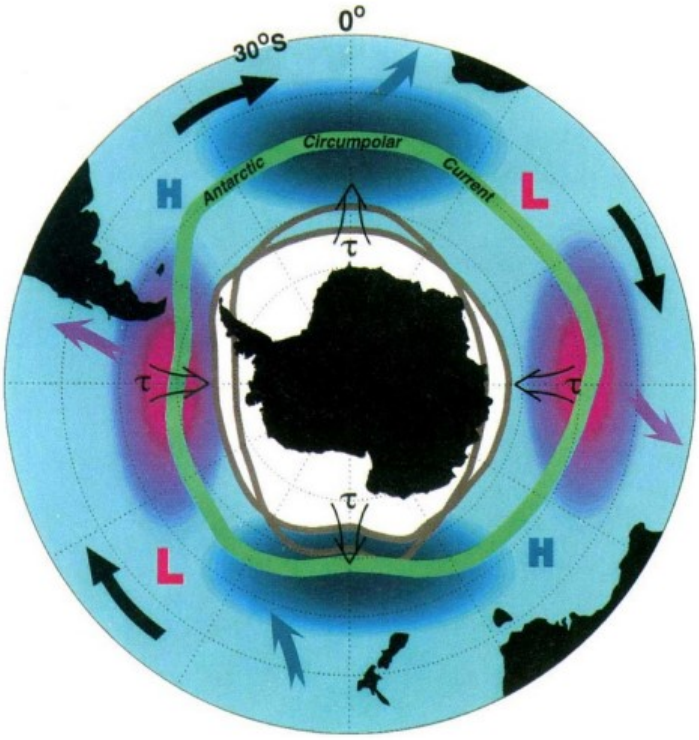

Figure 5.9: Simplified schematic summary of inter annual variations in the SO. Sea surface temperature (warm in red and cold in blue), atmospheric sea-level pressure (high, H and low, L), meridional wind stress, and sea ice extent (grey lines), together with the mean course of the Antarctic Circumpolar Current (green). Sea-ice extent is based on the overall 13-year average. Heavy black arrows depict the general eastward motion of anomalies, and other arrows indicate communications between the circumpolar current and the more northerly subtropical gyres. Adapted from White & Peterson [1996].

wavenumber refers to the dimensionless number of wavelengths fitting within a full circle around the globe at a given latitude. Few studies have tried to interlink both ENSO and ACW together [Peterson & White, 1998]. Prior studies investigating the characteristics, origin, effects and propagation of the wave in different time periods summarized the wave as a combination of wave-2 and wave-3 patterns. A wave-2 pattern is more associated with ENSO's tropical standing mode while a wave-3 pattern comes into play on weakening of the ENSO [White & Cherry, 1999; White, 2000; Connolley, 2002; Fischer et al., 2004; Cai & Baines, 2001]. A wave-2 pattern usually takes around 8 to 10 years to circumnavigate and has a periodicity of 4 to 5 years, which is similar to that of the ENSO phenomenon [White & Peterson, 1996; Peterson & White, 1998].

White and Peterson have also found that, in between two ENSO occurrences, the anomalies in temperature and pressure are propagated eastwards by the ACW into the Atlantic and Indian ocean portions of the SO [White & Peterson, 1996]. Long-term studies have depicted inter-decadal changes to the behavior of this wave

possibly due to a multitude of reasons [Cerrone et al., 2017]. These include warming of the tropical and subtropical oceans and depletion of the ozone layer and variability of the ENSO [Bian & Lin, 2012; White & Annis, 2004]. Changes also include the equatorward expansion of the wave causing subtropical south Indian Ocean to warm instead of the subtropical South Pacific Ocean which later cools. Earlier studies have indicated possibilities of weakening and decelerating of the anomaly propagation in the Indian Ocean sector of Antarctica (0° to 50° E) due to topographic meandering where the region gets warmer during winter [Nunico et al., 2011]. Figure 5.9 hints at interactions between the Antarctic Circumpolar Current and the more northerly subtropical domains.

Ice core serve as important records of climate. And these cores from DML of sea salt aerosol deposition, have depicted a sub 4- to 5- year quasi-periodic signal indicating ENSO and ACW influence on the climate in the AIS [Fischer et al., 2004]. This was then further complemented by a study where an 8- year rotating wave with a 4- year apparent periodicity was observed in the temperature variations at 10 automatic weather stations around the continent [Autret et al., 2013]. Similarly, Mémin et al. [2015] found anomalies in surface mass and elevation change estimates from GRACE and Envisat receptively which too had a periodicities ranging between 4 and 6 years, and circumnavigating AIS in 9 to 10 years. These too were attributed as ACW or ENSO contributions over the AIS.

During the characterization phase of the inter-annual signals, we observe above average amplitude values within a buffer of ∼600 km or 5° from the AIS coastline in figure 4.10. A wavenumber-2 pattern is observed at most of the locations along this buffer when sampled at equal intervals of 15° and after a PCA (figure 4.12). Anomalies had a dominant periodicity across the AIS in the range of 4 to 6 years. These anomalies show an eastward propagating pattern from 15° to 360° E encircling the AIS in about 8 years with irregular velocities.

Chapter 6

General conclusions

In this chapter, we put together our results and summarize our key findings from each chapter. We also share our perspective about the relevance of this study and future possibilities.

6.1 Conclusions

In this thesis, our aim was to investigate inter-annual variability in the AIS combining multiple geodetic observations (altimetry and gravimetry) and outputs from the regional climate model, RACMO2.3p2. The methodology we adopted is summarized as a flow char in figure 6.1.

In the process, we estimated height changes from gravity changes as proposed by Wahr et al. [1998] and from weather variables using the firn compaction model of Li and Zwally [2015]. Implementing the firn compaction model for the whole AIS involved understanding varying climatic conditions across the ice sheet and various sub processes involved during compaction. Estimates thus obtained from the model and GRACE were then combined with elevation changes from Envisat mission for the common period 2002–2010.

Inter comparison were made between these estimates by carrying out a correlation and regression analysis. Estimates of residual changes showed good agreement between each other across the AIS especially along the coasts where variations of large magnitude were found to occur. SEH from GRACE solutions was found to be the comparable metric to estimate of changes from RACMO and Envisat. In this process, the sensitivity associated with each estimation technique was explained and their limitations were made note of. We then employed the EMD technique to extract inter-annual signals which represents an average 60% of the monthly height changes (figure 4.6). During this process, we isolate inter-annual height change pat-

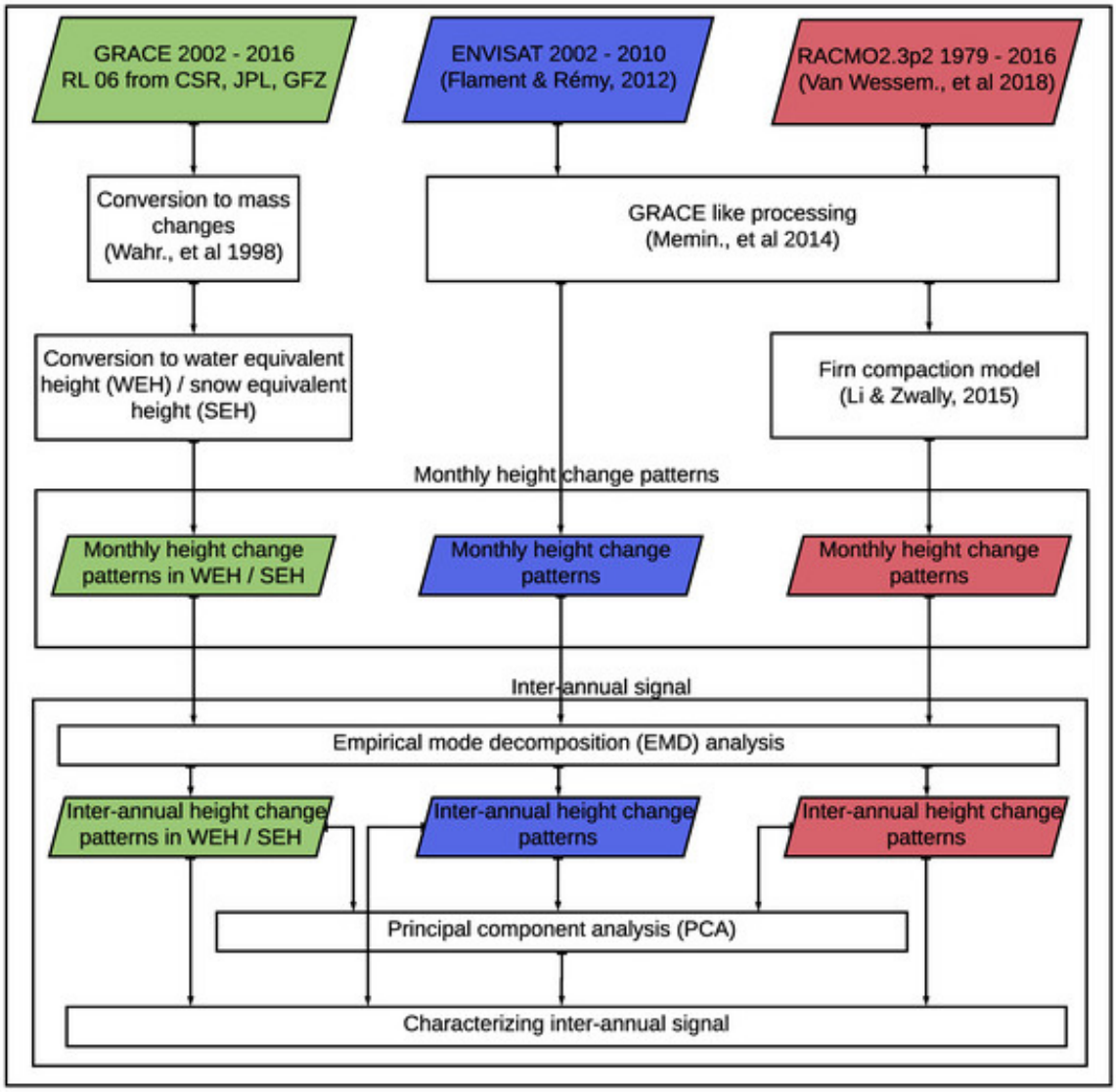

Figure 6.1: Flowchart of the study. Parallelogram represents data used and rectangle represents a process. The arrow points towards direction of data flow.

terns by removing noise and components with very high (greater than 0.5 $year^{-1}$) and very low (less than 0.125 $year^{-1}$) frequencies.

We use the least squares method to find the best fitting period and amplitude for the extracted inter-annual signals. The periods ranges between 2 and 8 years, and was grouped into three classes based upon its distribution in the AIS; class A with periods less than 4 years, class B with periods between 4 and 6 years and class C with periods greater than 6 years. Class B (4–6 years) covers the largest portion of the study area, closely followed by class A (less than 4 years) (table 4.3). Class B is dominant by a small margin in observations from RACMO whereas class A is dominant by a small margin in observations from GRACE and Envisat.

Period and amplitude maps (figure 4.8 & figure 4.10) indicate the likely influence of inter-annual climatic processes on the ice sheets. Inter-annual signal along the coast of East Antarctica has periods similar to that of ENSO with positive correlation up to 0.7 with the ENSO index, ONI (figure 5.4). Whereas differences in West Antarctica and Antarctic Peninsula figure 4.8 & figure 4.10) can be explained based upon the influence of phenomenon, like SAM and ASL, in the Antarctic Pacific (AP) sector.

A PCA of inter-annual signals along the coast at equal intervals reveals an anomaly propagating eastwards with a sub-4-year period mostly (figure 4.12). Similar anomaly was also found when the first principal component was processed temporally along the coast (figure 4.13). This anomaly might reflect a possible influence of the ACW on the AIS . ACW supposedly carries the climatic anomaly across the AIS, influencing regions along the coast with varying rates of propagation which is dependent on local features in 8-10 years. Indeed such a particular anomaly seems to take 6–8 years to encircle AIS as we observe it in different sectors during our period of study, and its magnitude of influence, too, varies locally.

Altogether we found the AIS being influenced by multiple inter annual climate anomalies which influences various processes like precipitation, sea level pressure, temperature, etc. and hence modify the nominal mass balance patterns. We were able to establish a climate origin to these inter-annual anomalies as these signatures were found in our estimates from the climate model RACMO, which is purely driven by variations in the regional climate. ENSO, SAM, ASL and ACW are few of them which we found influencing the nominal height change patterns. These anomalies have different characteristics having competing influences and also undergo decadal changes which makes it more complex to differentiate and understand.

6.2 Future perspectives

Understanding the inter annual variability of changes in the AIS is very important due to multiple reasons. It helps in accurately estimating the mass balance of the AIS independent of the inter-annual climate process components and thus the consequential variations in global mean sea level. It is important to understand the evolution in the properties of these inter annual climate processes on the back drop of climate change. IPCC reports have warned us on the increasing occurrence of extreme climate events with larger intensity causing irreversible changes. The exact understanding of these processes and their influences is necessary to make future

forecasts of mass balance or mean sea level changes in different warming scenarios. Once properly understood or quantified, it will be interesting to separate signatures associated with each process from the estimates of changes to the ice sheet.

Unlocking the key of inter-annual variability will help to improve our understanding of solid Earth's response to changes at the surface. GIA models can be developed or better understood with the help of long term GRACE solutions and inter-annual variability.

Research in this direction can be enhanced by including continuous observations for longer periods. This include observations from in-situ or observations from systems like automatic weather stations where we see maximum influence of these inter-annual climate anomalies. AWS can give continuous estimates of variables like accumulation, temperature, pressure, wind velocities at different time intervals. Another way of monitoring changes could be having measurements of Earth surface deformation from GPS stations due to variations in SMB. This could also be combined with surface mass changes observed by GRACE to reach better estimates of AIS mass balance and understanding the inter-annual variability.

Studies for longer periods is possible if we could integrate observations from other spaceborne missions. This include observations from Cryosat-2 which got operational in early 2010 and is still observing changes to the ice sheet. Other radar altimetry mission observations which could possibly be integrated include SARAL/AltiKa, Sentinel-3 missions, etc. ICESat-2, a follow on mission to ICESat will use lasers and a very precise detection instrument to measure changes in ice sheet elevation. GRACE-FO, a follow on mission to GRACE can also help in extending time series and having more robust estimates of changes since 2018. Upcoming missions like CRISTAL (planned for mid-2025) indicate continuity in the pursuit of science in this direction.

Studies to better understand various parameters measured by radar altimeters and other instruments holds large relevance in accurately quantifying the influence of inter-annual climate processes. This happens as the ice sheet surface properties vary due to the influence of multiple competing processes. New studies combine multiple monitoring techniques to create multi-dimensional insights. This include monitoring changes with radar interferometry, synthetic aperture radars (SAR), etc. Ice sheet models too have evolved in these years providing robust estimate of changes and making forecasts of changes in multiple climate scenarios. Techniques like multi-frequency radiometry has potential to separate influence of winds from

accumulation and thus provide more accurate estimates.

In a nutshell, we learned about multiple climate processes including its behavior, causes and how it can influence the changes in the AIS. These climate processes vary largely in multiple aspects including region of influence, frequency of occurrence, magnitude of influence, etc. All these processes undergo decadal changes in their behavior which makes it challenging to distinguish among multiple climate signatures. We see influence of multiple climate processes in the inter annual mass balance or height change patterns in the AIS. Better understanding of these inter annual processes and anomalies it causes in the nominal mass change patterns will help us better constrain other unknown or poorly known variables like GIA, mass balance, future sea level rise, etc.

Bibliography

Arthern, Robert J, Dale P Winebrenner, and David G Vaughan (2006). "Antarctic snow accumulation mapped using polarization of 4.3-cm wavelength microwave emission". In: *Journal of Geophysical Research: Atmospheres* 111.D6.

Arthern, Robert J, David G Vaughan, Andrew M Rankin, Robert Mulvaney, and Elizabeth R Thomas (2010). "In situ measurements of Antarctic snow compaction compared with predictions of models". In: *Journal of Geophysical Research: Earth Surface* 115.F3.

Autret, Guilhem, Frédérique Rémy, and Sylvie Roques (2013). "Multiscale analysis of Antarctic surface temperature series by empirical mode decomposition". In: *Journal of Atmospheric and Oceanic Technology* 30.4, pp. 649–654.

Bader, Henri (1962). "Theory of densification of dry snow on high polar glaciers, II". In.

Bailey, David A and Amanda H Lynch (2000). "Development of an Antarctic regional climate system model. Part I: Sea ice and large-scale circulation". In: *Journal of Climate* 13.8, pp. 1337–1350.

Bamber, Jonathan L, Simon Ekholm, and William B Krabill (2001). "A new, high-resolution digital elevation model of Greenland fully validated with airborne laser altimeter data". In: *Journal of Geophysical Research: Solid Earth* 106.B4, pp. 6733–6745.

Barletta, Valentina Roberta, Louise Sandberg Sørensen, and René Forsberg (2013). "Scatter of mass changes estimates at basin scale for Greenland and Antarctica". In: *The Cryosphere* 7.5, pp. 1411–1432.

Barnola, J-M, P Pimienta, D Raynaud, and Ye S Korotkevich (1991). "CO2-climate relationship as deduced from the Vostok ice core: A re-examination based on new measurements and on a re-evaluation of the air dating". In: *Tellus B* 43.2, pp. 83–90.

Benson, Carl S (1959). *Physical investigations on the snow and firn of northwest Greenland 1952, 1953, and 1954*. Vol. 26. US Army Snow Ice and Permafrost Research Establishment, Corps of Engineers.

— (1962). *Stratigraphic studies in the snow and firn of the Greenland ice sheet*. Tech. rep. Cold Regions Research and Engineering Lab HANOVER NH.

Bian, Lingen and Xiang Lin (2012). “Interdecadal change in the Antarctic Circumpolar Wave during 1951–2010”. In: *Advances in Atmospheric Sciences* 29.3, pp. 464–470.

Bindschadler, Robert (1998). “Monitoring ice sheet behavior from space”. In: *Reviews of Geophysics* 36.1, pp. 79–104.

Bodart, JA and RJ Bingham (2019). “The impact of the extreme 2015–2016 El Niño on the mass balance of the Antarctic ice sheet”. In: *Geophysical Research Letters* 46.23, pp. 13862–13871.

Boening, Carmen, Matthew Lebsock, Felix Landerer, and Graeme Stephens (2012). “Snowfall-driven mass change on the East Antarctic ice sheet”. In: *Geophysical Research Letters* 39.21.

Bracegirdle, Thomas J, John Turner, J Scott Hosking, and Tony Phillips (2014). “Sources of uncertainty in projections of twenty-first century westerly wind changes over the Amundsen Sea, West Antarctica, in CMIP5 climate models”. In: *Climate dynamics* 43.7-8, pp. 2093–2104.

Brenner, AC, RA Blndschadler, RH Thomas, and HJ Zwally (1983). “Slope-induced errors in radar altimetry over continental ice sheets”. In: *Journal of Geophysical Research: Oceans* 88.C3, pp. 1617–1623.

Bromwich, David H, Biao Chen, and Ren-Yow Tzeng (1995). “Arctic and Antarctic precipitation simulations produced by the NCAR community climate models”. In: *Annals of Glaciology* 21, pp. 117–122.

Bromwich, David H, Zhichang Guo, Lesheng Bai, and Qiu-shi Chen (2004). “Modeled Antarctic precipitation. Part I: Spatial and temporal variability”. In: *Journal of Climate* 17.3, pp. 427–447.

Bromwich, David H, Andrew J Monaghan, Kevin W Manning, and Jordan G Powers (2005). “Real-time forecasting for the Antarctic: An evaluation of the Antarctic Mesoscale Prediction System (AMPS)”. In: *Monthly Weather Review* 133.3, pp. 579–603.

Brooks, RL, William J Campbell, Rene O Ramseier, H Ray Stanley, and H Jay Zwally (1978). “Ice sheet topography by satellite altimetry”. In: *Nature* 274.5671, pp. 539–543.

Cai, Wenju and Peter G Baines (2001). “Forcing of the Antarctic Circumpolar Wave by El Niño-Southern Oscillation teleconnections”. In: *Journal of Geophysical Research: Oceans* 106.C5, pp. 9019–9038.

Cavalieri, DJ and CL Parkinson (2008). “Antarctic sea ice variability and trends, 1979–2006”. In: *Journal of Geophysical Research: Oceans* 113.C7.

Cazenave, A, K Dominh, S Guinehut, E Berthier, W Llovel, G Ramillien, M Ablain, and G Larnicol (2009). “Sea level budget over 2003–2008: A reevaluation from

GRACE space gravimetry, satellite altimetry and Argo". In: *Global and Planetary Change* 65.1-2, pp. 83–88.

Cerrone, D, G Fusco, Y Cotroneo, I Simmonds, and G Budillon (2017). "The antarctic circumpolar wave: Its presence and interdecadal changes during the last 142 years". In: *Journal of Climate* 30.16, pp. 6371–6389.

Christoph, Michael, Timothy P Barnett, and Erich Roeckner (1998). "The Antarctic Circumpolar Wave in a coupled ocean–atmosphere GCM". In: *Journal of Climate* 11.7, pp. 1659–1672.

Connolley, WM (2002). "Long-term variation of the Antarctic Circumpolar Wave". In: *Journal of Geophysical Research: Oceans* 107.C4, SOV–3.

Cullen, MJP (1993). "The unified forecast/climate model". In: *Meteorological Magazine* 122.1449, pp. 81–94.

Davis, Curt H., Yonghong Li, Joseph R. McConnell, Markus M. Frey, and Edward Hanna (2005). "Snowfall-Driven Growth in East Antarctic Ice Sheet Mitigates Recent Sea-Level Rise". In: *Science* 308.5730, pp. 1898–1901. DOI: 10.1126/science.1110662. eprint: https://www.science.org/doi/pdf/10.1126/science.1110662. URL: https://www.science.org/doi/abs/10.1126/science.1110662.

Deb, Pranab, Andrew Orr, David H Bromwich, Julien P Nicolas, John Turner, and J Scott Hosking (2018). "Summer drivers of atmospheric variability affecting ice shelf thinning in the Amundsen Sea Embayment, West Antarctica". In: *Geophysical Research Letters* 45.9, pp. 4124–4133.

Depoorter, M. A., J. L. Bamber, J. A. Griggs, J. T. M. Lenaerts, S. R. M. Ligtenberg, M. R. van den Broeke, and G. Moholdt (Oct. 2013). "Calving fluxes and basal melt rates of Antarctic ice shelves". In: *Nature* 502.7469, pp. 89–92. DOI: 10.1038/nature12567. URL: https://ideas.repec.org/a/nat/nature/v502y2013i7469d10.1038_nature12567.html.

Donat-Magnin, Marion, Nicolas C Jourdain, Hubert Gallée, Charles Amory, Christoph Kittel, Xavier Fettweis, Jonathan D Wille, Vincent Favier, Amine Drira, and Cécile Agosta (2020). "Interannual variability of summer surface mass balance and surface melting in the Amundsen sector, West Antarctica". In: *The Cryosphere* 14.1, pp. 229–249.

ECMWF (2009). "IFS Documentation CY33R1 - Part IV: Physical Processes". In: *IFS Documentation CY33R1*. IFS Documentation 4. ¡p¿ Operational implementation 3 June 2008¡/p¿. ECMWF. DOI: 10.21957/8o7vwlbdr. URL: https://www.ecmwf.int/node/9227.

Ettema, Janneke, Michiel R van den Broeke, Erik van Meijgaard, Willem Jan van de Berg, Jonathan L Bamber, Jason E Box, and Roger C Bales (2009). "Higher sur-

face mass balance of the Greenland ice sheet revealed by high-resolution climate modeling". In: *Geophysical Research Letters* 36.12.

Fischer, Hubertus, F Traufetter, Hans Oerter, Rolf Weller, and Heinrich Miller (2004). "Prevalence of the Antarctic Circumpolar Wave over the last two millenia recorded in Dronning Maud Land ice". In: *Geophysical research letters* 31.8.

Flament, Thomas and Frédérique Rémy (2012). "Dynamic thinning of Antarctic glaciers from along-track repeat radar altimetry". In: *Journal of Glaciology* 58.211, pp. 830–840.

Fogt, Ryan L, David H Bromwich, and Keith M Hines (2011). "Understanding the SAM influence on the South Pacific ENSO teleconnection". In: *Climate dynamics* 36.7, pp. 1555–1576.

Fogt, Ryan L, Alex J Wovrosh, Ryan A Langen, and Ian Simmonds (2012). "The characteristic variability and connection to the underlying synoptic activity of the Amundsen-Bellingshausen Seas Low". In: *Journal of Geophysical Research: Atmospheres* 117.D7.

Fretwell, Peter, Hamish D Pritchard, David G Vaughan, Jonathan L Bamber, Nicholas E Barrand, R Bell, C Bianchi, RG Bingham, Donald D Blankenship, G Casassa, et al. (2013). "Bedmap2: improved ice bed, surface and thickness datasets for Antarctica". In: *The Cryosphere* 7.1, pp. 375–393.

Forsberg, Rene, Louise Sørensen, and Sebastian Simonsen (2017). "Greenland and Antarctica ice sheet mass changes and effects on global sea level". In: *Integrative Study of the Mean Sea Level and Its Components*, pp. 91–106.

GAO, Chun-Chun, Yang LU, Zi-Zhan ZHANG, Hong-Ling SHI, and Chuan-Dong ZHU (2015). "Ice sheet mass balance in Antarctica measured by GRACE and its uncertainty". In: *Chinese journal of geophysics* 58.3, pp. 780–792.

Gao, Chunchun, Yang Lu, Zizhan Zhang, and Hongling Shi (2019). "A joint inversion estimate of antarctic ice sheet mass balance using multi-geodetic data sets". In: *Remote Sensing* 11.6, p. 653.

Gaposchkin, EM and H Frey (2000). "Geoid recovery using geophysical inverse theory applied to satellite to satellite tracking data". In.

Gardner, Alex S, Geir Moholdt, J Graham Cogley, Bert Wouters, Anthony A Arendt, John Wahr, Etienne Berthier, Regine Hock, W Tad Pfeffer, Georg Kaser, et al. (2013). "A reconciled estimate of glacier contributions to sea level rise: 2003 to 2009". In: *science* 340.6134, pp. 852–857.

Genthon, Christophe and Gerhard Krinner (2001). "Antarctic surface mass balance and systematic biases in general circulation models". In: *Journal of Geophysical Research: Atmospheres* 106.D18, pp. 20653–20664.

Groh, Andreas, Heiko Ewert, Ralf Rosenau, Elisa Fagiolini, Christian Gruber, Dana Floricioiu, W Abdel Jaber, Stefanie Linow, Frank Flechtner, Michael Eineder,

et al. (2014). “Mass, volume and velocity of the Antarctic Ice Sheet: present-day changes and error effects”. In: *Surveys in Geophysics* 35.6, pp. 1481–1505.

Grinsted, Aslak (2013). “An estimate of global glacier volume”. In: *The Cryosphere* 7.1, pp. 141–151.

Gunter, Brian, T Urban, R Riva, M Helsen, R Harpold, S Poole, P Nagel, B Schutz, and B Tapley (2009). “A comparison of coincident GRACE and ICESat data over Antarctica”. In: *Journal of Geodesy* 83.11, pp. 1051–1060.

Gunter, BC, O Didova, REM Riva, SRM Ligtenberg, JTM Lenaerts, MA King, MR Van den Broeke, and T Urban (2014). “Empirical estimation of present-day Antarctic glacial isostatic adjustment and ice mass change”. In: *The Cryosphere* 8.2, pp. 743–760.

Harig, Christopher and Frederik J Simons (2015). “Long term mass changes and interannual variability in the Canadian Archipelago and Gulf of Alaska from GRACE”. In: *AGU Fall Meeting Abstracts*. Vol. 2015, G31A–1105.

Helm, Veit, Angelika Humbert, and Heinrich Miller (2014). “Elevation and elevation change of Greenland and Antarctica derived from CryoSat-2”. In: *The Cryosphere* 8.4, pp. 1539–1559.

Helsen, Michiel M, Michiel R Van Den Broeke, Roderik SW Van De Wal, Willem Jan Van De Berg, Erik Van Meijgaard, Curt H Davis, Yonghong Li, and Ian Goodwin (2008). “Elevation changes in Antarctica mainly determined by accumulation variability”. In: *science* 320.5883, pp. 1626–1629.

Herron, Michael M and Chester C Langway (1980). “Firn densification: an empirical model”. In: *Journal of Glaciology* 25.93, pp. 373–385.

Horwath, Martin and Reinhard Dietrich (2009). “Signal and error in mass change inferences from GRACE: the case of Antarctica”. In: *Geophysical Journal International* 177.3, pp. 849–864.

Horwath, Martin, Benoıt Legrésy, Frédérique Rémy, Fabien Blarel, and Jean-Michel Lemoine (2012). “Consistent patterns of Antarctic ice sheet interannual variations from ENVISAT radar altimetry and GRACE satellite gravimetry”. In: *Geophysical Journal International* 189.2, pp. 863–876.

Hosking, J Scott, Andrew Orr, Gareth J Marshall, John Turner, and Tony Phillips (2013). “The influence of the Amundsen–Bellingshausen Seas low on the climate of West Antarctica and its representation in coupled climate model simulations”. In: *Journal of Climate* 26.17, pp. 6633–6648.

Huang, Boyin, Peter W Thorne, Viva F Banzon, Tim Boyer, Gennady Chepurin, Jay H Lawrimore, Matthew J Menne, Thomas M Smith, Russell S Vose, and Huai-Min Zhang (2017). “Extended reconstructed sea surface temperature, version 5 (ERSSTv5): upgrades, validations, and intercomparisons”. In: *Journal of Climate* 30.20, pp. 8179–8205.

Huang, Norden E, Zheng Shen, Steven R Long, Manli C Wu, Hsing H Shih, Quanan Zheng, Nai-Chyuan Yen, Chi Chao Tung, and Henry H Liu (1998). "The empirical mode decomposition and the Hilbert spectrum for nonlinear and nonstationary time series analysis". In: *Proceedings of the Royal Society of London. Series A: mathematical, physical and engineering sciences* 454.1971, pp. 903–995.

Huss, Matthias and Daniel Farinotti (2012). "Distributed ice thickness and volume of all glaciers around the globe". In: *Journal of Geophysical Research: Earth Surface* 117.F4.

Ivins, Erik R, Thomas S James, John Wahr, Ernst J O. Schrama, Felix W Landerer, and Karen M Simon (2013). "Antarctic contribution to sea level rise observed by GRACE with improved GIA correction". In: *Journal of Geophysical Research: Solid Earth* 118.6, pp. 3126–3141.

Jouzel, Jean, Valérie Masson-Delmotte, Olivier Cattani, Gabrielle Dreyfus, Sonia Falourd, Georg Hoffmann, Benedicte Minster, Julius Nouet, Jean-Marc Barnola, Jérôme Chappellaz, et al. (2007). "Orbital and millennial Antarctic climate variability over the past 800,000 years". In: *science* 317.5839, pp. 793–796.

Ju, Xiao-Lei, Yun-Zhong SHEN, and Zi-Zhan ZHANG (2013). "Antarctic ice mass change analysis based on GRACE RL05 data". In: *Chinese Journal of Geophysics* 56.9, pp. 2918–2927.

Kahn, WD, SM Klosko, and WT Wells (1982). "Mean gravity anomalies from a combination of Apollo/ATS 6 and GEOS 3/ATS 6 SST tracking campaigns". In: *Journal of Geophysical Research: Solid Earth* 87.B4, pp. 2904–2918.

Kaitheri, Athul, Anthony Mémin, and Frédérique Rémy (2021). "Inter-Annual Variability in the Antarctic Ice Sheets Using Geodetic Observations and a Climate Model". In: *Remote Sensing* 13.11, p. 2199.

Kern, Michael, Robert Cullen, Bruno Berruti, Jerome Bouffard, Tania Casal, Mark R Drinkwater, Antonio Gabriele, Arnaud Lecuyot, Michael Ludwig, Rolv Midthassel, et al. (2020). "The Copernicus Polar Ice and Snow Topography Altimeter (CRISTAL) high-priority candidate mission". In: *The Cryosphere* 14.7, pp. 2235–2251.

Kerr, Andrew (1993). "Topography, climate and ice masses: a review". In: *Terra Nova* 5.4, pp. 332–342.

Kojima, Kenji and M Mellor (1964). "Densification of snow in Antarctica". In: *Antarctic snow and ice studies. Washington, DC, American Geophysical Union*, pp. 157–218.

Kwok, Ron and Josefino C Comiso (2002). "Spatial patterns of variability in Antarctic surface temperature: Connections to the Southern Hemisphere Annular Mode and the Southern Oscillation". In: *Geophysical Research Letters* 29.14, pp. 50–1.

Kwok, Ronald, Josefino C Comiso, Tong Lee, and PR Holland (2016). "Linked trends in the South Pacific sea ice edge and Southern Oscillation Index". In: *Geophysical Research Letters* 43.19, pp. 10–295.

Lachlan-Cope, Tom A, William M Connolley, and John Turner (2001). "The role of the non-axisymmetric Antarctic orography in forcing the observed pattern of variability of the Antarctic climate". In: *Geophysical research letters* 28.21, pp. 4111–4114.

Landerer, Felix W, Frank M Flechtner, Himanshu Save, Frank H Webb, Tamara Bandikova, William I Bertiger, Srinivas V Bettadpur, Sung Hun Byun, Christoph Dahle, Henryk Dobslaw, et al. (2020). "Extending the global mass change data record: GRACE Follow-On instrument and science data performance". In: *Geophysical Research Letters* 47.12, e2020GL088306.

Legresy, Benoit, Fabrice Papa, Frederique Remy, Gaetan Vinay, Mathias Van den Bosch, and Ouan-Zan Zanife (2005). "ENVISAT radar altimeter measurements over continental surfaces and ice caps using the ICE-2 retracking algorithm". In: *Remote Sensing of Environment* 95.2, pp. 150–163.

Lemke, Peter, Jiawen Ren, Richard B Alley, Ian Allison, Jorge Carrasco, Gregory Flato, Yoshiyuki Fujii, Georg Kaser, Philip Mote, Robert H Thomas, et al. (2007). "Observations: changes in snow, ice and frozen ground". In.

Lenaerts, JTM and MR Van den Broeke (2012). "Modeling drifting snow in Antarctica with a regional climate model: 2. Results". In: *Journal of Geophysical Research: Atmospheres* 117.D5.

Lenaerts, Jan TM, Michiel R Van Den Broeke, Claudio Scarchilli, and Cécile Agosta (2012). "Impact of model resolution on simulated wind, drifting snow and surface mass balance in Terre Adélie, East Antarctica". In: *Journal of Glaciology* 58.211, pp. 821–829.

Lenaerts, Jan TM, Dewi Le Bars, Leo Van Kampenhout, Miren Vizcaino, Ellyn M Enderlin, and Michiel R Van Den Broeke (2015). "Representing Greenland ice sheet freshwater fluxes in climate models". In: *Geophysical Research Letters* 42.15, pp. 6373–6381.

Lenaerts, Jan TM, Brooke Medley, Michiel R van den Broeke, and Bert Wouters (2019). "Observing and modeling ice sheet surface mass balance". In: *Reviews of Geophysics* 57.2, pp. 376–420.

LI, Fei, Le-Xian YUAN, Sheng-Kai ZHANG, Yuan-De YANG, E Dong-Chen, Wei-Feng HAO, et al. (2016). "Mass change of the Antarctic ice sheet derived from ICESat laser altimetry". In: *Chinese Journal of Geophysics* 59.1, pp. 93–100.

Li, Jun and H Jay Zwally (2011). "Modeling of firn compaction for estimating ice-sheet mass change from observed ice-sheet elevation change". In: *Annals of Glaciology* 52.59, pp. 1–7.

Li, Jilu, John Paden, Carl Leuschen, Fernando Rodriguez-Morales, Richard D Hale, Emily J Arnold, Reid Crowe, Daniel Gomez-Garcia, and Prasad Gogineni (2012). "High-altitude radar measurements of ice thickness over the Antarctic and Greenland ice sheets as a part of operation icebridge". In: *IEEE Transactions on Geoscience and Remote Sensing* 51.2, pp. 742–754.

Li, Jun and H Jay Zwally (2015). "Response times of ice-sheet surface heights to changes in the rate of Antarctic firn compaction caused by accumulation and temperature variations". In: *Journal of Glaciology* 61.230, pp. 1037–1047.

Ligtenberg, SRM, MM Helsen, and MR Van den Broeke (2011). "An improved semi-empirical model for the densification of Antarctic firn". In: *The Cryosphere* 5.4, pp. 809–819.

Ligtenberg, SRM, P Kuipers Munneke, and MR Van den Broeke (2014). "Present and future variations in Antarctic firn air content". In: *The Cryosphere* 8.5, pp. 1711–1723.

Marshall, Gareth J (2003). "Trends in the Southern Annular Mode from observations and reanalyses". In: *Journal of climate* 16.24, pp. 4134–4143.

Masson-Delmotte, V, P Zhai, A Priani, SL Connors, C Péan, S Berger, et al. (2021). *IPCC, 2021: Climate Change 2021: The Physical Science Basis. Contribution of Working Group I to the Sixth Assessment Report of the Intergovernmental Panel on Climate Change*.

Massom, Robert and Dan Lubin (2006). *Polar remote sensing*. Vol. 2. Springer.

Massom, Robert A and Sharon E Stammerjohn (2010). "Antarctic sea ice change and variability–physical and ecological implications". In: *Polar Science* 4.2, pp. 149–186.

McConnell, JR, RJ Arthern, E Mosley-Thompson, CH Davis, RC Bales, R Thomas, JF Burkhart, and JD Kyne (2000). "Changes in Greenland ice sheet elevation attributed primarily to snow accumulation variability". In: *Nature* 406.6798, pp. 877–879.

McMillan, Malcolm, Andrew Shepherd, Aud Sundal, Kate Briggs, Alan Muir, Andrew Ridout, Anna Hogg, and Duncan Wingham (2014). "Increased ice losses from Antarctica detected by CryoSat-2". In: *Geophysical Research Letters* 41.11, pp. 3899–3905.

Mémin, Anthony, Yves Rogister, Jacques Hinderer, OC Omang, and Bernard Luck (2011). "Secular gravity variation at Svalbard (Norway) from ground observations and GRACE satellite data". In: *Geophysical Journal International* 184.3, pp. 1119–1130.

Mémin, A, T Flament, F Rémy, and M Llubes (2014). "Snow-and ice-height change in Antarctica from satellite gravimetry and altimetry data". In: *Earth and Planetary Science Letters* 404, pp. 344–353.

Mémin, A, T Flament, B Alizier, C Watson, and Florence Rémy (2015). "Interannual variation of the Antarctic Ice Sheet from a combined analysis of satellite gravimetry and altimetry data". In: *Earth and Planetary Science Letters* 422, pp. 150–156.

Mo, Kingtse C and Glenn H White (1985). "Teleconnections in the southern hemisphere". In: *Monthly Weather Review* 113.1, pp. 22–37.

Moore, Philip and Matt A King (2008). "Antarctic ice mass balance estimates from GRACE: Tidal aliasing effects". In: *Journal of Geophysical Research: Earth Surface* 113.F2.

Mu, Dapeng, Haoming Yan, Wei Feng, and Peng Peng (2017). "GRACE leakage error correction with regularization technique: case studies in Greenland and Antarctica". In: *Geophysical Journal International* 208.3, pp. 1775–1786.

Nuncio, M, Alvarinho J Luis, and X Yuan (2011). "Topographic meandering of Antarctic Circumpolar Current and Antarctic Circumpolar Wave in the ice-ocean-atmosphere system". In: *Geophysical research letters* 38.13.

Pachauri, Rajendra K, Myles R Allen, Vicente R Barros, John Broome, Wolfgang Cramer, Renate Christ, John A Church, Leon Clarke, Qin Dahe, Purnamita Dasgupta, et al. (2014). *Climate change 2014: synthesis report. Contribution of Working Groups I, II and III to the fifth assessment report of the Intergovernmental Panel on Climate Change*. Ipcc.

Paolo, FS, L Padman, HA Fricker, S Adusumilli, S Howard, and MR Siegfried (2018). "Response of Pacific-sector Antarctic ice shelves to the El Niño/Southern oscillation". In: *Nature geoscience* 11.2, pp. 121–126.

Parker, DE (1983). "Documentation of a Southern Oscillation index". In.

PATERSON, W.S.B. (1994). "2 - The Transformation of Snow to Ice". In: *The Physics of Glaciers (Third Edition)*. Ed. by W.S.B. PATERSON. Third Edition. Amsterdam: Pergamon, pp. 8–25. ISBN: 978-0-08-037944-9. DOI: https://doi.org/10.1016/B978-0-08-037944-9.50008-X. URL: https://www.sciencedirect.com/science/article/pii/B978008037944950008X.

Peltier, W Richard (2004). "Global glacial isostasy and the surface of the ice-age Earth: the ICE-5G (VM2) model and GRACE". In: *Annu. Rev. Earth Planet. Sci.* 32, pp. 111–149.

Peterson, Ray G and Warren B White (1998). "Slow oceanic teleconnections linking the Antarctic circumpolar wave with the tropical El Niño-Southern Oscillation". In: *Journal of Geophysical Research: Oceans* 103.C11, pp. 24573–24583.

Pollard, David and PMIP Participating Groups (2000). "Comparisons of ice-sheet surface mass budgets from Paleoclimate Modeling Intercomparison Project (PMIP) simulations". In: *Global and Planetary Change* 24.2, pp. 79–106.

Press, William H, Saul A Teukolsky, Brian P Flannery, and William T Vetterling (1992). *Numerical recipes in Fortran 77: volume 1, volume 1 of Fortran numerical recipes: the art of scientific computing*. Cambridge university press.

Pritchard, Hamish D, Robert J Arthern, David G Vaughan, and Laura A Edwards (2009). "Extensive dynamic thinning on the margins of the Greenland and Antarctic ice sheets". In: *Nature* 461.7266, pp. 971–975.

Pritchard, Hamish D, SB Luthcke, and Andrew H Fleming (2010). "Understanding ice-sheet mass balance: progress in satellite altimetry and gravimetry". In: *Journal of Glaciology* 56.200, pp. 1151–1161.

Pritchard, HDx, Stefan RM Ligtenberg, Helen A Fricker, David G Vaughan, Michiel R van den Broeke, and Laurence Padman (2012). "Antarctic ice-sheet loss driven by basal melting of ice shelves". In: *Nature* 484.7395, pp. 502–505.

Radić, Valentina, Andrew Bliss, A Cody Beedlow, Regine Hock, Evan Miles, and J Graham Cogley (2014). "Regional and global projections of twenty-first century glacier mass changes in response to climate scenarios from global climate models". In: *Climate Dynamics* 42.1-2, pp. 37–58.

Ramillien, G, A Lombard, A Cazenave, ER Ivins, M Llubes, F Remy, and R Biancale (2006). "Interannual variations of the mass balance of the Antarctica and Greenland ice sheets from GRACE". In: *Global and Planetary Change* 53.3, pp. 198–208.

Raphael, Marilyn N, GJ Marshall, J Turner, RL Fogt, D Schneider, DA Dixon, JS Hosking, JMa Jones, and William R Hobbs (2016). "The Amundsen Sea low: Variability, change, and impact on Antarctic climate". In: *Bulletin of the American Meteorological Society* 97.1, pp. 111–121.

Reijmer, CH, E Van Meijgaard, and MR Van den Broeke (2005). "Evaluation of temperature and wind over Antarctica in a Regional Atmospheric Climate Model using 1 year of automatic weather station data and upper air observations". In: *Journal of Geophysical Research: Atmospheres* 110.D4.

Rémy, Frédérique, Benoɪt Legresy, and Laurent Testut (2001). "Ice sheet and satellite altimetry". In: *Surveys in Geophysics* 22.1, pp. 1–29.

Rémy, Frédérique and Frédéric Parrenin (2004). "Snow accumulation variability and random walk: how to interpret changes of surface elevation in Antarctica". In: *Earth and Planetary Science Letters* 227.3-4, pp. 273–280.

Rémy, Frédérique and Massimo Frezzotti (2006). "Antarctica ice sheet mass balance". In: *Comptes Rendus Geoscience* 338.14-15, pp. 1084–1097.

Rémy, Frédérique and Soazig Parouty (2009). "Antarctic ice sheet and radar altimetry: A review". In: *Remote Sensing* 1.4, pp. 1212–1239.

Rémy, Frédérique, Thomas Flament, Aurélie Michel, and Jacques Verron (2014). "Ice sheet survey over Antarctica using satellite altimetry: ERS-2, Envisat, SARAL/AltiKa,

the key importance of continuous observations along the same repeat orbit". In: *International Journal of Remote Sensing* 35.14, pp. 5497–5512.

Ridley, JK and KC Partington (1988). "A model of satellite radar altimeter return from ice sheets". In: *Remote Sensing* 9.4, pp. 601–624.

Rignot, Eric and Robert H Thomas (2002). "Mass balance of polar ice sheets". In: *Science* 297.5586, pp. 1502–1506.

Rignot, Eric, Jonathan L Bamber, Michiel R Van Den Broeke, Curt Davis, Yonghong Li, Willem Jan Van De Berg, and Erik Van Meijgaard (2008). "Recent Antarctic ice mass loss from radar interferometry and regional climate modelling". In: *Nature geoscience* 1.2, pp. 106–110.

Rignot, Eric, Isabella Velicogna, Michael R van den Broeke, Andrew Monaghan, and Jan TM Lenaerts (2011a). "Acceleration of the contribution of the Greenland and Antarctic ice sheets to sea level rise". In: *Geophysical Research Letters* 38.5.

Rignot, Eric, Jeremie Mouginot, and B Scheuchl (2011b). "Ice flow of the Antarctic ice sheet". In: *Science* 333.6048, pp. 1427–1430.

— (2011c). "Antarctic grounding line mapping from differential satellite radar interferometry". In: *Geophysical Research Letters* 38.10.

Rignot, Eric, S Jacobs, Jeremie Mouginot, and B Scheuchl (2013). "Ice-shelf melting around Antarctica". In: *Science* 341.6143, pp. 266–270.

Rignot, Eric, Jérémie Mouginot, Bernd Scheuchl, Michiel Van Den Broeke, Melchior J Van Wessem, and Mathieu Morlighem (2019). "Four decades of Antarctic Ice Sheet mass balance from 1979–2017". In: *Proceedings of the National Academy of Sciences* 116.4, pp. 1095–1103.

Rodell, Matthew, PR Houser, UEA Jambor, J Gottschalck, K Mitchell, C-J Meng, K Arsenault, B Cosgrove, J Radakovich, M Bosilovich, et al. (2004). "The global land data assimilation system". In: *Bulletin of the American Meteorological Society* 85.3, pp. 381–394.

Ropelewski, Chester F and Phil D Jones (1987). "An extension of the Tahiti–Darwin southern oscillation index". In: *Monthly weather review* 115.9, pp. 2161–2165.

Rowlands, David D, Richard D Ray, Douglas S Chinn, and Frank G Lemoine (2002). "Short-arc analysis of intersatellite tracking data in a gravity mapping mission". In: *Journal of Geodesy* 76.6-7, pp. 307–316.

Rummel, Reiner (1980). *Geoid Heights, Geoid Height Differences, and Mean Gravity Anomalies from'Low-Low'Satellite-to-Satellite Tracking-An Error Analysis.* Tech. rep. OHIO STATE UNIV COLUMBUS DEPT OF GEODETIC SCIENCE.

Sakumura, C, S Bettadpur, and S Bruinsma (2014). "Ensemble prediction and intercomparison analysis of GRACE time-variable gravity field models". In: *Geophysical Research Letters* 41.5, pp. 1389–1397.

Sasgen, Ingo, Henryk Dobslaw, Z Martinec, and Maik Thomas (2010). “Satellite gravimetry observation of Antarctic snow accumulation related to ENSO”. In: *Earth and Planetary Science Letters* 299.3-4, pp. 352–358.

Sasgen, Ingo, Hannes Konrad, ER Ivins, MR Van den Broeke, JL Bamber, Z Martinec, and Volker Klemann (2013). “Antarctic ice-mass balance 2003 to 2012: regional reanalysis of GRACE satellite gravimetry measurements with improved estimate of glacial-isostatic adjustment based on GPS uplift rates”. In: *The Cryosphere* 7.5, pp. 1499–1512.

Scambos, Theodore A, Massimo Frezzotti, T Haran, J Bohlander, JTM Lenaerts, MR Van Den Broeke, K Jezek, D Long, S Urbini, K Farness, et al. (2012). “Extent of low-accumulation’wind glaze’areas on the East Antarctic plateau: implications for continental ice mass balance”. In: *Journal of glaciology* 58.210, pp. 633–647.

Schneider, David P, Yuko Okumura, and Clara Deser (2012). “Observed Antarctic interannual climate variability and tropical linkages”. In: *Journal of climate* 25.12, pp. 4048–4066.

Schrama, Ernst JO, Bert Wouters, and Roelof Rietbroek (2014). “A mascon approach to assess ice sheet and glacier mass balances and their uncertainties from GRACE data”. In: *Journal of Geophysical Research: Solid Earth* 119.7, pp. 6048–6066.

Schröder, Ludwig, Martin Horwath, Reinhard Dietrich, Veit Helm, Michiel R Broeke, and Stefan RM Ligtenberg (2019). “Four decades of Antarctic surface elevation changes from multi-mission satellite altimetry”. In: *The Cryosphere* 13.2, pp. 427–449.

Shepherd, Andrew, Erik R Ivins, A Geruo, Valentina R Barletta, Mike J Bentley, Srinivas Bettadpur, Kate H Briggs, David H Bromwich, René Forsberg, Natalia Galin, et al. (2012). “A reconciled estimate of ice-sheet mass balance”. In: *Science* 338.6111, pp. 1183–1189.

Shepherd, Andrew, Erik Ivins, Eric Rignot, Ben Smith, Michiel Van Den Broeke, Isabella Velicogna, Pippa Whitehouse, Kate Briggs, Ian Joughin, Gerhard Krinner, et al. (2018). “Mass balance of the Antarctic Ice Sheet from 1992 to 2017”. In: *Nature* 558, pp. 219–222.

Shi, Hong-Ling, Yang Lu, Zong-Liang Du, Lu-Lu Jia, Zi-Zhan Zhang, and Chun-Xia Zhou (2011). “Mass change detection in Antarctic ice sheet using ICESat block analysis techniques from 2003˜ 2008”. In: *Chinese Journal of Geophysics* 54.4, pp. 958–965.

Spada, Giorgio, Valentina Roberta Barletta, Volker Klemann, REM Riva, Zdenek Martinec, Paolo Gasperini, Björn Lund, Detlef Wolf, LLA Vermeersen, and MA King (2011). “A benchmark study for glacial isostatic adjustment codes”. In: *Geophysical Journal International* 185.1, pp. 106–132.

Stevens, C Max, Vincent Verjans, Jessica Lundin, Emma C Kahle, Annika N Horlings, Brita I Horlings, and Edwin D Waddington (2020). "The Community Firn Model (CFM) v1. 0". In: *Geoscientific Model Development* 13.9, pp. 4355–4377.

Stocker, Thomas (2014). *Climate change 2013: the physical science basis: Working Group I contribution to the Fifth assessment report of the Intergovernmental Panel on Climate Change*. Cambridge university press.

Swenson, Sean, Don Chambers, and John Wahr (2008). "Estimating geocenter variations from a combination of GRACE and ocean model output". In: *Journal of Geophysical Research: Solid Earth* 113.B8.

Tapley, Byron D, S Bettadpur, Mo Watkins, and Ch Reigber (2004a). "The gravity recovery and climate experiment: Mission overview and early results". In: *Geophysical research letters* 31.9.

Tapley, Byron D, Srinivas Bettadpur, John C Ries, Paul F Thompson, and Michael M Watkins (2004b). "GRACE measurements of mass variability in the Earth system". In: *Science* 305.5683, pp. 503–505.

Tapley, Byron D, Michael M Watkins, Frank Flechtner, Christoph Reigber, Srinivas Bettadpur, Matthew Rodell, Ingo Sasgen, James S Famiglietti, Felix W Landerer, Don P Chambers, et al. (2019). "Contributions of GRACE to understanding climate change". In: *Nature climate change* 9.5, pp. 358–369.

Talpe, Matthieu J, R Steven Nerem, Ehsan Forootan, Michael Schmidt, Frank G Lemoine, Ellyn M Enderlin, and Felix W Landerer (2017). "Ice mass change in Greenland and Antarctica between 1993 and 2013 from satellite gravity measurements". In: *Journal of Geodesy* 91.11, pp. 1283–1298.

Turner, John (2004). "The el nino–southern oscillation and antarctica". In: *International Journal of Climatology: A Journal of the Royal Meteorological Society* 24.1, pp. 1–31.

Turner, John, Tom Lachlan-Cope, Steve Colwell, and Gareth J Marshall (2005). "A positive trend in western Antarctic Peninsula precipitation over the last 50 years reflecting regional and Antarctic-wide atmospheric circulation changes". In: *Annals of Glaciology* 41, pp. 85–91.

Turner, John, Tony Phillips, J Scott Hosking, Gareth J Marshall, and Andrew Orr (2013). "The amundsen sea low". In: *International Journal of Climatology* 33.7, pp. 1818–1829.

Undén, Per, Laura Rontu, Heikki Jarvinen, Peter Lynch, Francisco Javier Calvo Sánchez, Gerard Cats, Joan Cuxart, Kalle Eerola, Carl Fortelius, José Antonio Garcıa-Moya, et al. (2002). "HIRLAM-5 scientific documentation". In.

Van Angelen, JH, JT M. Lenaerts, MR Van den Broeke, Xavier Fettweis, and E Van Meijgaard (2013). "Rapid loss of firn pore space accelerates 21st century Greenland mass loss". In: *Geophysical Research Letters* 40.10, pp. 2109–2113.

Van de Berg, WJ, MR Van den Broeke, CH Reijmer, and E Van Meijgaard (2005). "Characteristics of the Antarctic surface mass balance, 1958–2002, using a regional atmospheric climate model". In: *Annals of Glaciology* 41, pp. 97–104.

— (2006). "Reassessment of the Antarctic surface mass balance using calibrated output of a regional atmospheric climate model". In: *Journal of Geophysical Research: Atmospheres* 111.D11.

Broeke, Michiel R van den (1997). "Spatial and temporal variation of sublimation on Antarctica: Results of a high-resolution general circulation model". In: *Journal of Geophysical Research: Atmospheres* 102.D25, pp. 29765–29777.

Broeke, Michiel van den, Willem Jan Van de Berg, and Erik Van Meijgaard (2008). "Firn depth correction along the Antarctic grounding line". In: *Antarctic Science* 20.5, pp. 513–517.

Van den Broeke, Michiel R, Jonathan Bamber, Jan Lenaerts, and Eric Rignot (2011). "Ice sheets and sea level: Thinking outside the box". In: *Surveys in geophysics* 32.4-5, pp. 495–505.

Lipzig, Nicole PM van, Erik van Meijgaard, and Johannes Oerlemans (2002). "The spatial and temporal variability of the surface mass balance in Antarctica: results from a regional atmospheric climate model". In: *International Journal of Climatology: A Journal of the Royal Meteorological Society* 22.10, pp. 1197–1217.

Van Meijgaard, E, LH van Ulft, WJ van de Berg, FC Bosveld, BJJM van den Hurk, G Lenderink, and AP Siebesma (2008). "The KNMI regional atmospheric climate model, version 2.1". In: *KNMI Tech. Rep.* Vol. 302. R. Neth. Meteorol. Inst De Bilt, Netherlands.

Vaughan, David G, Jonathan L Bamber, Mario Giovinetto, Jonathan Russell, and A Paul R Cooper (1999). "Reassessment of net surface mass balance in Antarctica". In: *Journal of climate* 12.4, pp. 933–946.

Velicogna, Isabella and John Wahr (2006a). "Measurements of time-variable gravity show mass loss in Antarctica". In: *science* 311.5768, pp. 1754–1756.

— (2006b). "Acceleration of Greenland ice mass loss in spring 2004". In: *Nature* 443.7109, pp. 329–331.

Velicogna, Isabella (2009). "Increasing rates of ice mass loss from the Greenland and Antarctic ice sheets revealed by GRACE". In: *Geophysical Research Letters* 36.19.

Velicogna, I and J Wahr (2013). "Time-variable gravity observations of ice sheet mass balance: Precision and limitations of the GRACE satellite data". In: *Geophysical Research Letters* 40.12, pp. 3055–3063.

Verjans, Vincent, Amber A Leeson, Christopher Nemeth, C Max Stevens, Peter Kuipers Munneke, Brice Noël, and Jan Melchior van Wessem (2020). "Bayesian calibration of firn densification models". In: *The Cryosphere* 14.9, pp. 3017–3032.

Wahr, John, Mery Molenaar, and Frank Bryan (1998). “Time variability of the Earth’s gravity field: Hydrological and oceanic effects and their possible detection using GRACE”. In: *Journal of Geophysical Research: Solid Earth* 103.B12, pp. 30205–30229.

Walsh, Kevin JE, Ian Simmonds, and Mark Collier (2000). “Sigma-coordinate calculation of topographically forced baroclinicity around Antarctica”. In: *Dynamics of atmospheres and oceans* 33.1, pp. 1–29.

Watkins, Michael M, David N Wiese, Dah-Ning Yuan, Carmen Boening, and Felix W Landerer (2015). “Improved methods for observing Earth’s time variable mass distribution with GRACE using spherical cap mascons”. In: *Journal of Geophysical Research: Solid Earth* 120.4, pp. 2648–2671.

Wei, William WS (2018). *Multivariate time series analysis and applications*. John Wiley & Sons.

Wendler, Gerd, Charles Stearns, George Weidner, Guillaume Dargaud, and Thomas Parish (1997). “On the extraordinary katabatic winds of Adélie Land”. In: *Journal of Geophysical Research: Atmospheres* 102.D4, pp. 4463–4474.

Williams, Simon DP, Philip Moore, Matt A King, and Pippa L Whitehouse (2014). “Revisiting GRACE Antarctic ice mass trends and accelerations considering autocorrelation”. In: *Earth and Planetary Science Letters* 385, pp. 12–21.

White, Warren B and Ray G Peterson (1996). “An Antarctic circumpolar wave in surface pressure, wind, temperature and sea-ice extent”. In: *Nature* 380.6576, pp. 699–702.

White, Warren B and Neil J Cherry (1999). “Influence of the Antarctic circumpolar wave upon New Zealand temperature and precipitation during autumn–winter”. In: *Journal of Climate* 12.4, pp. 960–976.

White, Warren B (2000). “Influence of the Antarctic Circumpolar Wave on Australian precipitation from 1958 to 1997”. In: *Journal of Climate* 13.13, pp. 2125–2141.

White, Warren B and Jeffrey Annis (2004). “Influence of the Antarctic Circumpolar Wave on El Niño and its multidecadal changes from 1950 to 2001”. In: *Journal of Geophysical Research: Oceans* 109.C6.

White, Warren B and Ian Simmonds (2006). “Sea surface temperature–induced cyclogenesis in the Antarctic circumpolar wave”. In: *Journal of Geophysical Research: Oceans* 111.C8.

Whitehouse, Pippa L, Michael J Bentley, and Anne M Le Brocq (2012). “A deglacial model for Antarctica: geological constraints and glaciological modelling as a basis for a new model of Antarctic glacial isostatic adjustment”. In: *Quaternary Science Reviews* 32, pp. 1–24.

Wilkinson, DS (1988). “A pressure-sintering model for the densification of polar firn and glacier ice”. In: *Journal of Glaciology* 34.116, pp. 40–45.

Wingham, Duncan J, Andrew J Ridout, Remko Scharroo, Robert J Arthern, and CK Shum (1998). “Antarctic elevation change from 1992 to 1996”. In: *Science* 282.5388, pp. 456–458.

Wingham, DJ, A Shepherd, A Muir, and GJ Marshall (2006). “Mass balance of the Antarctic ice sheet”. In: *Philosophical Transactions of the Royal Society A: Mathematical, Physical and Engineering Sciences* 364.1844, pp. 1627–1635.

Wingham, DJ, DW Wallis, and A Shepherd (2009). “Spatial and temporal evolution of Pine Island Glacier thinning, 1995–2006”. In: *Geophysical Research Letters* 36.17.

Zhang, Bao, Yibin Yao, Lin Liu, and Yuanjian Yang (2021). “Interannual ice mass variations over the Antarctic ice sheet from 2003 to 2017 were linked to El Niño-Southern Oscillation”. In: *Earth and Planetary Science Letters* 560, p. 116796.

Zwally, H Jay, RA Bindschadler, AC Brenner, TV Martin, and RH Thomas (1983). “Surface elevation contours of Greenland and Antarctic ice sheets”. In: *Journal of Geophysical Research: Oceans* 88.C3, pp. 1589–1596.

Zwally, H Jay and Li Jun (2002). “Seasonal and interannual variations of firn densification and ice-sheet surface elevation at the Greenland summit”. In: *Journal of Glaciology* 48.161, pp. 199–207.

Zwally, H Jay, Mario B Giovinetto, Jun Li, Helen G Cornejo, Matthew A Beckley, Anita C Brenner, Jack L Saba, and Donghui Yi (2005). “Mass changes of the Greenland and Antarctic ice sheets and shelves and contributions to sea-level rise: 1992–2002”. In: *Journal of Glaciology* 51.175, pp. 509–527.

Zwally, H Jay and Mario B Giovinetto (2011). “Overview and assessment of Antarctic ice-sheet mass balance estimates: 1992–2009”. In: *Surveys in Geophysics* 32.4-5, pp. 351–376.

Zwally, H Jay, Jun Li, John W Robbins, Jack L Saba, Donghui Yi, and Anita C Brenner (2015). “Mass gains of the Antarctic ice sheet exceed losses”. In: *Journal of Glaciology* 61.230, pp. 1019–1036.

Appendix A: Scientific Communications

You will find a comprehensive list of the scientific communications done with my supervisors.

Peer-reviewed journal articles

- Kaitheri, A., Mémin, A. and Rémy, F. (2021) Inter-annual Variability in the Antarctic Ice Sheets Using Geodetic Observations and a Climate Model. Remote Sensing, 13(11), p.2199. DOI:10.3390/rs13112199.

Other international oral communications

- Kaitheri, A., Mémin, A. and Remy, F., 2021, December. Investigating inter-annual variability in the Antarctic ice sheets using multi-technique geodesy and modeling. In AGU Fall Meeting 2021. AGU.

- Kaitheri, A., Mémin, A. and Remy, F., 2021, June. Inter-annual variability in the Antarctic ice sheets using multi-technique geodesy and modelling. In Scientific Assembly of the International Association of Geodesy 2021.

- Kaitheri, A., Mémin, A. and Rémy, F., 2021, April. Global climate anomalies and their association with the mass balance of the Antarctic Ice Sheet. In EGU General Assembly Conference Abstracts (pp. EGU21-12320).

- Kaitheri, A., Mémin, A. and Remy, F., 2020, December. Global Climate Anomalies and its Influence on the Mass Balance of the Antarctic Ice Sheet.

In AGU Fall Meeting Abstracts (Vol. 2020, pp. C054-0005).

- Kaitheri, A., Mémin, A. and Rémy, F., 2020, May. Climate parameters influencing satellite-based volume and elevation changes of the Antarctic ice sheet. In EGU General Assembly Conference Abstracts (p. 18542).